

QATAR UNIVERSITY

COLLEGE OF ENGINEERING

COLLAPSE BEHAVIOR AND ENERGY ABSORPTION OF CORRUGATED

TAPERED TUBES

BY

SAMI EMAD ALKHATIB

A Thesis Submitted to
the Faculty of the College of
Engineering
in Partial Fulfillment
of the Requirements
for the Degree of
Masters of Science in Mechanical Engineering

January 2018

© 2018. Sami Alkhatib. All Rights Reserved.

COMMITTEE PAGE

The members of the Committee approve the Thesis of Sami E. Alkhatib
defended on 10/12/2017.

Prof. Faris Tarlochan
Thesis Supervisor

Prof. Elsadig Mahdi Saad
Committee Member

Prof. Ramesh Singh
Committee Member

Approved:

Khalifa Al-Khalifa, Dean, College of Engineering

ABSTRACT

Alkhatib, Sami E., Masters: January : 2018, Masters of Science in Mechanical Engineering

Title: Collapse Behavior and Energy Absorption of Corrugated Tapered Tubes

Supervisor of Thesis: Faris Tarlochan.

Thin-walled structures have been widely used in energy absorption and safety applications such as automotive vehicles and locomotives, due to their lightweight, progressive folding modes, and reduced manufacturing costs. This thesis studies the collapse behavior and energy absorption performance of corrugated tapered tubes (CTTs) as potential efficient thin-walled structures under axial and oblique loading conditions. The study was conducted using experimentally validated numerical finite element model. The proposed CTT design is impacted under seven different loading angles with a striker mass of 275 kg and 15 m/s velocity. The material assigned to the proposed design structure is AA6060 aluminum alloy. The effect of loading angles and geometric parameters on various performance indicators, such as the initial peak force (IPF), mean crushing force (MF), energy absorption (EA) and specific energy absorption (SEA) were studied. The results showed that the amplitude of corrugation is the most influential factor on the force-displacement characteristics of CTTs. Also, IPF was found to be reduced when corrugation is adopted (a maximum reduction of 93.38%), especially for longer corrugation's amplitudes and wavelengths, while EA and SEA were found to be reduced slightly. Furthermore, it was found that increasing the impact angles from 0° to 40° leads to a reduction of 54% in EA and SEA. In addition, global Euler buckling was found to develop at higher impact angles for CTTs of 80° tapered angles. Finally, it was found that CTTs of

85° tapered angle and 1-mm thickness can achieve higher SEA relative to their tapered conventional counterparts under all loading conditions (40% and 9.5% increase under axial and 40° impacts, respectively).

DEDICATION

I dedicate this thesis to my beloved family and friends,

*To my mother, Rehab, who supported me during my academic journey and taught me to believe
in myself and always pursue my dreams.*

*To my father, Emad, who worked very hard to support my education and never hesitated to give
me whatever I needed to succeed.*

*To my brothers, Mahmoud, Hossam, and Mohannad, who believed in me and motivated me to
stay on the right track to complete my master's degree.*

*I am also very grateful to my supervisor, Dr. Faris Tarlochan, who guided me and provided me
with the academic and moral support needed to complete this work.*

ACKNOWLEDGMENTS

This project was carried out in the Mechanical and Industrial Engineering Department of Qatar University. The author is grateful to the university and all faculty member who supported the project by their great ideas.

TABLE OF CONTENTS

DEDICATION	v
ACKNOWLEDGMENTS	vi
LIST OF TABLES	xi
LIST OF FIGURES	xii
PUBLICATIONS.....	xix
CHAPTER 1: INTRODUCTION.....	1
1.1 Introduction	1
1.2 Thin-walled Structures as Energy Absorbers.....	3
1.3 Objectives and Methodology	6
1.3.1 Objectives	6
1.3.2 Methodology.....	6
1.4 Contributions.....	7
1.5 Thesis Layout.....	8
CHAPTER 2: LITERATURE REVIEW	10
2.1 Introduction	10
2.2 Structural Crashworthiness	10
2.3 Structural Impact.....	12
2.3.1 Quasi-static and Dynamic Loading.....	12

2.3.2	Strain Rate Sensitivity.....	13
2.3.3	Effects of Inertia	15
2.4	Energy Absorption by Structural Collapse.....	18
2.4.1	Energy Absorber: General Principles	18
2.4.2	Performance Indicators	22
2.5	Thin-Walled Structures as Energy Absorbers.....	24
2.5.1	Circular Tubes.....	24
2.5.2	Square Tubes.....	26
2.5.3	Tubes of Different Cross-Sections.....	28
2.5.4	Multicellular Tubes.....	30
2.5.5	Tubes of Functionally Graded Thickness (FGT)	32
2.5.6	Foam-Filled Tubes	34
2.5.7	Tapered & Conical Tubes	36
2.5.8	Tubes of Patterned Surfaces.....	38
2.6	Analysis of Thin-Walled Energy Absorbers	41
2.6.1	Finite Element Modelling of Thin-Walled Structures	41
2.6.2	Use of FEM in the Literature	42
2.7	Summary of Literature Review	45
2.7.1	Main Findings from the Surveyed Literature.....	45

2.7.2	Research Gaps and Thesis Aims.....	46
CHAPTER 3: METHODOLOGY		47
3.1	Introduction	47
3.2	Development of The FE Model for Corrugated Tapered Tubes	47
3.2.1	FEM tool.....	47
3.2.2	Geometry & Design of Experiment	49
3.2.3	Element Type Selection	51
3.2.4	Mesh Size Optimization.....	57
3.2.5	Boundary Conditions	59
3.2.6	Material Properties.....	60
3.2.7	Material Model.....	62
3.3	FE Model Validation Against Experimental Testing.....	63
3.4	Summary	68
CHAPTER 4: CORRUGATED TAPERED TUBES UNDER AXIAL LOADING.....		69
4.1	Introduction	69
4.2	Force-Displacement Characteristics.....	69
4.3	Deformation Modes Under Axial Impact.....	72
4.4	Analysis of Performance Indicators under Axial Impact.....	77
4.4.1	Influence on Initial Peak Force (IPF).....	77

4.4.2	Influence on Mean Force (MF).....	82
4.4.3	Influence on Energy Absorption (EA).....	85
4.4.4	Influence on Specific Energy Absorption (SEA).....	88
4.5	Summary	91
CHAPTER 5: CORRUGATED TAPERED TUBES UNDER OBLIQUE LOADING...		93
5.1	Introduction	93
5.2	Force-Displacement Characteristics.....	93
5.3	Deformation Modes.....	95
5.4	Performance Analysis	100
5.4.1	Influence of Loading Angle	100
5.4.2	Influence of Geometric Parameters	104
5.5	Comparative Analysis	116
5.6	Summary	122
CHAPTER 6: CONCLUSIONS		123
CHAPTER 7: RECOMMENDATIONS FOR FUTURE WORK		126
REFERENCES		127
APPENDIX: PERFROMANCE INDICATORS SUMMARY		141

LIST OF TABLES

Table 2-1: Developed deformation modes in circular tubes according to their D/t and L/t ratios.....	25
Table 2-2: Developed deformation modes in square tubes according to their b/t ratios ..	28
Table 3-1: Corrugated tapered tube geometric factors and values for axial and oblique impact conditions	51
Table 3-2: Linear and quadratic elements of full and reduced integration	54
Table 3-3: Material properties of the aluminum alloy AA6060	61
Table 3-4: Johnson-Cook parameter for (AA6060) aluminum alloy.....	63
Table 3-5: Difference in IPF and EA between the original and present study models.....	67
Table 4-1: Deformation modes distribution for the 64 runs based on the amplitude and the wavelength	77

LIST OF FIGURES

Figure 1-1: Thin-walled structures as energy absorbers in vehicles.....	2
Figure 1-2: Thin-walled structures as energy absorbers in air-craft subfloors	3
Figure 2-1: Front chassis crash-boxes as energy absorbers	12
Figure 2-2: Progressive buckling of circular tubes under (a) dynamic loading; (b) quasi-static loading	13
Figure 2-3: Two common types of thin-walled energy absorbers	17
Figure 2-4: Steel circular tubes under the following velocity from right to left: 385 m/s, 277 m/s, 227 m/s, 173 m/s and 0 m/s.....	18
Figure 2-5: A vehicle impacting a large elastic spring that does not convert the kinetic energy.....	19
Figure 2-6: Typical force-displacement diagram.....	22
Figure 2-7: Circular tubes deformation modes: (a) axisymmetric mode; (b) non-axisymmetric or diamond model; (c) mixed mode	25
Figure 2-8: Deformation modes in square tubes: (a) asymmetric mixed mode, (b) inextensional mode, (c) extensional mode, and (d) non-compact mode.....	27
Figure 2-9: inward multi-corner tubes: (a) star-shaped cross-section tube; (b) criss-cross cross-section tube.....	30
Figure 2-10: multicell tubes: corners and angle elements	31
Figure 2-11: Multicellular configurations on thin-walled structures: (a) 4-cells: s4; (b) 5-cells: s5.....	32
Figure 2-12: Thickness gradient direction in FGT tubes: (a) longitudinal in conical tubes	

[79]; (b) transverse in square tubes	33
Figure 2-13: Modes of deformation of foam filled circular tubes of different foam densities [56]	35
Figure 2-14: Global Euler buckling in thin-walled structures: (a) Force-displacement profile for tubes undergoing global Euler buckling; (b) Global Euler buckling in a circular tube.....	37
Figure 2-15: Tapered tubes of different cross sections: (a) hexagonal; (b) circular; (c) square	38
Figure 2-16: Tubular structures of patterned surfaces: (a) windowed tube; (b) corrugated tube [23]	40
Figure 2-17: FE models of different thin-walled energy absorbers: (a) square tube; (b) multi-cell square tube; (c) circular tube; (d) tapered circular tube: experimental results (left), and numerical simulations (right)	44
Figure 2-18: Experimental and numerical force-displacement curves of a square tube...	44
Figure 3-1: Corrugated tapered tube profile and parameters	50
Figure 3-2: Elements families in ABAQUS	52
Figure 3-3: Deformation of material under pure bending.....	54
Figure 3-4: Deformation of linear fully integrated element under pure bending (Shear locking)	55
Figure 3-5: Defromation of linear element of reduced integration under pure bending (Hour-glassing)	56
Figure 3-6: S4R linear 4-node shell element with reduced integration	56

Figure 3-7: Mesh sensitivity analysis under axial impact.....	58
Figure 3-8: Mesh sensitivity analysis under oblique impact (40°)	58
Figure 3-9: Crash simulation setup and boundary conditions	60
Figure 3-10: ASTM E8/8M-11 sheet-type static tensile test specimen's dimensions.....	61
Figure 3-11: Axial tensile test set-up and specimen: (a) Instron Testing Machine of 250 kN capacity; (b) tensile test specimen and representative engineering stress-strain curve	62
Figure 3-12: Deformation modes of a circular aluminum tube (experimental and FE) ...	65
Figure 3-13: Deformation modes for the corrugated aluminum tube (experimental and FE)	66
Figure 3-14: Force-displacement profiles for a circular aluminum tube (experimental and FE tests)	66
Figure 3-15: Force-displacement profiles for a corrugated aluminum tube (experimental and FE tests).....	67
Figure 4-1: Force-displacement diagram of CTTs of $t = 2 \text{ mm}$ & $L = 150 \text{ mm}$ (a) Tapered Angle = 80° & $D = 40 \text{ mm}$; (b) Tapered Angle = 80° & $D = 50 \text{ mm}$; (c) Tapered Angle = 85° & $D = 40 \text{ mm}$; (d) Tapered Angle = 85° & $D = 50 \text{ mm}$	70
Figure 4-2: Force-displacement diagram of CTTs of Tapered Angle= 80° & $D = 50 \text{ mm}$ (a) $t = 1 \text{ mm}$ & $L = 150 \text{ mm}$; (b) $t = 1 \text{ mm}$ & $L = 200 \text{ mm}$; (c) $t = 2 \text{ mm}$ & $L = 150 \text{ mm}$; (d) $t = 2 \text{ mm}$ & $L = 200 \text{ mm}$	72
Figure 4-3: CTT exhibited deformation modes, a: mode 1 (Symmetric mode), b: mode 2 (Symmetric mode), c: mode 3 (Non-symmetric mode)	74
Figure 4-4: Cross-section view of the crushing stages of mode 1 of CTT of $A = 2 \text{ mm}$ and	

W = 10 mm (L = 200 mm, D = 50 mm, t = 2 mm and Tapered angle = 80°).....	74
Figure 4-5: Cross-section view of the crushing stages of mode 2 of CTT of A = 1 mm and	
W = 10 mm (L = 200 mm, D = 50 mm, t = 2 mm and Tapered angle = 80°).....	75
Figure 4-6: Cross-section view of the crushing stages of mode 3 of CTT of A = 1 mm and	
W = 20 mm (L = 200 mm, D = 50 mm, t = 2 mm and Tapered angle = 80°).....	75
Figure 4-7: The profiles of CTTs for different wavelengths (W) or amplitudes (A) at W =	
∞ and A = 0, (a) A = 1 mm (b) W = 10 mm.....	76
Figure 4-8: IPF values for CTT profiles relative to a conventional tapered tube (L = 200	
mm, D = 50 mm, t = 2 mm and Tapered angle = 80°).....	78
Figure 4-9: Influence of design parameters on IPF	80
Figure 4-10: The effect of Amplitude-Thickness interaction on IPF	81
Figure 4-11: MF values for CTT profiles relative to a conventional tapered tube (L = 200	
mm, D = 50 mm, t = 2 mm and Tapered angle = 80°).....	82
Figure 4-12: Influence of design parameters on MF	84
Figure 4-13: The effect of Amplitude-Thickness interaction on MF	84
Figure 4-14: EA values for CTT profiles relative to a conventional tapered tube (L = 200	
mm, D = 50 mm, t = 2 mm and Tapered angle = 80°).....	86
Figure 4-15: Influence of design parameters on EA.....	86
Figure 4-16: The effect of Amplitude-Thickness interaction on EA.....	87
Figure 4-17: SEA values for CTT profiles relative to a conventional tapered tube (L = 200	
mm, D = 50 mm, t = 2 mm and Tapered angle = 80°).....	89
Figure 4-18: Influence of design parameters on SEA.....	90

Figure 4-19: The effect of Amplitude-Thickness interaction on SEA.....	91
Figure 4-20: Amplitude-thickness performance influence paradox under the tested geometric factors' range: (Thickness: 1-2 mm, Amplitude= 1-2 mm)	92
Figure 5-1: Force-Displacement Diagram for CTT (A = 1 mm, W =20 mm, Tapered Angle = 85° and Thickness = 2 mm).....	94
Figure 5-2: Force-Displacement Diagram for a Regular Circular Tapered Tube (Tapered Angle = 85° and Thickness = 2 mm)	95
Figure 5-3: Final Deformation Modes for CTT (A=1 mm, W=10 mm).....	97
Figure 5-4: Final Deformation Modes for CTT (A=1 mm, W=20 mm).....	98
Figure 5-5: Final Deformation Modes for CTT (A=2 mm, W=10 mm).....	99
Figure 5-6: Final Deformation Modes for CTT (A=2 mm, W=20 mm).....	100
Figure 5-7: Effect of Load Angle on the Initial Peak Force IPF	101
Figure 5-8: Effect of Load Angle on the Mean Force (MF).....	102
Figure 5-9: Effect of Load Angle on the Energy Absorption (EA)	103
Figure 5-10: Effect of Load Angle on the Specific Energy Absorption (SEA).....	103
Figure 5-11: The Average Effect of Amplitude on IPF Under Different Loading Angles	104
Figure 5-12: The Average Effect of Wavelength on IPF Under Different Loading Angles	105
Figure 5-13: The Average Effect of Thickness on IPF Under Different Loading Angles	106
Figure 5-14: The Average Effect of Tapered Angle on IPF Under Different Loading Angles	

.....	106
Figure 5-15: The Average Effect of Amplitude on MF Under Different Loading Angles 107
Figure 5-16: The Average Effect of Wavelength on MF Under Different Loading Angles 108
Figure 5- 17: The Average Effect of Thickness on MF Under Different Loading Angles 109
Figure 5-18: The Average Effect of Tapered Angle on MF Under Different Loading Angles 109
Figure 5-19: The Average Effect of Amplitude on EA Under Different Loading Angles 110
Figure 5-20: The Average Effect of Wavelength on EA Under Different Loading Angles 111
Figure 5-21: The Average Effect of Thickness on EA Under Different Loading Angles 112
Figure 5-22: The Average Effect of Tapered Angle on EA Under Different Loading Angles 112
Figure 5-23: The Average Effect of Amplitude on SEA Under Different Loading Angles 114
Figure 5-24: The Average Effect of Wavelength on SEA Under Different Loading Angles 114
Figure 5-25: The Average Effect of Thickness on SEA Under Different Loading Angles	

.....	115
Figure 5-26: The Average Effect of Tapered Angle on SEA Under Different Loading Angles	115
Figure 5-27: SEA Values for a Conventional Tapered Tube and CTT (Tapered Angle = 80°, Thickness = 1 mm).....	117
Figure 5-28: MF Values for a Conventional Tapered Tube and CTT (Tapered Angle = 80°, Thickness = 1 mm)	117
Figure 5-29: SEA Values for a Conventional Tapered Tube and CTT (Tapered Angle = 80°, Thickness = 2 mm).....	118
Figure 5-30: MF Values for a Conventional Tapered Tube and CTT (Tapered Angle = 80°, Thickness = 2 mm)	118
Figure 5-31: SEA Values for a Conventional Tapered Tube and CTT (Tapered Angle = 85°, Thickness = 1 mm).....	120
Figure 5-32: MF Values for a Conventional Tapered Tube and CTT (Tapered Angle = 85°, Thickness = 1 mm)	120
Figure 5-33: SEA Values for a Conventional Tapered Tube and CTT (Tapered Angle = 85°, Thickness = 2 mm).....	121
Figure 5-34: MF Values for a Conventional Tapered Tube and CTT (Tapered Angle = 85°, Thickness = 2 mm)	121

PUBLICATIONS

Refereed International Journal Papers:

S. E. Alkhatib, F. Tarlochan, and A. Eyvazian, "Collapse behavior of thin-walled corrugated tapered tubes," *Engineering Structures*, vol. 150, pp. 674-692, 11/1/ 2017. (Impact Factor: 2.258)

S. E. Alkhatib, F. Tarlochan, Ahmad Hashem, Sadok Sassi, "Collapse behavior of thin-walled corrugated tapered tubes under oblique impact," *Thin-Walled Structures*, vol. 122, pp. 510-528, 2018. (Impact Factor: 2.829)

CHAPTER 1: INTRODUCTION

1.1 Introduction

Safety is one of the most critical concerns to humans in the 21st century. With the vast advancements in science and technology, people started to take being protected and safe during their day-to-day activities for granted. Moreover, this by itself is a great motive to researchers and scientists to improve people's lives by integrating science in applications where safety is of the highest significance to people. One of these most critical applications is the automotive safety.

With the continuously increasing population in our modern world, the rate of demand for transportation rises proportionally. As a result, the number of vehicles, whether they are private automobiles or for public transports, increases. The number of automobile vehicles is expected to reach 1.7 billion by 2035 [1]. Therefore, logically, the probability of engaging in a traffic accident rises, and the number of traffic accidents grows as an inevitable consequence. According to the world health organization, automobile accidents are the main cause of death for people of the age group between 5-44 years old [2]. Traffic accidents result in an approximate of 1.25 million deaths annually while causing around 20-50 million non-fatal injuries [3]. From this information, it is evident that motor vehicle accidents cause huge economic and societal losses globally. Therefore, extensive efforts have been placed to find a solution to this vital problem. As a solution, great focus has been placed on energy absorbing devices that absorb accidents' impact and crash energy. These devices are used as parts of the vehicle's structure to reduce the crash severity and absorb the crash energy in a controllable manner. A device that helps reduce the potential risks of

injury and death to vehicles' occupants involved in an accident is described as a crashworthy device [4]. Hence, crashworthiness is perceived as the most important criteria for safety in automotive. The most common used crashworthy energy absorbing devices category is thin-walled structures (TWS). Thin-walled tubular structures are widely used in the engineering field, specifically, for impact energy absorption applications. The lightweight, low manufacturing cost, excellent energy absorption characteristics and easy installation qualify these structures to be used in applications where safety is vital. Thin-walled structures are used in automotive applications such as passenger cars and trains [5], and aircraft subfloors [6] as shown in Figure 1-1 and Figure 1-2, respectively.

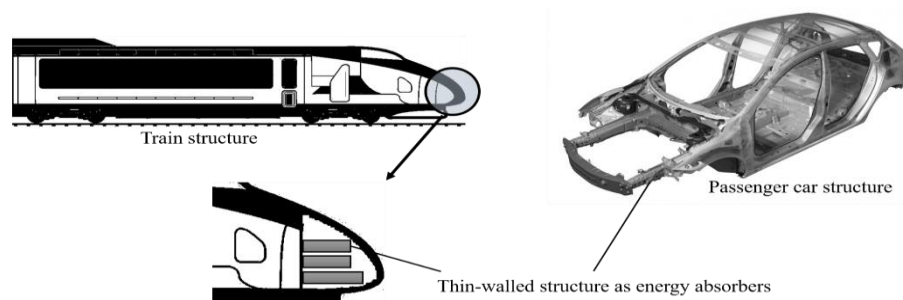


Figure 1-1: Thin-walled structures as energy absorbers in vehicles

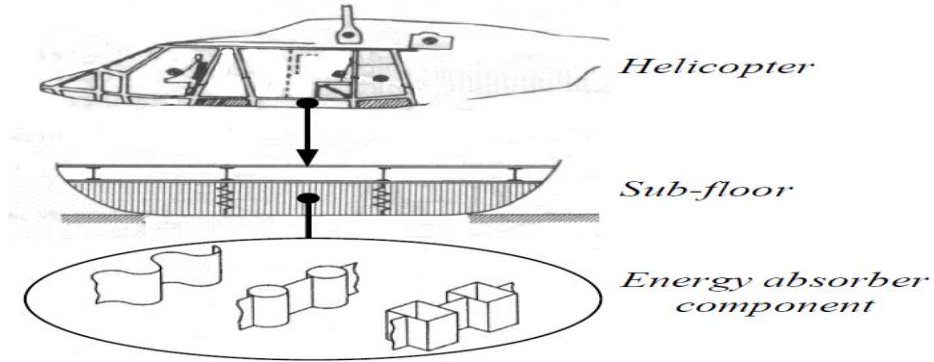


Figure 1-2: Thin-walled structures as energy absorbers in air-craft subfloors [3]

1.2 Thin-walled Structures as Energy Absorbers

The performance of thin-walled structures in energy absorption applications depend mainly on their material, geometry, and type of impact they experience. The most common materials used to manufacture thin-walled structures are ductile metals, such as aluminum and mild steel, as well as composites, specifically fiber-reinforced composite (FRC). There is a significant difference in the energy dissipating mechanisms of thin-walled structures of different materials. Thin-walled structures of ductile metallic materials dissipate the crash energy by undergoing progressive plastic deformation. On the other hand, composites' thin-walled structures dissipate energy by brittle failure either by fiber breakage, matrix cracking, and delamination [7, 8].

Because of their vital energy absorption role in safety applications, there has been a tremendous focus on enhancing the performance of thin-walled structures in occupants carrying vehicles. A lot of research work has studied the effect of different cross-sections on the energy absorption performance of thin-walled components. Structures of circular,

rectangular, polygonal, hexagonal and star-shaped cross sections have been investigated [9-12]. Beside studying various cross-sections, researchers examined the effects of thin-walled structures fillers, specifically metallic foams of non-uniform [13-15], and uniform [16-19] density distribution. Lately, thin-walled structures with various surface patterns have been the focus for many scientists, and have shown significant enhancement in energy absorption and lowering the initial crushing forces. For instance, thin-walled components with surface holes patterns [20, 21] have shown potential in reducing the initial crushing forces. In addition to windowed structures, researchers investigated the effect of surface corrugation on the performance of thin-walled structures. Structures with corrugated surface have shown excellent performance in terms of increasing the specific energy absorption and reducing the initial crushing forces under axial loading conditions [22-25].

However, thin-walled structures do not always experience pure axial impacts in all their applications. Rather, energy absorbers undergo a combination of axial and oblique loads. This is generally the case in vehicular crashes situations as off-set, or oblique impacts account for 48% of all of the frontal impacts category [26]. Oblique loads tend to lead to unstable crushing of the thin-walled tubular structure because they cause the structure to crush in a global Euler buckling mode, and hence reduce the overall energy absorption. Therefore, a lot of the research work has focused on enhancing the performance of these energy absorbers under oblique loading conditions. Structures of conical and tapered layouts were explicitly the focus of many researchers in this area. Researching these structures was because of their resilience under global Euler buckling that exists under oblique loading conditions. This was concluded by Nagel and Thambiratnam [27]

who found that tapered tubular structures offer a steady reduction in crushing forces under oblique impacts and hence have better performance than conventional straight tubular structures. Researchers studied empty, and foam filled tapered structures [28], tapered structures with surface rectangular indentations and cutouts [29-31], tapered structures of functionally graded thickness [32], and tapered tubes of multicellular configurations [33]. The major outcomes of these studies were that tapered tubular structure has better performance under oblique impacts when compared to a conventional straight tube.

The corrugated surface patterns and tapered layout studies provide the most essential characteristics of an ideal energy absorber: (1) lower crushing forces, and (2) resilience to oblique loading conditions. Hence, a tubular structure that combines a corrugated patterned surface and a tapered layout is worth investigating under different loading conditions. Therefore, studying the crushing response and performance of corrugated tapered tubes is vital, as such structures might have the potential to be ideal energy absorbers. In this thesis, the collapse behavior and energy absorption performance of corrugated tapered tubes (CTTs) under axial and oblique loading conditions are examined numerically. The explicit finite element code ABAQUS was used to model the impact and predict the collapse behavior and energy absorption characteristics of CTTs. The model is verified experimentally to assure the accuracy of the results. The effects of the impacting angles and geometrical parameters are investigated to understand the collapse behavior and energy absorption performance of CTTs.

1.3 Objectives and Methodology

1.3.1 Objectives

The primary objective of this thesis is to study the performance of corrugated tapered tubes as efficient energy absorption devices under axial and oblique impact conditions for safety applications. This objective is achieved through the following:

- 1- Developing an experimentally validated finite element model to simulate the crushing of corrugated tapered tubes of different geometrical parameters under axial and oblique loading conditions.
- 2- Investigating the effect of corrugation parameters (Amplitude and Wavelength), and other geometrical parameters on the collapse and crushing modes of corrugated tapered tubes under axial and oblique impacts.
- 3- Investigating the effect of geometrical parameters of corrugated tapered tubes and loading angles on the performance under axial oblique impacts.
- 4- Comparing the energy absorption of conventional tapered tubes and corrugated tapered tubes, and identifying the most important corrugation combination and geometric parameters that lead to the optimum energy absorption performance under axial and oblique loading conditions.

1.3.2 Methodology

This thesis depends mainly on finite element modelling (FEM) to simulate the crushing of the proposed corrugated tapered tubes and obtain their responses numerically. Finite element methods have been used widely in various kinds of studies to reduce costs and time. Therefore, the use of finite element analysis can reduce the time required to run

the crushing simulations. To assure the accuracy of the results obtained from the FE analysis, the FE model was validated against experimental tests. All the FE related work in this research framework, such as modelling, solving, and visualization of the results was done via ABAQUS software. The non-linear explicit code in ABAQUS was used to solve all the simulations presented in the thesis. The material used for all the simulations was aluminum alloy AA6060. The AA6060 alloy properties that were used as inputs to the FE model were obtained by conducting a standard tensile test. The material was also characterized using the built-in Johnson-Cook isotropic model to account for strain hardening.

1.4 Contributions

The research conducted on thin-walled structures have shown promising results in terms of crashworthiness performance. The studies conducted on tapered tubular structures focused on adding foam fillers, studying surface indentations and altering tapered angles. On the other hand, studies on straight tubes with corrugated surface have shown that these surfaces reduce the dynamic crushing forces and offer a smooth and more controllable energy absorption compared to conventional tubes. The ideal energy absorption device must have reduced crushing forces and smooth energy absorption under both axial and oblique loading situations. Therefore, this study proposes a new thin-walled design that has the tapered feature of thin-walled structures and a sinusoidal corrugated surface as a potential ideal energy absorption device. The study investigates the behavior of this design's geometrical parameters under axial and oblique impacts to assess its performance for safety and crashworthiness applications. Moreover, the study identifies the best design

parameter for the proposed structure under axial and oblique loadings.

1.5 Thesis Layout

This thesis is organized as follows:

Chapter 1: Introduction

This chapter introduces the research problem, the current solution to it, and the motive behind the thesis. This chapter also includes the research objectives, a brief methodology, the outline of the thesis, and its contributions.

Chapter 2: Literature Review

This chapter surveys the literature in terms of the work related to the research problem. The chapter is divided into logical categories that explain the flow of the research work done on enhancing thin-walled structures. This chapter finally outlines the reason behind studying the proposed corrugated tapered tubes.

Chapter 3: Methodology

The methodology chapter highlights the experiment design for both the axial and oblique crushing simulations. In addition, it presents the finite element model description and corrugated tapered tubes geometrical parameters. It finally explains the finite element model validation process.

Chapter 4: Corrugated Tapered Tubes Under Axial Loading

This chapter underlines the performance of corrugated tapered tubes under axial impact. The force-displacement characteristics for CTTs of different geometrical parameters are discussed. It also discusses the developed collapse modes experienced by CTTs under axial impacts. Finally, the chapter explains the effect of geometrical

parameters on energy absorption, specific energy absorption, initial peak force and mean force.

Chapter 5: Corrugated Tapered Tubes Under Oblique Loading

This chapter discusses the performance of CTTs under oblique loading conditions. The chapter highlights the effect of loading angle and geometric properties on the force-displacement characteristics. The chapter also discusses the crushing behavior of CTTs and their transition to global Euler buckling under high impact angles. Finally, the chapter discusses the performance patterns of CTTs of different geometrical properties under different loading angles.

Chapter 6: Conclusions

The main findings and conclusions drawn from the thesis research framework are listed in this chapter.

Chapter 7: Recommendations for Future Work

This chapter highlights some suggestions and recommendations for future research for further understanding and enhancement to the proposed corrugated tapered tube design in this thesis.

CHAPTER 2: LITERATURE REVIEW

2.1 Introduction

This chapter reviews the areas of literature related to the thesis topic up to this date. The literature survey covers various areas that discuss all the theoretical aspects and studies conducted in a way that explains the motivation behind undertaking the research conducted in this thesis. These areas will be addressed as follows:

- (1) Structural Crashworthiness
- (2) Structural Impact
- (3) Energy Absorption by Structural Collapse
- (4) Thin-walled Structures
- (5) Finite Element Modeling of Thin-Walled Structures

2.2 Structural Crashworthiness

The “Crashworthiness” term was used in aviation initially to refer to the capability of the aircraft in providing safety to its occupants in potential survivable crash situations. Later, the automotive safety community adopted and embraced the term and designated it to describe the passengers' safety performance exhibited by different categories of automobiles and automotive vehicles under different crash conditions [34]. Crashworthiness denotes the ability of occupants-carrying vehicles to withstand and undergo the crash impact without penetrating the occupant's compartment so that they can survive the crash without injuries. Hence, the structural crashworthiness research field can be defined as the field that investigates the behavior and performance of structures under impact situations [35]. Certain characteristics define structural

crashworthiness which should be taken into consideration in occupants-carrying vehicles' designs. The main crashworthiness characteristic is the energy absorption management [34]. Research has shown that the occupant's safety and survivability depend mainly on the vehicle management of the crash kinetic energy. The frontal structures of an automobile vehicle or the subfloor structures of an aircraft should absorb the impact energy while maintaining minimum to no deformation to the occupants' compartment. If a structure achieves this characteristic, it could be used as an effective energy absorbing device in occupants' carrying vehicles. Furthermore, the structure should keep the occupants' compartment at the lowest deceleration level possible, to reduce the potential chances of injuries [36].

Crash-boxes have been extensively used in automotive safety applications to absorb the crash energy and protect the occupants. These structures are small shell tubes and are mainly used in automobile vehicles. In a vehicle, they are usually connected to the chassis frame as shown in Figure 2-1. In a crash situation, these structures deform to absorb the impact energy, and then they can be replaced after accidents. In general, a crashworthiness study focuses on different aspects mainly, the vehicle dynamics during and after the crash, the occupant's motion during the crash, and the collapse behavior of the crash-box structure [37]. However, this thesis focuses only on the structural collapse behavior aspect of crashworthiness studies.

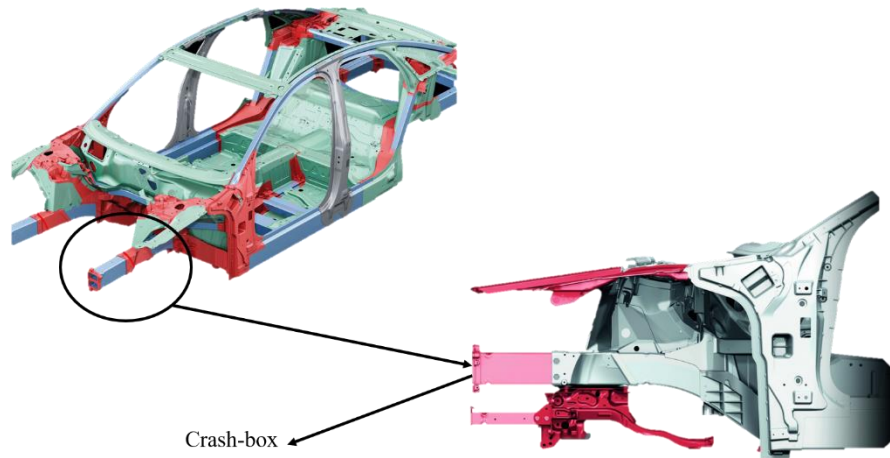


Figure 2-1: Front chassis crash-boxes as energy absorbers

2.3 Structural Impact

The deformation behavior and energy absorption of thin-walled energy absorbing devices depend on the nature of loading, strain rates, and inertia effect. Since this thesis focuses mainly on the collapse behavior of thin-walled corrugated tapered tubes under impact, the following areas of impact mechanics, effects of strain rates, and influence of inertia are addressed.

2.3.1 Quasi-static and Dynamic Loading

Under impacts, structures behave differently according to the nature of the impact. When the impact is static or quasi-static, the effect of strain and inertia on the structure under impact is insignificant or negligible. However, when the impact is of a dynamic nature, the inertia and strain will affect the behavior of the structure and its deformation shape. Under axial loading, the thin-walled tubular structure (shell-tube) deforms in a

stable manner forming lobes (folds). The process of lobe formation under loading is known as progressive buckling or crushing. According to Karagiozova and Jones [38], progressive buckling consists of two categories: quasi-static and dynamic buckling. As evident by their names, the major difference between the two is the nature of loading they develop under: quasi-static buckling under low-velocity impacts, and dynamic buckling under high-velocity impacts. Another significant difference between the two categories is that dynamic buckling utilizes the whole tubular structure under deformation, and is governed by the effect of stress wave propagation [4]. Figure 2-2 depicts the deformation shapes of a circular tube under quasi-static and dynamic progressive buckling.

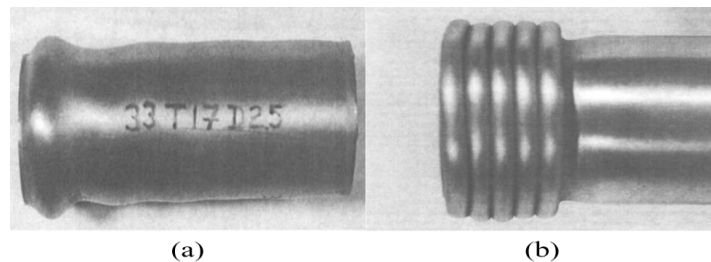


Figure 2-2: Progressive buckling of circular tubes under (a) dynamic loading; (b) quasi-static loading [4]

2.3.2 Strain Rate Sensitivity

The mechanical properties of the absorbing structures' materials have a vital influence on the structures' response to impacts. The variation in properties such as yield strength and strain hardening leads to a significant difference in terms of crashworthiness

performance for different materials. Metallic materials, which are widely used as energy absorbers, have different properties under different loading/impact rates, and hence they are generally sensitive to strains. For example, mild steel, aluminum, and magnesium alloys are greatly sensitive to strain rate [39-41]. The effect of strain sensitivity is considered to be beneficial to thin-walled energy absorbers because when there is an increase in strain rate, the values of yield and ultimate strengths increase. It is worth mentioning that strain rate sensitivity is an exclusive material characteristic and is not related to the geometry or shape of the energy absorbing structure [4].

For engineering applications, the effect of strain rate sensitivity is considered by using dynamic flow stress rather than static stress. Researchers have developed explicit rate-dependent constitutive models that describe the dynamic flow stress and consider the influence of the strain-rate sensitivity. One of the most popular models that have been used for structural impact applications is the Cowper-Symonds model [42]. This empirical model has been experimentally validated and used to understand the strain effect on the crushing behavior of tubular structures [43]. The constitutive model can be described as follows:

$$\sigma_d = \sigma_s \left(1 + \left(\frac{\dot{\epsilon}}{D} \right)^{\frac{1}{q}} \right) \quad (2-1)$$

where σ_d is the dynamic stress, σ_s is the static stress, $\dot{\epsilon}$ is the strain rate, and D and q are material's constants. Another constitutive model that describes the dynamic flow stress in terms of strain rate is the Johnson-Cook model. The Johnson-Cook model is used widely in applications where the strain rate has a huge range, and plastic deformation changes the temperature because of thermal softening [11]. The model characterizes the flow stress of

material in terms of different functions: strain hardening, strain rate strengthening, and thermal softening, which can be combined in three terms respectively as in Eq. (2-2) [44]:

$$\sigma = [A + B\varepsilon^n] \left[1 + C \ln \left(\frac{\dot{\varepsilon}}{\dot{\varepsilon}_0} \right) \right] \left[1 - \left(\frac{T - T_{room}}{T_{melt} - T_{room}} \right)^m \right] \quad (2-2)$$

Where σ is the material flow stress, ε is the plastic strain, $\dot{\varepsilon}$ is the strain rate, and $\dot{\varepsilon}_0$ is the reference strain rate. T is the structure's surface temperature, T_{melt} is the material melting point, and T_{room} is the room temperature. The parameters A , B , C , n and m are five empirical constants [45]. The significance of these models lies within the ability of incorporating them into material models for finite element analysis, which was the case with the Johnson-Cook model that was used in this thesis. There are other constitutive models that account for strain sensitivity. Developing these models requires an in-depth understanding of the behavior of the material under high strain rates and loading conditions to accurately describe its stress-strain relation. Other material models that account for strain-rate sensitivity for different metals are Khan–Huang model, Zerilli–Armstrong model, and Bodner–Partom model [46].

2.3.3 Effects of Inertia

Under severe impact conditions, the effect of inertia plays a significant role in influencing the deformation shape and collapse behavior of thin-walled structures. When the impact is of high velocity, the effect of inertia changes the initial peak forces, force-displacement characteristics, and deformation mode of the tubular structures under impact. Various research work has been conducted to understand the effect of impacts of high velocity and the influence of inertia on the collapse behavior of thin-walled tubular structures.

The influence of inertia on structures depends mainly on the nature and geometry of the structure, in addition to the crash characteristics (velocity and mass). Calladine and English [47] have studied two common types of energy absorbers as shown in Figure 2-3: Type I: characterized by an initially increasing force curve that flattens after reaching a certain point, and Type II: characterized by an initial peak force that drops significantly afterward. Their research has shown that behavior of the Type I absorber is not influenced by the impact velocity. On the other hand, the collapse behavior of Type II absorber is significantly influenced by the impact velocity and hence influenced by inertia.

Karagiozova et al. [48] have studied the effect of inertia on circular thin-walled tubular structures using structures of different geometrical characteristics and strikers of different masses and velocities. The results of the conducted research showed that the stress wave propagation effects govern the dynamic buckling process as mentioned in section 2.3.1. In addition, the findings showed that the collapse behavior of the studied structures is influenced significantly by the impact velocity and the impactor mass. For instance, when the impact mass is small, and the impact velocity is high, a larger amount of energy is absorbed by the impacted structure. This was explained by the accumulation of larger strains and stresses in the structure in the early phase of compression. Additionally, a low-velocity impact would cause an irregular compression which shortens the structure length significantly. The same shortening phenomenon occurs to structures under high-velocity impacts, however, in the early phase of deformation, before buckling takes place.

Wang and Lu [49] have also studied the effect of high impact velocity on the deformation modes of circular tubular structures. The structures were subjected to axial

loads of up to 300 m/s velocity. The results have shown that impacts of high velocities lead to a specific type of plastic deformation known as “Mushrooming”. Three deformation modes were observed for the tested circular structures as shown in Figure 2-4. The first one is a regular progressive crushing mode which was observed for tubular structures of small shell thickness under low-velocity impacts. The second mode was the mushrooming mode accompanied by some folds for structures under impacts of medium velocity. The final mode was mushrooming with wrinkles for structures of large wall thickness under impacts of high velocity.

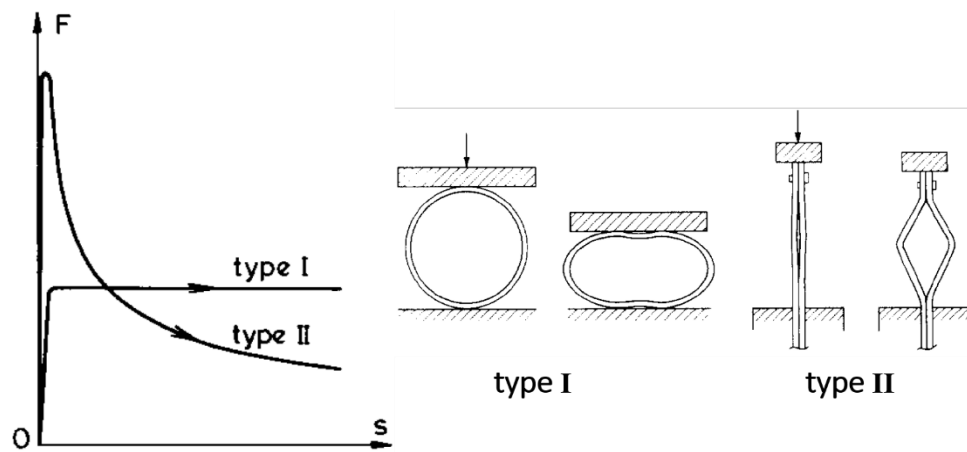


Figure 2-3: Two common types of thin-walled energy absorbers [48]



Figure 2-4: Steel circular tubes under the following velocity from right to left: 385 m/s, 277 m/s, 227 m/s, 173 m/s and 0 m/s [49]

2.4 Energy Absorption by Structural Collapse

The performance of thin-walled energy absorbers can be evaluated qualitatively and quantitatively using different methods and equations. Before the evaluation, however, certain general principles need to be followed in designing and using thin-walled energy absorbers. The following sections will explain these principles and the formulas that can be used to measure them to assess the performance of energy absorbers.

2.4.1 Energy Absorber: General Principles

According to Lu and Yu [50], there are general principles that scientists and vehicle manufacturers should consider before designing or testing new energy absorbers. Even though each design goal needs certain principals, and therefore principles may vary from certain application to another. However, these principles are fundamental to all energy absorption applications. The following sections summaries the key principles for designing energy absorbers.

2.4.1.1 Irreversible Conversion of Energy

The kinetic energy that results from the crash should be converted by the absorbing structure to an inelastic/plastic form of energy by either plastic deformation or any other process. If an absorbing structure fails to convert the crash energy, and rather stores it elastically, after a certain point where the structure reaches maximum elastic deformation, this energy will be released leading to potential injuries to the occupants of the vehicle. This idea can be clarified by an example of a vehicle impacting a large spring. Instantly, the spring will store the kinetic energy of the vehicle by compression. After the spring reaches its maximum elastic deformation, the spring will release its stored energy and the vehicle will bounce off it as shown in Figure 2-5. This means that the occupants will feel severe deceleration at the moment of impact and a severe acceleration afterward, which might lead to serious injuries to the occupants. The same idea applies to an energy absorber that is not capable of converting the energy plastically.

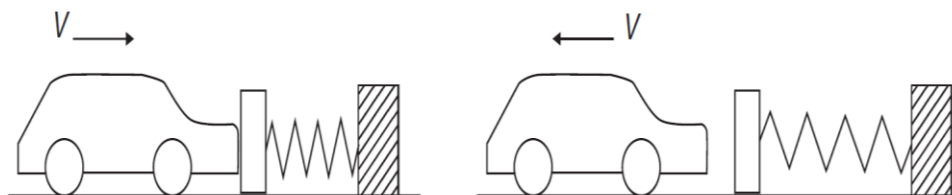


Figure 2-5: A vehicle impacting a large elastic spring that does not convert the kinetic energy [50]

2.4.1.2 Constant Reaction Forces

The crushing forces during the deformation process of an energy absorber should be kept to a minimum and below a specific threshold, especially the initial peak reaction force. Despite the fact that energy-absorbing structures should provide enough energy absorption, however, the crushing forces should not pass a specific value. This is because large crushing forces will lead to higher deceleration levels, leading to severe injuries to the occupants. Occupants riding a vehicle will have approximately the vehicle's acceleration, and if the reaction forces during an impact are high or fluctuating, the occupants will be susceptible to severe injuries.

2.4.1.3 Long Stroke

Although the reaction forces should be minimized and kept constant throughout the crushing process (during a crash), the energy absorbed should be enough to mitigate the crash energy from reaching the occupants' compartment. The energy absorbed represents the work done by the force on the structure, and this work equals the force times the displacement of the force line. This displacement represents the stroke of the structure, and hence it should be of sufficient length to absorb enough energy. Additionally, the longer the stroke, the longer the energy absorption process is. This is vital for energy absorption applications as more time means that the crushing forces are being maintained for a longer time, hence the structure will be able to arrest the crushing forces gently. This will lead to lower decelerations felt by occupants and hence reduce the severity of potential injuries.

2.4.1.4 Stable and Repeatable Deformation Mode

The structure should be able to deform stably in a predictable manner and repeatable deformation mechanism. This is essential to energy absorption and vehicle safety applications as it indicates that the structure is reliable under different crash situations. It was discussed previously that the types of impact's nature in terms of velocity and inertia play a vital role in influencing the deformation modes, force-displacement characteristics and structure's collapse behavior in general (refer to section 2.3). Therefore, a structure that is being considered for energy absorption and safety applications should be able to deform in a stable and predictable manner under all possible crash situations.

2.4.1.5 Light Weight

Weight is an important aspect to consider when designing a new energy absorber. This is precisely important for vehicle manufacturing companies where vehicle weight is essential. Structures of high weight increase the fuel consumption and hence has adverse effects on the environment. Therefore, designing a new energy absorbing structure should consider different kinds of materials and geometric modifications that lead to high energy absorption and low weight simultaneously.

2.4.1.6 Low Cost

Energy absorbing devices are essentially sacrificial devices, and their sole purpose is to deform to save the lives of the occupants. Therefore, it is reasonable that these structures should not be expensive. The cost of these structures is comprised of the material and the manufacturing cost. Hence, using materials that are recyclable is an important aspect of designing such structures. Also, manufacturing methods that are inexpensive

should be used to produce these structures if their design makes it possible.

2.4.2 Performance Indicators

The performance of the tubular structure can be assessed qualitatively and quantitatively. The qualitative assessment includes the overall collapse behavior of the structure, the force-displacement characteristics, and final deformation modes. The quantitative analyses, on the other hand, includes quantifying some of the principles mentioned in the previous section. The quantitative performance indicators are illustrated in the typical force-displacement diagram shown in Figure 2-6, which are explained in the following sections. These performance indicators were also used to assess the performance of the corrugated tapered tubular structure proposed in this thesis.

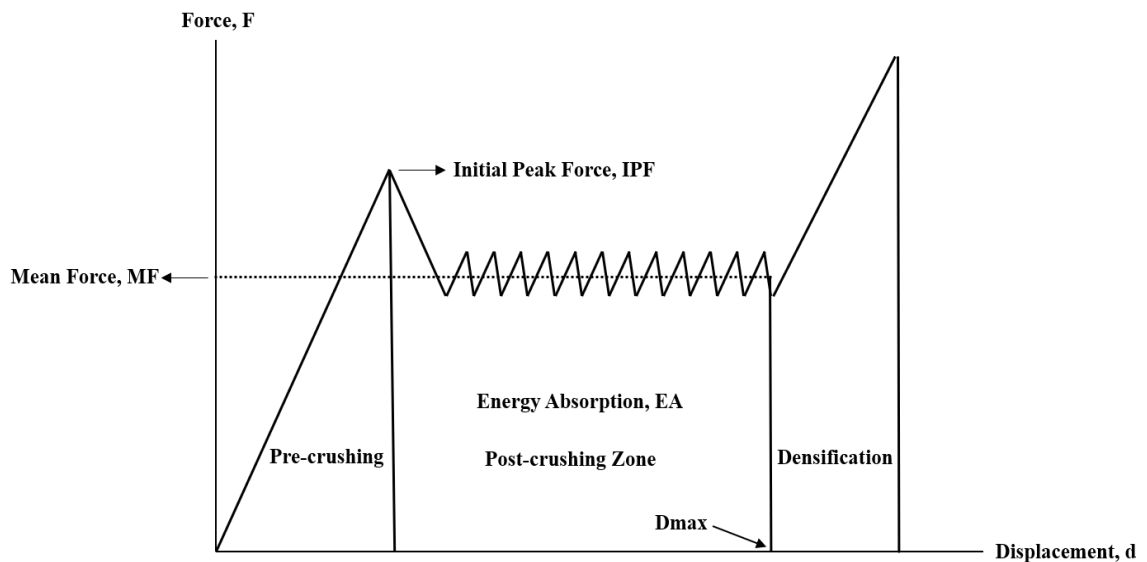


Figure 2-6: Typical force-displacement diagram

2.4.2.1 Initial Peak Force

The initial peak force (*IPF*) is the largest force needed to start deforming and collapsing the tubular structure. A low *IPF* value is desirable as it reduces the reaction forces which prevent passenger's injuries in safety applications such as automotive.

2.4.2.2 Mean Crushing Force

The mean crushing force (*MF*) is the average crushing experienced by the tubular structure:

$$MF = \frac{EA}{D_{max}} = \frac{\int_0^{d_{max}} F ds}{d_{max}} \quad (2-3)$$

Where *EA* is the energy absorption, and *D_{max}* is the displacement point up to the densification zone shown in Figure 2-6.

2.4.2.3 Energy Absorption and Specific Energy Absorption

The energy absorption is measured to evaluate the capability of the tubular structure to dissipate the impact energy by plastic deformation. The absorbed impact energy represents the area under the force-displacement curve depicted in Figure 2-6. The absorbed energy is calculated as follows:

$$EA = \int_0^{D_{max}} F ds \quad (2-4)$$

Where *F* is the crushing force, and *D_{max}* is the longest length point where the tubular structure reaches the maximum amount of deformation. The specific energy absorption (*SEA*), on the other hand, is calculated to assess the energy absorbed by the structure to its mass:

$$SEA = \frac{EA}{m} \quad (2-5)$$

Where m is the crushed mass of the structure.

2.5 Thin-Walled Structures as Energy Absorbers

Thin-walled structures as energy absorbers are generally a part of an energy absorbing system. For instance, thin-walled energy absorbers represent the frontal section that is connected to the frontal longitudinal of the vehicle's chassis or the small crash boxes that go in aircrafts subfloors as mentioned in Chapter 1. To thoroughly understand the behavior of thin-walled structures under crash situations, it is necessary to test and study the whole energy absorbing system containing these thin-walled structures. However, due to cost and time difficulties, a lot of the conducted research in the area tends to study thin-walled energy absorbers individually. Although studying these structures individually does not accurately reflect the real-life crash situations because of the complicated boundary conditions that exist in a real crash [51], however, analyzing these structures individually gives an indication of their collapse behavior and energy absorption performance. This section comprehensively reviews the thin-walled energy absorbers that have been studied and analyzed for energy absorption applications in the open literature.

2.5.1 Circular Tubes

The focus on circular tubes was huge due to their energy absorption efficiency, and a lot of early research work studied their behavior under axial impact [43, 52, 53]. Gameiro et al. [54] stated that circular tubular structures were the most widespread of energy absorbers because they experience constant crushing load under impact. Under axial impact, circular tubular structures undergo progressive crushing or buckling behavior, with three main deformation modes: (a) axisymmetric mode, (b) diamond or non-axisymmetric

mode, and (c) mixed mode that combines the first two as shown in Figure 2-7.

The developed deformation modes in circular tubes depend mainly on the geometric properties of the structures, and mainly the diameter to thickness (D/t) and length to thickness (L/t) ratios [55]. Table 2-1 lists the D/t , and L/t ratios' ranges and the corresponding developed deformation mode. A related point to consider is that the axisymmetric mode is the most stable one and allows for maximum energy absorption.

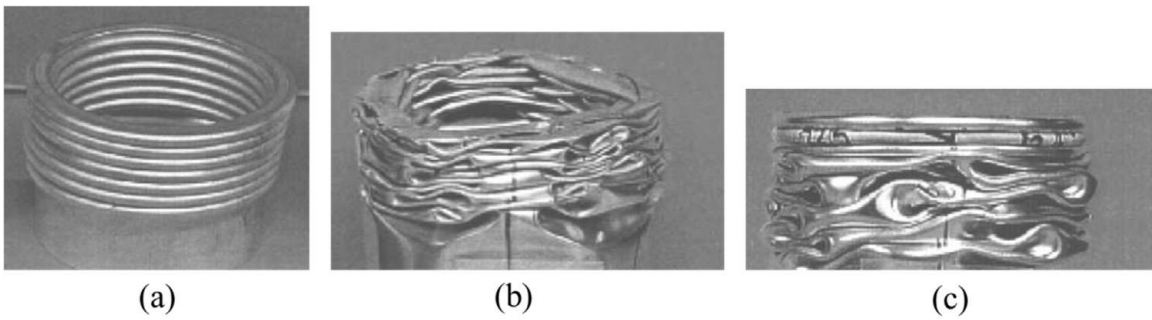


Figure 2-7: Circular tubes deformation modes: (a) axisymmetric mode; (b) non-axisymmetric or diamond model; (c) mixed mode [58]

Table 2-1: Developed deformation modes in circular tubes according to their D/t and L/t ratios [55]

Diameter to thickness ratio (D/t) & length to thickness ratio (L/t)	Developed deformation mode
$D/t > 80$	Diamond mode
$D/t < 50$ and $L/t < 2$	Axisymmetric mode
$D/t < 50$ and $L/t > 2$	Mixed mode

Beside experimental testing of circular tubular structures, a lot of research work has developed theoretical equations of the mean crushing force of circular tubes. These equations predict the average crushing force for different developed deformation modes such as asymmetric [56, 57] and axisymmetric [52] modes. Guillow et al. [58] developed an empirical equation that predicts the mean crushing force (MCF) for all types of circular tubular structures:

$$MCF = 18.075 \sigma_0 t^2 \left(\frac{D}{t}\right)^{0.32} \quad (2-6)$$

where σ_0 is the flow stress, D is the diameter, and t is the thickness.

2.5.2 Square Tubes

The focus of research has shifted to square tubes because of the practicality of square tubes in their attachments to other structural members such as automotive vehicles. The main issue with square tubular structures is that they are less efficient when compared to circular tubes. A square tube is approximately only as 70% efficient as its circular tube counterpart in terms of energy absorption performance [59]. This reported reduction in efficiency is related to the fact that the maximum amount of deformation occurs only on the square tube's corners. The developed deformation modes in square tubes under axial impact can be divided into two categories: compact and non-compact modes as shown in Figure 2-8 [60]. The compact modes include: (a) extensional mode, (b) inextensional mode, and (c) asymmetric mixed-mode [4]. The deformation modes exhibited in square tubular structures, like the circular tubes, depends on the geometrical configurations of the tube, mainly the width (b) to thickness (t) ratio [60].

Table 2-2 lists (b/t) ratio ranges and the corresponding developed deformation

modes in square tubes. Similar to circular tubes, scientists and researchers developed many theoretical equations for the mean crushing force of square tubes under axial impacts. Wierzbicki and Abramowicz [61] developed one of the first theoretical equations for MCF for square tubes of different deformation modes:

$$MCF = 9.56 \sigma_0 b^{\frac{1}{3}} t^{\frac{5}{3}} \quad (2-7)$$

This equation was updated later by Abramowicz and Jones to include the effect of strain hardening [52]:

$$MCF = 13.06 \sigma_0 b^{\frac{1}{3}} t^{\frac{5}{3}} \quad (2-8)$$

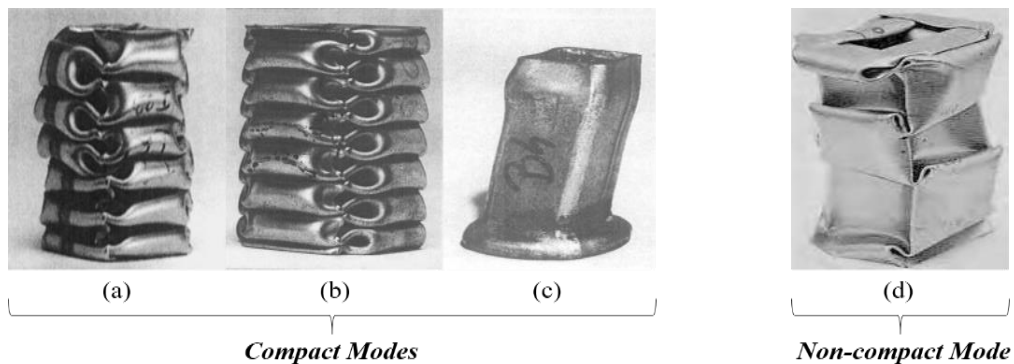


Figure 2-8: Deformation modes in square tubes: (a) asymmetric mixed mode, (b) inextensional mode, (c) extensional mode, and (d) non-compact mode [4]

Table 2-2: Developed deformation modes in square tubes according to their b/t ratios [60]

Width to thickness ratio (b/t)	Developed deformation mode
b/t < 7.5	Extensional mode
b/t > 40.8	Inextensional mode
7.5 ≤ b/t ≤ 40.8	Asymmetric mixed mode
b/t = 100	Non-compact mode

2.5.3 Tubes of Different Cross-Sections

Studying thin-wall structures of different geometrical modifications has received a massive focus by researchers to investigate the crashworthiness capability of novel thin-walled tubular designs. One of these geometrical modifications was studying structures of different cross sections than the conventional circular and square ones. The thin-walled structures that have been studied in the literature are grouped into two categories: (1) outward (convex) multi-corner tubes, and (2) inward multi-corner tubes.

Tubular structures of multi-corners were inspired by the observation that square tubes' maximum deformation occurred at the corners' zones as mentioned in section 2.5.2. Hence, a structure with a cross-section of multiple corners such as an octagonal or hexagonal will result in higher energy absorption. This was evident in the developed theoretical equation by Abramowicz and Wierzbicki [62] for the mean crushing force of hexagonal tubes:

$$MCF = 20.23 \sigma_0 b^{0.4} t^{1.6} \quad (2-9)$$

Where b is the maximum width of the tube. Similar to square tubes, multi-corner tubular structures exhibit extensional, inextensional and mixed modes [63]. The developed mode depends on the angle between the side walls of the structure [64]. An inextensional mode

will develop if the angle between the side walls is an acute angle, while a mixed mode will develop when the angle is between 90° and 120° , and finally, an extensional mode will develop at an angle of 120° . It is worth mentioning that a mixed mode will result in the maximum energy absorption [65].

It was found that no further enhancement of energy absorption is possible when the number of corners exceeds 11 corners [66]. This is due to the fact that after 11 corners the condition that satisfies the development of mixed mode deformation (maximum energy absorption) is no longer viable [65]. To overcome this issue scientists have studied structures with inward corners such as star [9] and criss-cross [67] sections structures as shown in Figure 2-9. The results have indicated that these the criss-cross structures have led to a higher crushing force efficiency and specific energy absorption when compared to other structures with convex cross-sections such as rectangular, square, hexagonal and octagonal. Similarly, it was found that a structure with a star-shaped cross-section has better specific energy absorption performance when compared to a structure of a hexagonal cross-section of the same area.

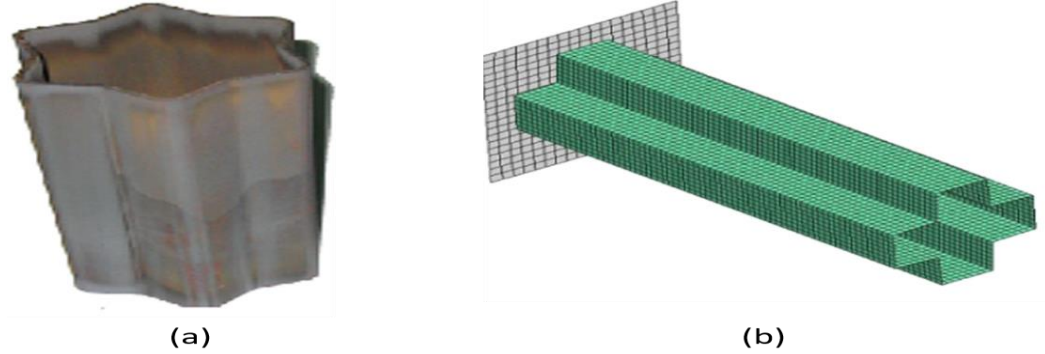


Figure 2-9: inward multi-corner tubes: (a) star-shaped cross-section tube [9]; (b) criss-cross cross-section tube [67]

2.5.4 Multicellular Tubes

Multicellular tubes were explored as an alternative solution to the multi-corner tubes problems with energy absorption limitation after increasing the number of corners. The energy absorption of multicellular thin-walled structures depends mainly on the number of the cells. The mean crushing force experienced by a multi-cellular tubular structure under quasi-static load is given by [68]:

$$MCF = \sigma_0 t \sqrt{(N_c + 4N_o + 2N_T) \pi L_c} \quad (2-10)$$

where N_c is the number of corners, N_o is the number of crisscrosses, N_T is the number of T-shaped cross sections, and L_c is the length of the cross-section walls as shown in Figure 2-10. From the equation, it is evident that increasing the number of cells (more crisscrosses and t-shaped elements) would result in higher energy absorption, which means that a multicellular tube is superior to a simple one in terms of energy absorption. This was proved by Xiong and Hui [69], in which they reported that tubes of 4 and 5 cells (s4 and

s5) shown in Figure 2-11, have higher energy absorption than tubes of single cells, with energy absorption increase of 120% and 220% for s4 and s5, respectively. It has also been proved that tubes of multicellular configurations result in 50-100% higher energy absorption compared to foam filled tubular structures [70]. The multicell configuration has also been studied on many structural layouts such as square [71], circular [72], octagonal [73], and hexagonal tubes [74].

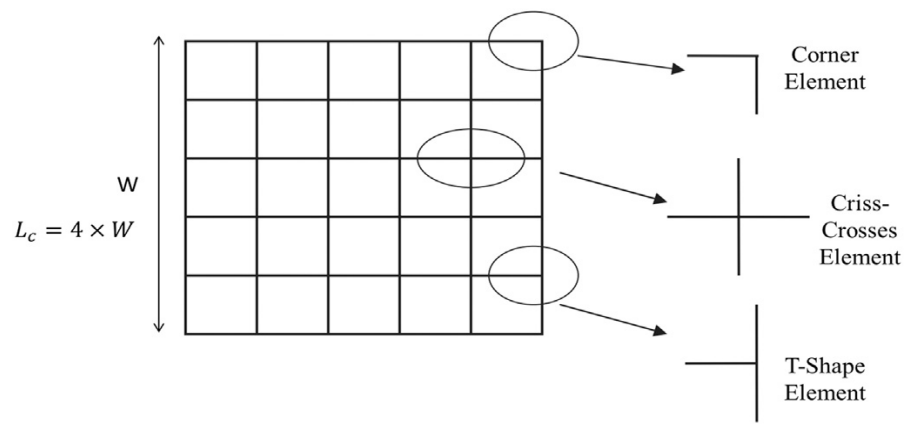


Figure 2-10: multicell tubes: corners and angle elements [68]

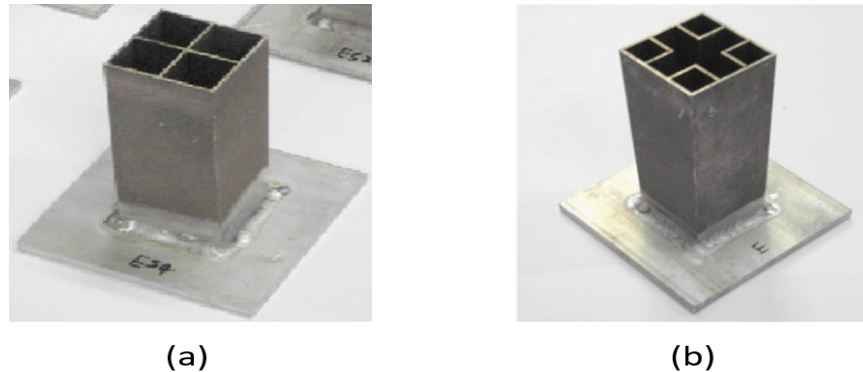


Figure 2-11: Multicellular configurations on thin-walled structures: (a) 4-cells: s4; (b) 5-cells: s5 [69]

2.5.5 Tubes of Functionally Graded Thickness (FGT)

Functionally graded thickness is a novel method introduced by researchers to enhance the energy absorption and crashworthiness characteristics of thin-walled structures. The idea of thickness grading is that the tube's wall will have non-uniform thickness across specific directions in a particular increasing or decreasing gradient. The gradient direction could be longitudinal, or transverse as shown in Figure 2-12. The advantages of grading the surface thickness are having better specific energy absorption, weight efficiency, and lower initial crushing forces [75]. Generally, lower thickness is assigned to the upper portion of the tubular structure to lower the initial crushing force, and larger thickness is assigned to the lower portion of the tube to allow for higher energy absorption [76].

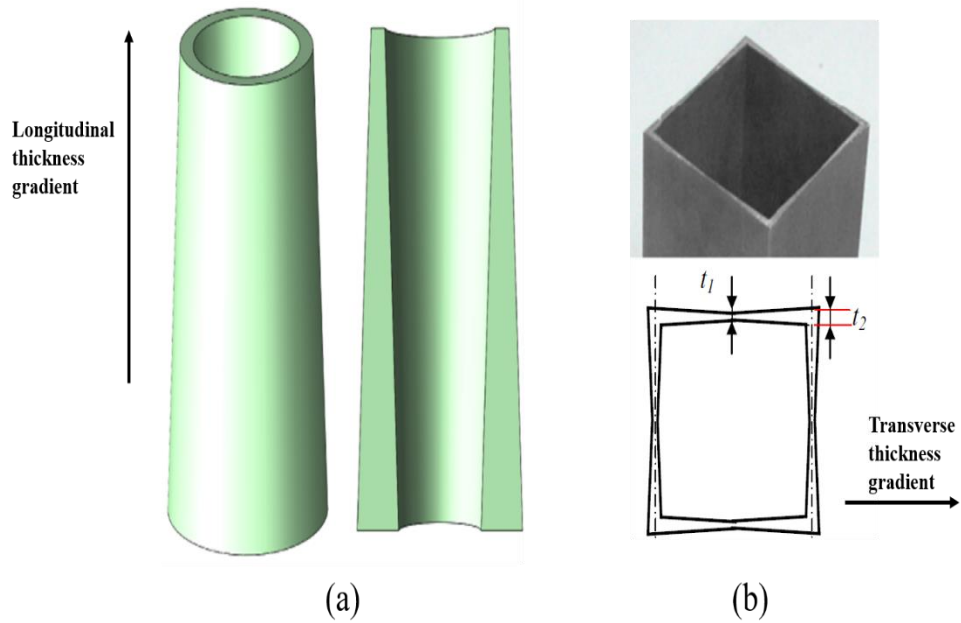


Figure 2-12: Thickness gradient direction in FGT tubes: (a) longitudinal in conical tubes [79]; (b) transverse in square tubes [77]

FGT has been studied on different thin-walled structures of different cross-sections. Zhang et al. [77] studied functionally graded square tubes and found that FGT enhances the energy absorption and increases the mean crushing force to 30-35%. Also, Li et al. [78] studied circular tubes of functionally graded thickness. The results have shown that FGT of grading exponents above 0.1 achieves better energy absorption performance and have better resistance to global Euler buckling at high impact angles. Furthermore, conical tubes of functionally graded thickness have been studied [79]. The results have shown that tubes with proper grading thickness exponents reduce the initial peak force and provide resistance to global Euler buckling.

2.5.6 Foam-Filled Tubes

Foam-fillers and foam-filled tubular structures have been the focus of many researchers due to their lightweight and excellent energy absorbing capabilities. Many foam fillers have been studied, but the most commonly used ones are polymeric and metallic foams [75]. The mechanical behavior of metallic foam fillers relies on the cell microstructure, the material properties and the density of the foam filler [80]. The advantage of foam fillers is that they crush at nearly a constant force, making their use as fillers in thin-walled structures beneficial in terms of energy absorption and reduced crushing forces [75].

Many studies in the literature have been conducted on foam-filled tubular structures of different cross-sections and under various types of loads. Various foam filled tubes of different cross-sections such as square [81], circular [82], and hexagonal [83] have been studied. The results of these studies have shown that foam fillers enhance the energy absorption and the weight efficiency of thin-walled tubular structures. Foam-filled tubes tend to deform compactly with a large number of folds compared to hollow tubes as shown in Figure 2-13 [56]. Also, the presence of a foam filler in a tubular structure changes the developed deformation mode from diamond mode to axisymmetric concertina mode [56], as shown in Figure 2-13. The reason behind these changes in the deformation modes (compared to hollow tubes) is the interaction effect between the filler material and the tubular structure's wall. The presence of the foam filler material in the hollow tube increases the resistance to fold formation, and therefore the fold length shortens and the number of folds increases [84].

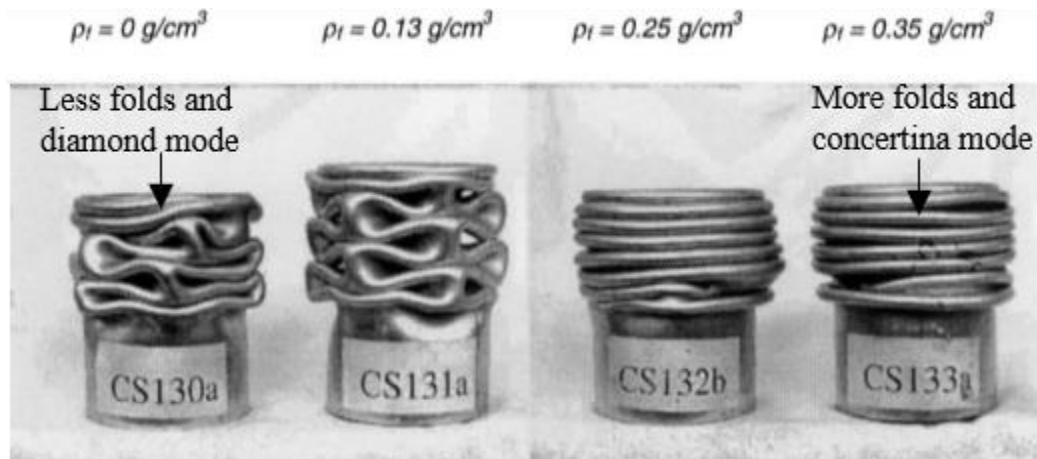


Figure 2-13: Modes of deformation of foam filled circular tubes of different foam densities [56]

The density of the foam filler material is the most influential factor on the behavior of the foam filled tubular structure under crushing. The higher the foam filler density, the higher the energy absorption. However, it was found that when the foam density passes a certain value, adverse effects on the performance may occur such as lower specific energy absorption and global Euler buckling deformation mode [85]. For example, it was found that a using polyurethane foam of 320 kg/m^3 density in square thin-walled structure may lead to the development of global Euler buckling [86]. This has led researchers to study different variations of foam densities including metallic foams of non-uniform density distribution [13-15]. The results of their work showed that metallic foam fillers of non-uniform density could improve the overall specific energy absorption if designed correctly.

2.5.7 Tapered & Conical Tubes

One crucial aspect of energy absorption applications, which has received a considerable interest by researchers, is the capability of the structure to absorb energy under oblique loading impacts. An oblique impact occurs when a structure is impacted with an angle or off its central axis. Oblique impacts introduce what is known as global Euler buckling failure that inhibits the structure to utilize its full energy absorption capacity as shown in Figure 2-14. Global Euler buckling also occurs under axial loading conditions in both circular and square tubular structures. The development of global Euler buckling in structures depends mainly on the diameter to thickness (D/t) and length to diameter (L/D) ratios [58]. It was also found that there is a critical length in which if a structure exceeds it will undergo global Euler buckling under axial crushing [87]. It was also found that a square tube with a higher width to thickness (b/t) ratio, or a circular tube with a higher diameter to thickness (D/t) ratio have higher critical length and hence are more resilient to global Euler buckling [87].

One of the solutions to this issue was studying the tapered or conical structural layout which was found to be resilient under global Euler buckling, and offer a steady reduction in crushing forces relative to conventional straight tubes [27]. The energy absorption and crashworthiness characteristics of tapered thin-walled structures are generally dependent on the geometry of the structure such as the inclination angle, length, cross-section and thickness [88]. Despite showing good performance under oblique loading condition, tapered tubes were reported to have lower specific energy absorption when compared to conventional square straight tubes under axial loading conditions [44].

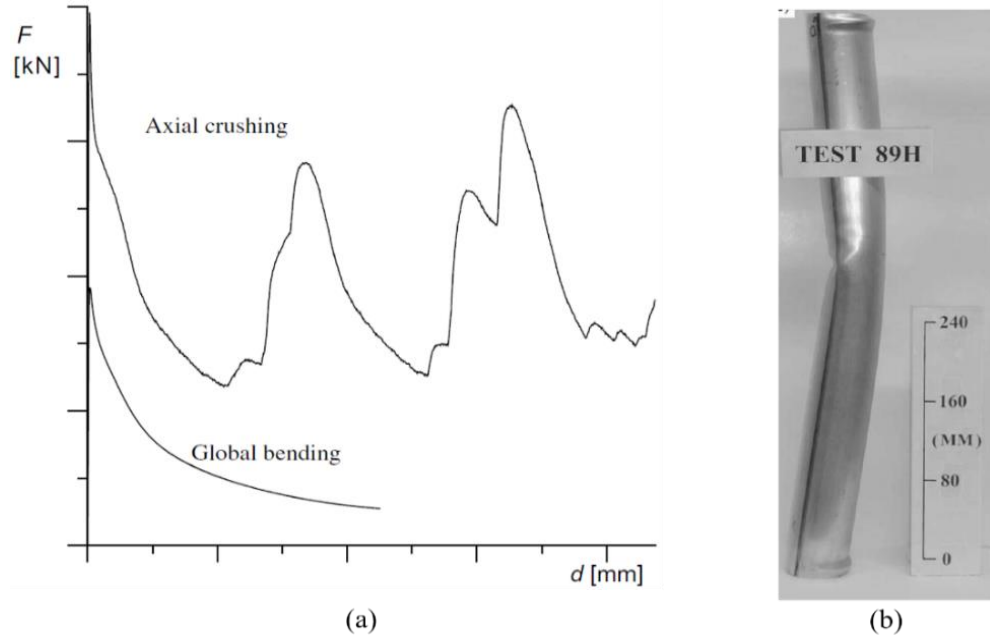


Figure 2-14: Global Euler buckling in thin-walled structures: (a) Force-displacement profile for tubes undergoing global Euler buckling [89]; (b) Global Euler buckling in a circular tube [58]

Tapered tubular structures have been studied extensively by researchers. Tapered tubular structures can have many cross-sections, but the most commonly used ones are the circular and square cross-sections. It was found that a tapered tube of a circular cross-section (conical tube) has the most efficient energy absorption characteristics when compared to tapered tubes of other cross-sections such as square and hexagonal (Figure 2-15) [88]. Researchers have also studied other geometrical modification of tapered structures such as conical tubes with foam fillers, tapered tubes of surface patterns [29, 30], tapered tubes of multi-cellular configurations [33], and conical tubes of functionally graded thickness [32]. Similar to the conventional tubes, tapered tubes have three deformation

modes: axisymmetric, asymmetric, and mixed mode [90].

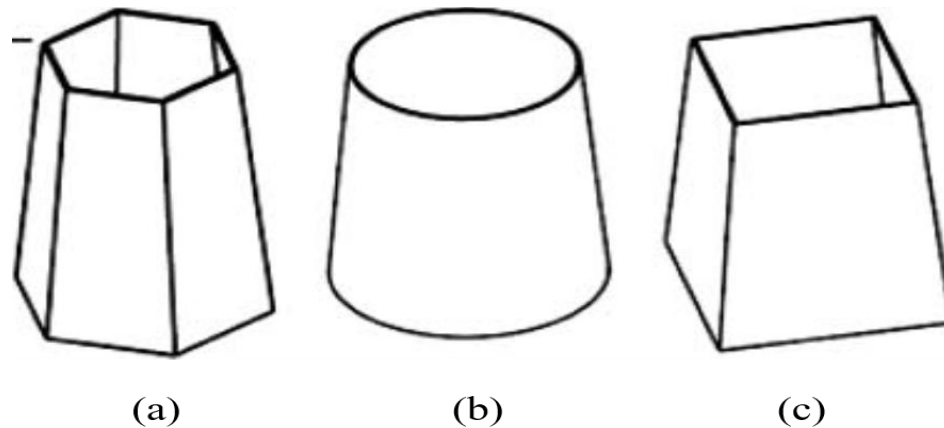


Figure 2-15: Tapered tubes of different cross sections: (a) hexagonal; (b) circular; (c) square [88]

2.5.8 Tubes of Patterned Surfaces

Tubes with patterned surfaces have been the focus of many researchers recently. This is due to the ability of patterned surfaces of lowering the crushing forces, and offering smooth and controllable energy absorption. The patterned surfaces studied in the literature can be divided into surface holes and cutouts, and corrugations and grooves. Introducing surface patterns to the thin-walled structures was because of their role as deformation triggers that allow smooth crushing of the structure, as they work as stress concentration points. The category of windowed tubes or tubular structures with cutouts was studied extensively in the literature. Tubular structures with holes surface patterns (Figure 2-16) work as deformation triggers that allows for smooth deformation and high specific energy

absorption because of the material removal involved in cutting the surface of the structure. Song et al. [17] studied the effect of window-like wall holes' surface patterns (Figure 2-16a). It was found through experimental tests that the window-like holes reduce the initial peak crushing force and increase the energy absorption relative to a conventional tubular structure (with no patterns). Furthermore, Nikkiah et al. [18] studied the effect of various shapes of holes' patterns on the energy absorption response of thin-walled structures under different impact angles. Their results have shown that surface holes reduce the initial crushing force, and that square and rectangular holes patterns result in better crushing performance compared to a conventional tube.

Tubes of corrugated and grooved surfaces was another significant studied category of patterned tubular structures. Wu et al. [23] investigated the performance of straight tubes with sinusoidal corrugated patterns (Figure 2-16b) and found that corrugation increases the undulation load carrying (ULC) capacity and reduce the initial peak force significantly. Furthermore, it was found that corrugated tubes offer around 47-84% reduction in the initial peak force compared to a conventional straight tube. Additionally, Liu et al. [24] studied structures of similar corrugation patterns and found that such patterns enhance specific energy absorption and crushing force efficiency. High crushing force efficiency was also reported by Kılıçaslan [25] who tested circular tubular structures of similar sinusoidal patterns. Moreover, Eyvazian et al. [91] also conducted an experimental study on corrugated tubular structures and found that corrugation reduces the fluctuations in dynamic forces. Finally, external patterns of press-fitted rings on the structure surface which were studied by Isaac et al. [22] revealed that structures with these patterns have

higher energy absorption than regular tubes. Other patterns studied by researchers included buckling triggers patterns [92] which were found to increase the crushing force efficiency. Moreover, structures with pre-folded origami patterns which were explored by Kai et al. [93] who found that these patterns decrease the initial peak force and increase the specific energy absorption.

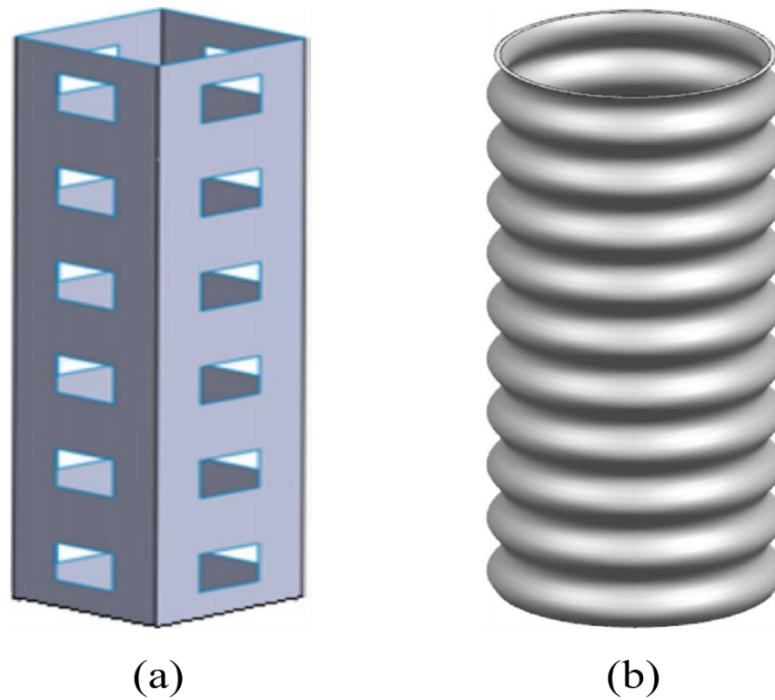


Figure 2-16: Tubular structures of patterned surfaces: (a) windowed tube [17]; (b) corrugated tube [23]

2.6 Analysis of Thin-Walled Energy Absorbers

Many methods have been used to analyze the behavior of thin-walled energy absorbers. Beside experimental analysis, a lot of analytical and numerical methods have been used to study the behavior of thin-walled energy absorbers under impact. The finite element analysis is one of the most used numerical methods in analyzing the crushing response of energy absorbers. The finite element methods have been adopted and used in this study, and therefore the finite element modelling and analysis will be discussed in turn in the following sections.

2.6.1 Finite Element Modelling of Thin-Walled Structures

The Finite Element Method (FEM) is a powerful computational mechanics method that can solve different structural analysis problems. The FE codes, specifically the nonlinear codes, can solve the most complex crash and plastic deformation problems and provide information on the deformation behavior that otherwise is not available using other methods. With the availability of supercomputers, FEM provides a design platform for manufacturers and scientists that allows for iterative designs and conducting parametric studies without wasting money or time. There are a lot of finite element software that can be used to analyze the behavior of thin-walled energy absorber under dynamic impacts such as LS-DYNA, PAM-CRASH, ANSYS, and ABAQUS. In this thesis, the non-linear FE code ABAQUS (version 6.14) has been used to conduct the dynamic simulations of the proposed thin-walled structure and analyze its crushing behavior.

2.6.2 Use of FEM in the Literature

FEM has been used extensively in the literature due to its ability of providing detailed insights on the crushing behavior of energy absorbers. Complex deformation modes and crushing behavior which cannot be analyzed using empirical and theoretical models can be easily predicted using FEM. If validated correctly, FE models provide a feasible analysis of energy absorbers under various impact loads that is accurate and very close to the actual physical behavior. The validation process generally requires experimental data or existing previous theoretical or numerical models that have been established in the literature.

A lot of work on various types of energy absorbers used FE to model the absorbers and analyze their response numerically under different loading conditions. Figure 2-17 shows the numerical models of different thin-walled structures under impact loads and their experimental equivalent [18, 71, 94, 95]. It is evident from the figure that the collapse modes predicted by the FE numerical model are accurate and close to the experimental results. Zhang et al. [96] conducted a study on square tubes of different thickness configurations where finite element method was incorporated to understand the crushing response of square tubes using LS-DYNA. A comparison between the numerical and experimental tests data was conducted, in which the initial peak force, energy absorption and force-displacement profile predicted by the FE model were accurate as shown in Figure 2-18. Tapered tubes have been investigated using solely numerical modelling. Guler et al. [88] have used the explicit finite element code LS-DYNA to study the effect of different geometrical parameters on the behavior of tapered circular tubes under axial impact.

Similarly, Acar et al. [30] have conducted multi-objective optimization study on circular tapered tubes with axisymmetric indentations using the finite element software ANAS. Tubular structures of corrugated surfaces have also been studied using finite element methods. Wu et al. [23] analyzed the crashworthiness behavior and conducted a multi-objective optimization study on sinusoidal corrugated tubes. Furthermore, Kılıçaslan [25] have studied the crushing behavior of foam-filled corrugated tubes numerically using the FE software LS-DYNA.

The studies above show that FE modelling can be used to predict the crushing response and collapse behavior of thin-walled energy absorbers accurately. Therefore, FE modelling is an excellent method to analyze and study the behavior of energy absorbing structures while avoiding the material cost and time involved in experimental testing. The nonlinear explicit FE code ABAQUS was heavily used in this study. The developed FE model used in the study was validated experimentally to assure the accuracy of the obtained results.

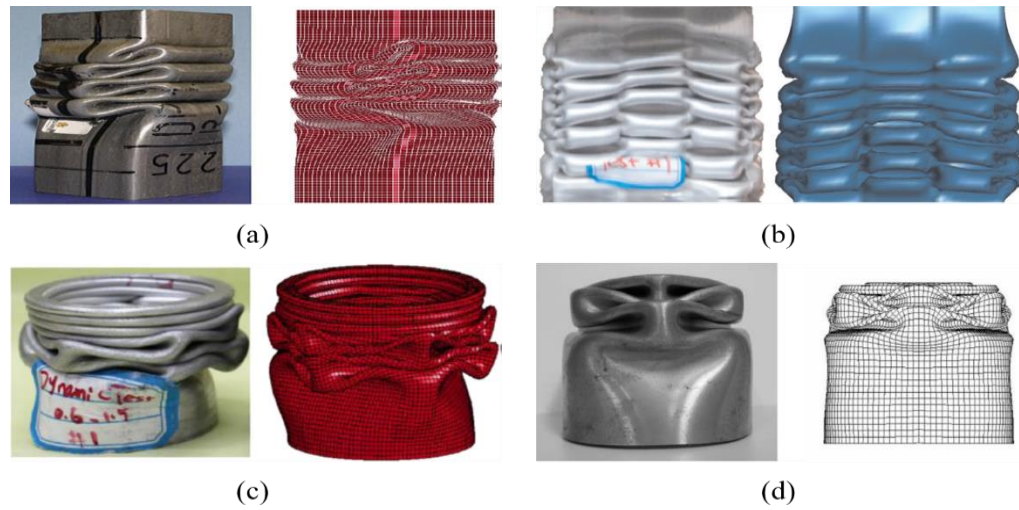


Figure 2-17: FE models of different thin-walled energy absorbers: (a) square tube [94]; (b) multi-cell square tube [71]; (c) circular tube [18]; (d) tapered circular tube [95]: experimental results (left), and numerical simulations (right)

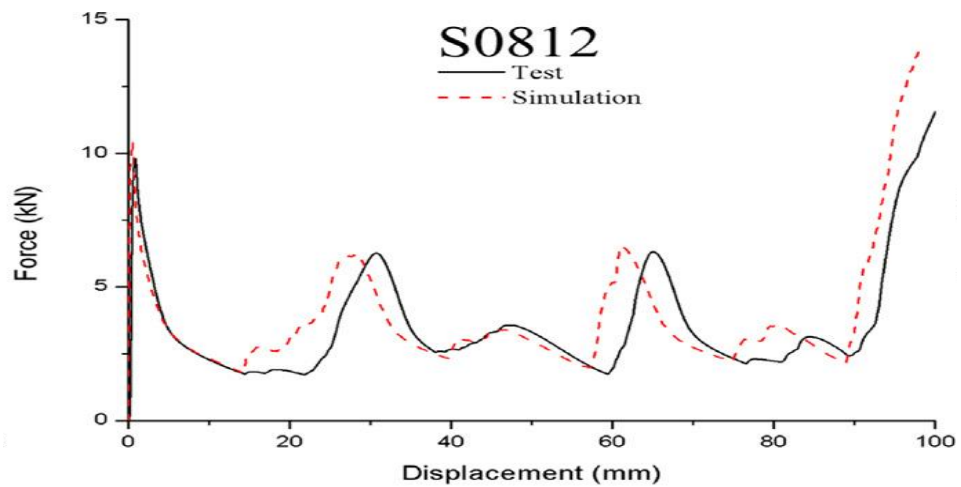


Figure 2-18: Experimental and numerical force-displacement curves of a square tube [96]

2.7 Summary of Literature Review

This chapter provided a comprehensive literature review on the most relevant topics to this thesis. The chapter specifically discussed the crashworthiness and impact of structures, energy absorption by structures, thin-walled energy absorbers, analysis of thin-walled energy absorbers, and the use of finite element methods in modelling energy absorbers and solving energy absorption and crushing problems.

2.7.1 Main Findings from the Surveyed Literature

The literature has revealed that there is an abundance of research work done on the crushing response and energy absorption of thin-walled energy absorbers of different geometrical cross-sections and modifications. A lot of these studies involved investigating the behavior of these structures under different loading conditions, and many have incorporated the use of FEA in carrying out these studies. Numerous studies have mainly investigated the crushing response and energy absorption performance of straight corrugated tubes while limited work has been conducted on corrugated tapered tubes, despite their excellent performance under axial and oblique loading conditions as highlighted in this chapter. Prominently, tapered circular tubes have lower chances of developing global Euler buckling under both axial and oblique loading conditions, which is not the case for straight circular tubes. Henceforth, for energy absorption applications where an energy absorber is exposed to all kinds of loading conditions, a tapered circular tube might be preferable.

2.7.2 Research Gaps and Thesis Aims

To the extent of the author's knowledge, the research work conducted on corrugated tapered circular tubes is rather limited. No research work that studies the crushing response and energy absorption performance of corrugated tapered tubes under axial and oblique impacts has yet been published. This raises the question of what will the energy absorption performance, crushing response and collapse behavior of corrugated tapered tubes under axial and oblique impacts be? Moreover, how will the performance of corrugated tapered tubes as energy absorbers under axial and oblique impacts compare to the performance of conventional tapered and straight tubes? This thesis aims to answer these significant questions by studying the effect of geometrical factors and loading angles on the crushing response of corrugated tapered tubes under axial and oblique impacts. Since studying the effect of geometrical factors and loading angles requires a huge number of crushing experiments, it was beneficial to study the collapse, crushing and energy absorption behavior of corrugated tapered tubes using FEA, which is a useful numerical tool that has been used broadly in the literature. Few experiments tests were conducted for validation purposes.

CHAPTER 3: METHODOLOGY

3.1 Introduction

This chapter explains and describes the methods used to carry out this study. The crushing tests conducted in this thesis were implemented using finite element methods. First, an FE model was developed to simulate the crushing of corrugated tapered tubes. After the FE model was developed, two experimental crushing tests were conducted to validate the FE model against experimental data. The geometry of the proposed corrugated tapered tubular structures was varied, and a simple design of experiment method was followed to determine the number of crushing tests needed for axial and oblique impact testing. The following sections explain the FE modeling, the elements of the FE model, and the validation of the FE model.

3.2 Development of The FE Model for Corrugated Tapered Tubes

3.2.1 FEM tool

The finite element method (FEM) is a numerical method that is used widely in engineering applications. The idea of finite element methods is dividing (discretizing) physical systems or problems into smaller parts/units called elements [97]. Instead of solving the complicated system, these finite elements are solved individually using simpler equations. The combined solution of these equations provides the solution for the overall system. To elaborate how FE solves a crushing problem, the time-dependent deformation of the continuum point can be obtained using the following Cauchy momentum equation:

$$\sigma_{ij} + \rho f_i = \rho \ddot{x}_i \quad (3-1)$$

where σ_{ij} refers to the stress, ρ refers to the density, f_i refers to the body force, and \ddot{x}_i refers

to the body acceleration. The principle of virtual work can be found using the divergent theorem, and the previous equation can be written in the following form:

$$\int_V \rho x_i \delta \ddot{x}_i dV + \int_V \sigma_{ij} \delta x_{ij} dV - \int_V \rho f_i \delta x_i dV - \int_{S_2} t_i \delta x_i dS = 0 \quad (3-2)$$

Eq. (3-2) can be represented by the matrix form as follows:

$$\sum_{i=1}^n \left\{ \int_V \rho N^t N a dv + \int_V B^t \sigma dv - \int_V \rho N^t b dv - \int_A N^t F dA + \int_S N^t F_c ds \right\}^i = 0 \quad (3-3)$$

Where n refers to the element number, σ refers to the stress vector, N refers to the interpolation matrix, a refers to the nodal acceleration vector, b refers to the body vector, and F refers to the traction force. Eq. (3-3) can be generalized and rewritten as following:

$$[M] \left[\frac{d^2 u}{dt^2} \right] + [C] \left[\frac{du}{dt} \right] + [K] \{U\} = [F(t)] \quad (3-4)$$

Where M refers to the mass matrix, C refers to the damping matrix, and K refers to the stiffness matrix. The boundary and initial conditions are considered in the beginning, and then the displacement solution is obtained based on these conditions. Consequently, the strains, forces, and energies are computed. Typically, a finite element software is used to solve the aforementioned dynamic equation using implicit methods. Nevertheless, such methods are not suitable for nonlinear cases such as the dynamic crushing, and hence explicit methods are used. Explicit methods depend on dividing the total time into small time units known as steps. The equations under consideration are solved, and the variables of interest are computed at time $t+\Delta t$ given their values at t . In the explicit method of solving, the information of a time step can be computed given the information of the previous time step only. On the other hand, in the implicit method of solving, evaluating the information at a time step depends on the previous step and the current one, which complicates solving the dynamic equations.

In this thesis, ABAQUS finite element solver with explicit time integration was used to develop and solve the FE model for the crushing of corrugated tapered tubes. FE models consist of the geometry of the system of the problem of concern, the mesh and element type of this geometry, the boundary conditions and contact algorithms related to the system, and the material model applied to the system. The accuracy of the solutions provided by FE models depends mainly on the previous aspects which are explained in detail in the following sections.

3.2.2 Geometry & Design of Experiment

The configurations that define the corrugated tapered tube (CTT) consist of two main features: tube wall corrugation and tube wall inclination (tapered tube) as shown in Figure 3-1. The corrugation of the tube is measured by two parameters: the corrugation amplitude (A) and wavelength (W). The inclination of the tube wall is measured by the tapered angle (Θ). Other geometric factors include the tube's total length (L), wall thickness (t), and top diameter (D). The lower diameter of the tube changes according to the tapered angle and top diameter. For the axial impact testing, those above six geometric parameters are assigned with two values (levels) as shown in Table 3-1. The 1st and 2nd levels represent a random minimum and maximum values of each geometric factor, respectively. This was done to investigate the effect of the geometric factors on the performance of the proposed CTT. Using a simple factorial experiment design, we obtain a total of 64 CTT profiles for axial crushing simulations:

$$\text{Number of simulations} = \text{Number of levels}^{\text{number of factors}} \quad (3-5)$$

For oblique impact loading conditions, the tube length (L) and top diameter (D) will have fixed values of 150 mm and 50 mm, respectively. The rest of the geometric parameters described in the previous section will have two assigned values as shown in Table 3-1. Using the simple factorial design of experiment method in Eq. (3-5), we obtain a total of 16 corrugated tubular structure profiles. Each profile is tested under seven different impact angles: 0° (Axial impact), 10° , 15° , 20° , 25° , 30° and 40° , which leads to a total of 112 impact experiments. The large number of impact experiments makes using finite element analysis essential to save material cost and time.

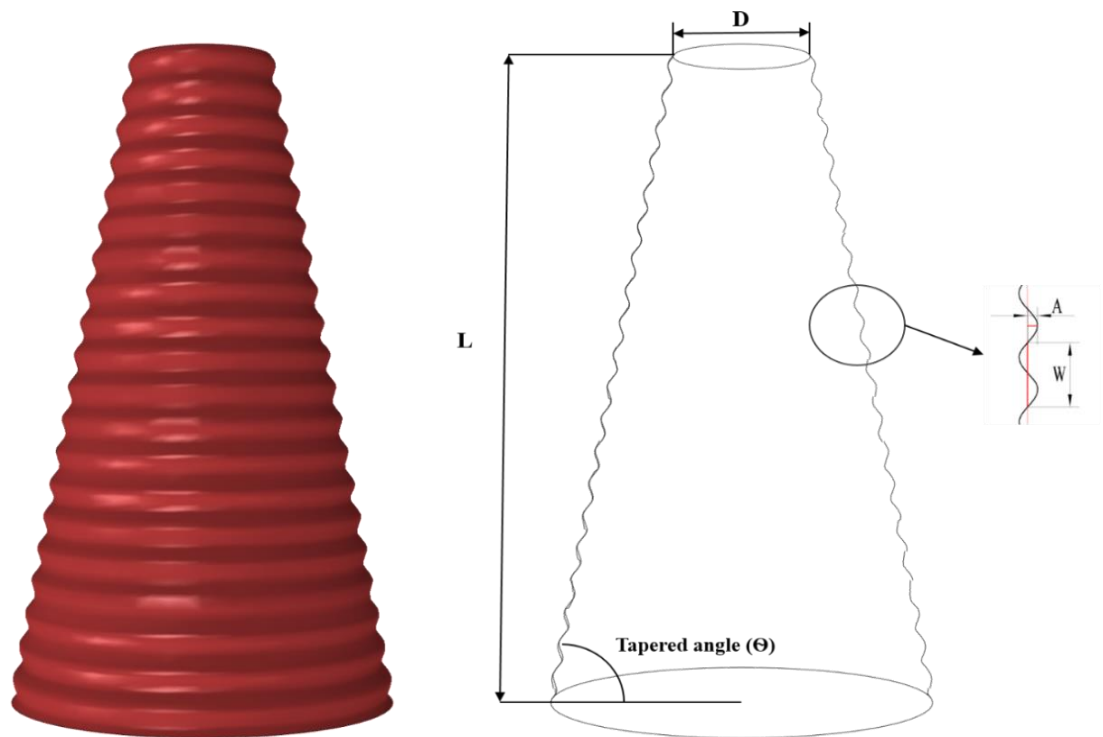


Figure 3-1: Corrugated tapered tube profile and parameters

Table 3-1: Corrugated tapered tube geometric factors and values for axial and oblique impact conditions

Geometric factor	Axial Impact		Oblique Impact	
	1st level	2nd level	1st level	2nd level
Amplitude (A)	1 mm	2 mm	1 mm	2 mm
Wavelength (W)	10 mm	20 mm	10 mm	20 mm
Tapered angle	80°	85°	80°	85°
Thickness (t)	1 mm	2 mm	1 mm	2 mm
Length (L)	150 mm	200 mm	150 mm	150 mm
Top diameter (D)	40 mm	50 mm	50 mm	50 mm

3.2.3 Element Type Selection

The element type has a significant effect on the accuracy of the FE model. ABAQUS provides a vast library of elements for different geometries and different types of applications. The element type is usually defined by five different characteristics: family, number of nodes, degrees of freedom, formulation, and integration. Each element family is tied directly to the type of the structure of the problem under consideration (Figure 3-2). For example, for a structural analysis problem of a solid part, the family of solid/continuum elements can be used. In this thesis, the collapse behavior and energy absorption of thin-walled corrugated tapered tubes under axial and oblique impact are investigated. Hence, the structure under investigation has low thickness value compared to the other global dimensions such as the length and the diameter. Therefore, the shell element family is used for this application. The shell element family in ABAQUS consists of 3 groups: thin-elements group, thick-elements group, and general-purpose elements group. Generally, general-purpose elements can be used for most types of problems, while thick-elements group can be used for complex contact problems. Hence, the general-

purpose elements group was used in this thesis.

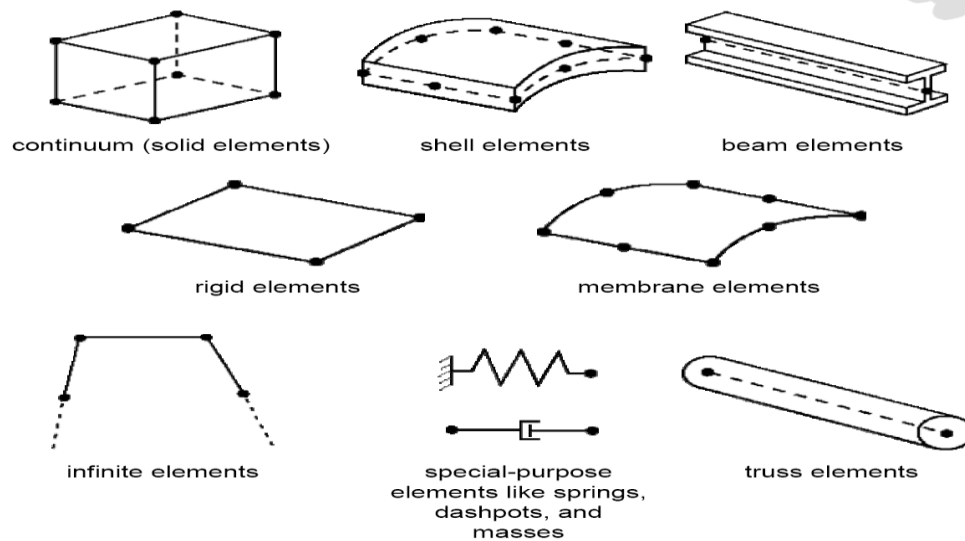
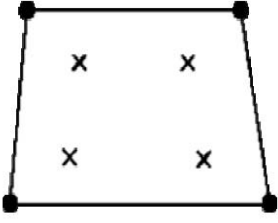
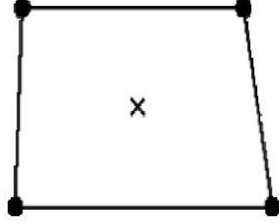
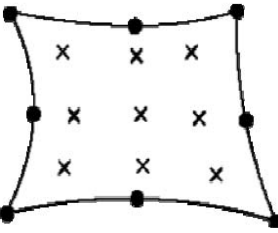
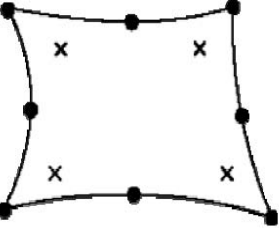


Figure 3-2: Elements families in ABAQUS [98]

Each element has a different number of nodes that determines how the nodal degrees of freedom will be interpolated across the element's domain. In ABAQUS, the elements can have 1st and 2nd order interpolation, or in other words they can be linear or quadratic elements, respectively. Although higher interpolation order (quadratic elements) will provide a better picture of the behavior of the element in some applications, however, it will also increase the solving time and decrease the computation efficiency [98]. On the other hand, linear elements can be used for a wide range of applications and are very cost effective. As for the degrees of freedom, an element of six degrees of freedom would be sufficient for the impact problem in this thesis.

Another characteristic that affects the computational efficiency is the number of integration points. The integration points are the sampling points where the element's stiffness and mass are calculated. In ABAQUS, elements can have both full and reduced integration. Table 3-2 shows linear and quadratic elements of full and reduced integration. The fully integrated elements are recommended for excellent solution accuracy; however, they increase the computation time [98]. In addition, linear fully integrated elements are prone to shear locking, which is a non-physical deformation mode that occurs under bending [99]. Shear locking happens because the stiffness of the element is overcalculated, which makes the element too stiff to bend. Under bending loads, the element should distort in a way similar to the one depicted in Figure 3-3. However, when fully integrated elements are used, the stiffness of the element is overpredicted, and the edges of the element become too stiff to curve. As a result, the distortion of the element will look like the one shown in Figure 3-4.

Table 3-2: Linear and quadratic elements of full and reduced integration [98]

	Full Integration	Reduced Integration
Linear Element (1 st Order Interpolation)		
Quadratic Element (2 nd Order Interpolation)		

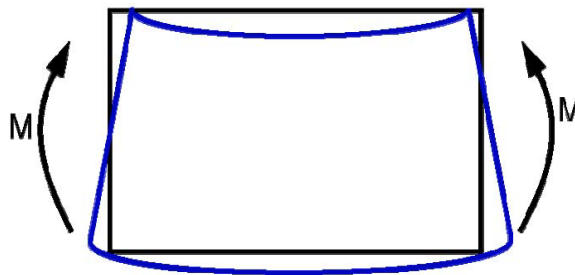


Figure 3-3: Deformation of material under pure bending [98]

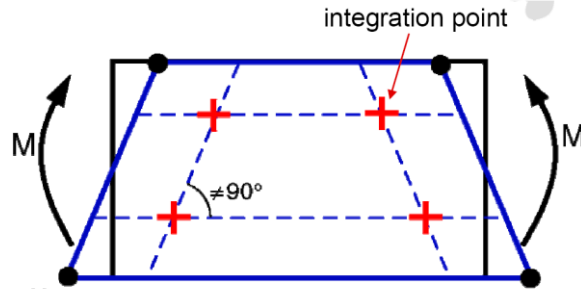


Figure 3-4: Deformation of linear fully integrated element under pure bending (Shear locking) [98]

To overcome the issue of shear locking, elements of reduced integration can be used. However, these elements are prone to another problem known as hour-glassing. Hour-glassing is another non-physical mode that occurs to linear elements of reduced integration under bending loads [99]. Because of the lower number of integration sampling points, the stiffness of the element is underpredicted, and therefore the element becomes very flexible. This leads the element to distort similar to the distortion depicted in Figure 3-5, which makes the obtained results unusable. To overcome the problems of hour-glassing, ABAQUS has different algorithms that control the hour-glassing and enhance the stiffness of the element. This makes the elements of reduced integration preferable since the hour-glassing problem can be avoided by the algorithms provided by the software, and because they are efficient in terms of computation cost.

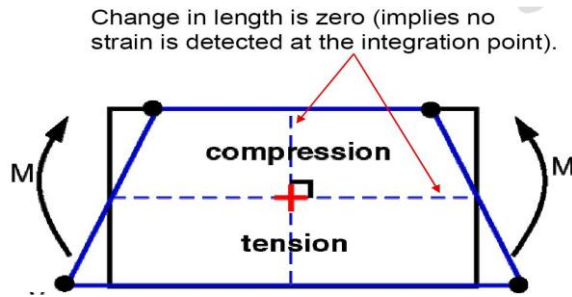


Figure 3-5: Deformation of linear element of reduced integration under pure bending (Hour-glassing) [98]

Based on the previous discussion, a linear shell element of six degrees of freedom and reduced integration can be used for the impact problem in this thesis. Therefore, the S4R 4-node quadrilateral shell element with 5 section points (Figure 3-6) was selected as the element to model the proposed corrugated tapered tube structure under investigation, due to its robustness, computation cost-effectiveness, and suitability for the thesis's impact application and most nonlinear design problems.

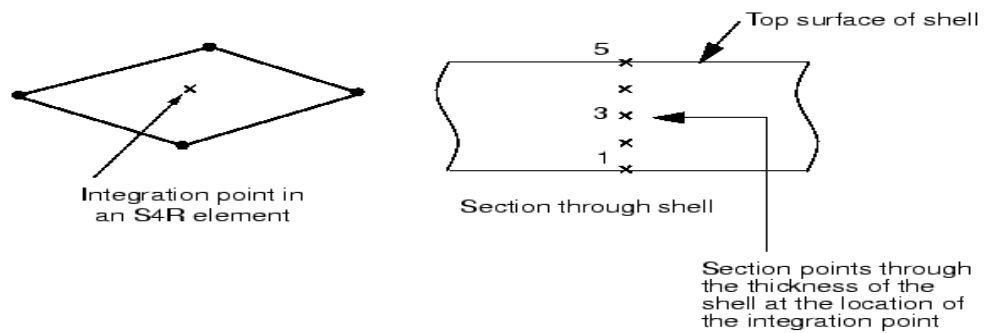


Figure 3-6: S4R linear 4-node shell element with reduced integration [98]

3.2.4 Mesh Size Optimization

Similar to the element type, the mesh size also affects the accuracy of the FE model results. When the mesh size is fine (small), the discretization of the system is larger, and hence the FE model solution is more accurate as it represents the physical system accurately. However, this leads to an increase in the mesh density and consequently the computation time which defies the purpose of using finite elements in the first place. In general, mesh convergence studies are conducted to select mesh size that provides acceptable accuracy and efficient computation time. The idea of mesh convergence study is to solve the FE model using different mesh sizes and compare the results of concern between the selected sizes. When the error in the results' accuracy between two specific sizes start to reduce insignificantly, the next large mesh size is selected as it reduces computational time and assures accurate results.

In this thesis, a mesh convergence study was performed to select the optimum mesh size for axial and oblique impact conditions. For the axial impact, a CTT tube of 10-mm wavelength and 2-mm amplitude was simulated using different mesh sizes. It was found that a mesh size of 5 mm does not have a significant variation in terms of peak force or energy absorption (Figure 3-7) when compared to a mesh size of 2-mm. Hence, a mesh size of 5-mm was selected for axial impact tests. For the oblique impact, the same CTT tube was used for the convergence analysis, however, under an impact angle of 40° . This was done because the oblique impact will cause extreme element deformation, and hence a smaller element size might be needed for testing corrugated tapered tubular structure under oblique impact. It was found from the analysis that an element size of 2-mm does

not have a significant variation in terms of initial peak force or energy absorption (Figure 3-8) when compared to a smaller mesh size of 0.5-mm, and therefore a mesh size of 2-mm has been selected for CTTs tested under oblique loading conditions.

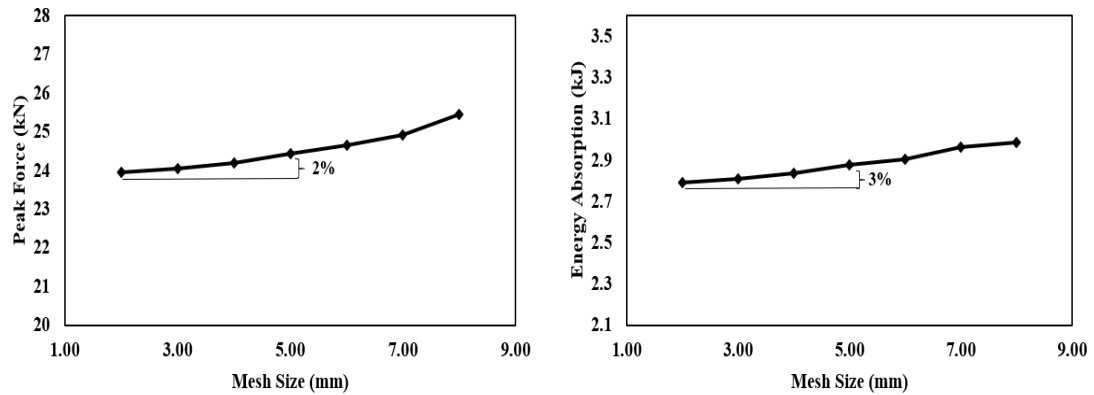


Figure 3-7: Mesh sensitivity analysis under axial impact

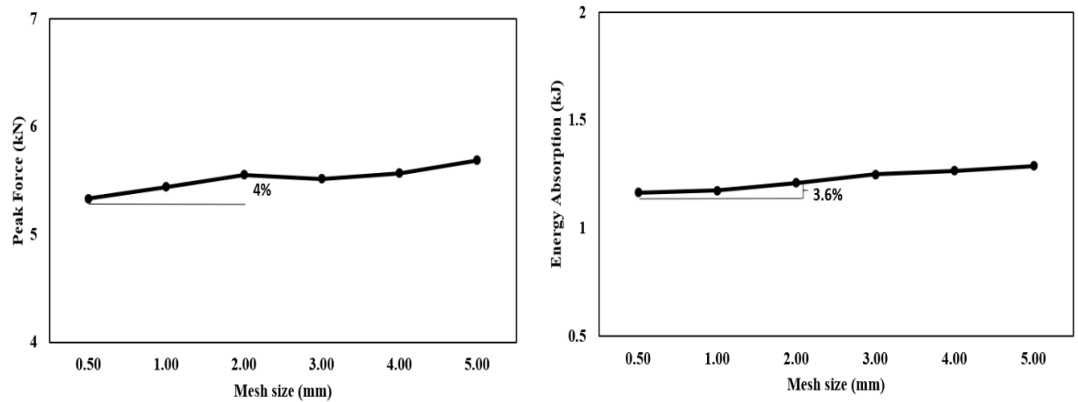


Figure 3-8: Mesh sensitivity analysis under oblique impact (40°)

3.2.5 Boundary Conditions

In the crash simulation setup, the CTT structure is placed on a fixed plate where it gets impacted by a top plate (striker) from the other free end. The fixed plate and the impact mass were modeled as rigid surfaces. The striker was assigned with a mass point of 275 kg. The mass was selected based on the fact that an energy absorber is assumed to absorb about only 25% of the kinetic energy of an average sedan vehicle that weighs 1100 kg [100]. The striker's impact velocity was modeled as a predefined velocity field of 15 m/s as shown in Figure 3-9. The selected striker's speed represents the speed used by the National Highway Traffic Safety Administration (NHTSA) for crash tests on automobile vehicle [101]. The striker's motion was limited to translational motion only with no rotation. The chosen contact algorithm was general of 0.2 friction coefficient to define the contact between the tube, the striker and the bottom fixed rigid plate. The general contact algorithm is essential to prevent the interpenetration of the tube's walls under crushing [102].

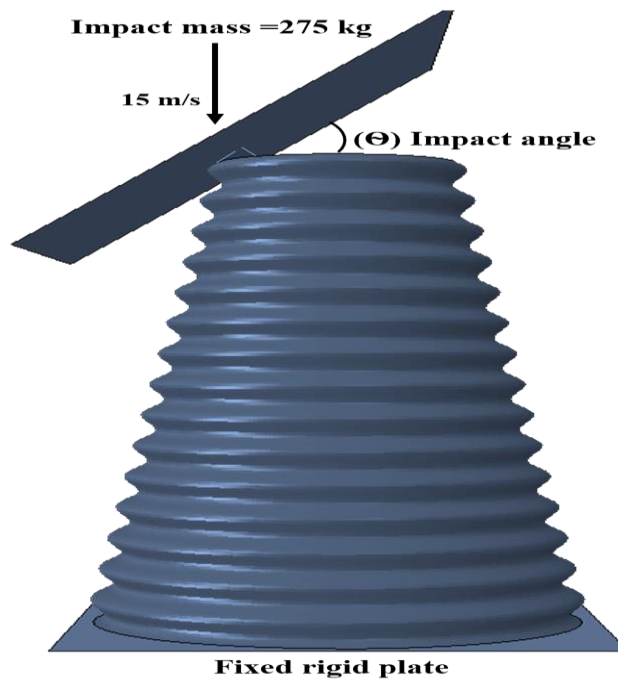


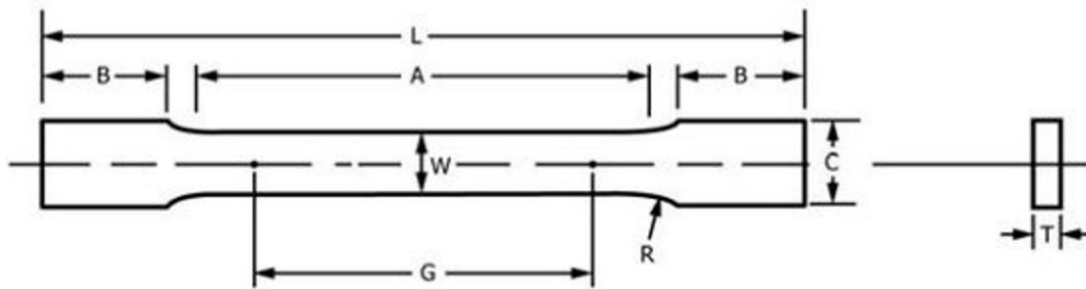
Figure 3-9: Crash simulation setup and boundary conditions

3.2.6 Material Properties

The material used for the CTT structures proposed in this thesis is AA6060 aluminum alloy. Aluminum was selected for the proposed structure due to its light weight compared to other metals such as steels, and low cost compared to composites. The material properties were obtained by performing a standard tensile test on three specimens which were cut with the dimensions per ASTM: E8/E8M-11 standard shown in Figure 3-10. The tensile test experiments were conducted using the Instron Testing Machine of 250 kN capacity which is fully computerized with data acquisition system. A summary of the material properties is listed in Table 3-3. The tensile testing machine, the specimen and a representative stress-strain curve are shown in Figure 3-11.

Table 3-3: Material properties of the aluminum alloy AA6060

Density	Young's modulus	Poisson's ratio	Yield stress
2700 kg/m ³	68.21 GPa	0.3	80 MPa



G – Gauge length = 50 mm

W – Width = 12.5 mm

T – Thickness = 12.5 mm

R – Radius of fillet = 12.5 mm

L – Overall length = 200 mm

A – Length of reduced parallel section = 57 mm

B – Length of grip section = 50 mm

C – Width of grip section = 20 mm

Figure 3-10: ASTM E8/8M-11 sheet-type static tensile test specimen's dimensions

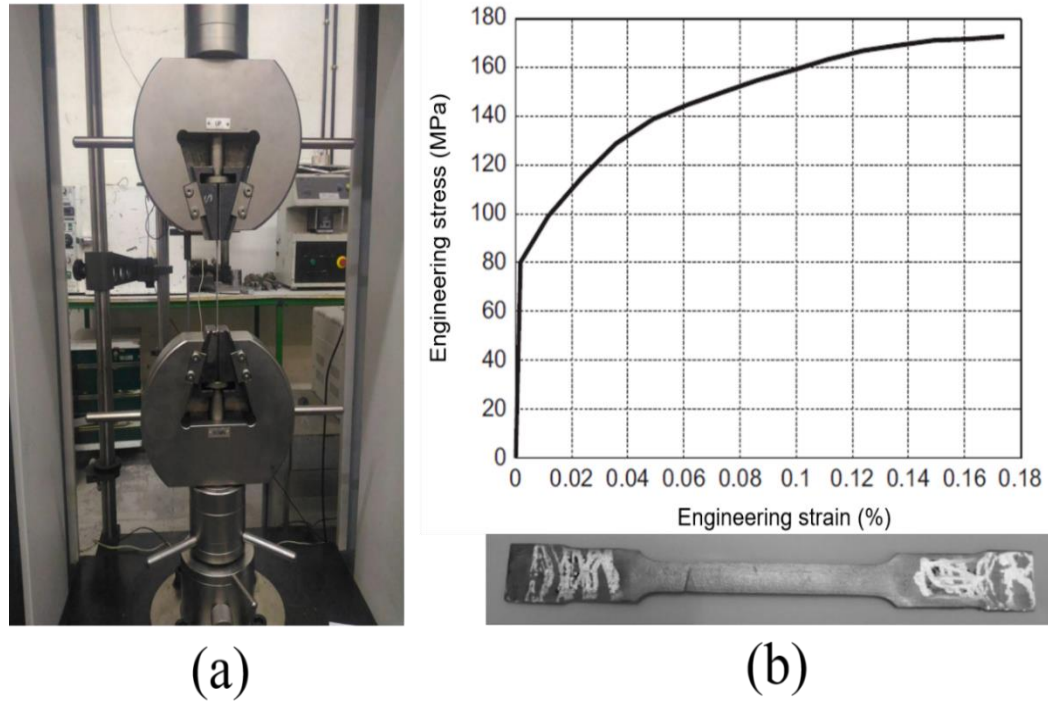


Figure 3-11: Axial tensile test set-up and specimen: (a) Instron Testing Machine of 250 kN capacity; (b) tensile test specimen and representative engineering stress-strain curve

3.2.7 Material Model

In the FE model, the structure material behavior was characterized by the Johnson-Cook isotropic constitutive model, which is extensively used for applications where high strain rates exist. The Johnson-Cook model is given in Eq. (3-6) [44]:

$$\sigma = [A + B\varepsilon^n] \left[1 + C \ln \left(\frac{\dot{\varepsilon}}{\dot{\varepsilon}_0} \right) \right] \left[1 - \left(\frac{T - T_{room}}{T_{melt} - T_{room}} \right)^m \right] \quad (3-6)$$

where σ is the material stress, ε is the plastic strain, $\dot{\varepsilon}$ is the strain rate, and $\dot{\varepsilon}_0$ is the reference strain rate, T is the structure's surface temperature, T_{melt} is the material melting point, and T_{room} is the room temperature. The assumption followed in this study was that

the tube temperature T is equal to the room temperature T_{room} , which means that the third function of Eq. (3-6) will equal 1. Therefore, the temperature will not affect the results of the study. The parameters A , B , C , n , and m , are empirical constants [45], and their values are listed in Table 3-4.

Table 3-4: Johnson-Cook parameter for (AA6060) aluminum alloy

Parameters	Values
A	70.28 MPa
B	302.5 MPa
Strain Power Coefficient, N	0.46
C	0.0001
Temperature Power Coefficient, M	0.7
Reference Strain Rate	1.0 s ⁻¹

3.3 FE Model Validation Against Experimental Testing

The most suitable way to validate the FE model is to conduct dynamic compression tests. However, this was not possible due to the capacity limitation of the dynamic compression machine. Nevertheless, since AA6060 alloy is only slightly sensitive to strain rate [43-45], quasi-static compression tests can be used to validate the FE model accurately. The FE model was validated using a circular straight aluminum tube and a straight corrugated tube under quasi-static axial compression with a constant velocity of 0.5 mm/min. Both tubes had a diameter of 70 mm, length of 80 mm and thickness of 1.65 mm. The corrugation's amplitude and wavelength of the corrugated tube were 3.5 mm and 18 mm, respectively. The quasi-static compression test of the tubes was conducted using the

Instron 8502 hydraulic (250 kN) testing machine.

Quasi-static simulations are solved using ABAQUS implicit/standard code. Although ABAQUS implicit solver is for true static equilibrium problems, however, the implicit solver is not very effective when it comes to high nonlinear static problems such as static compression tests. On the other hand, ABAQUS explicit solver is more efficient for this type of problems in terms of computation cost. When using the explicit solver for quasi-static problems, it is impractical to use the real-time period of the quasi-static test. Instead, the speed of the test needs to be increased artificially. This can be done by a process known as mass scaling. The idea of mass scaling is to artificially increase the density of the material so that the time step increment increases. The explicit solver in ABAQUS solves problems as wave propagation problems. The stable time increment in an explicit solving procedure is the minimum time for a wave (i.e., stress wave) to move across an element, and therefore can be estimated as [98]:

$$\Delta t = \frac{L^e}{C_d} \quad (3-7)$$

Where L^e is the element's length, and C_d is the wave speed. For a linear elastic material, the wave speed can be obtained as follows:

$$C_d = \sqrt{\frac{E}{\rho}} \quad (3-8)$$

Where E is Young's modulus, and ρ is the material's density. From Eq. (3-7) and Eq. (3-8), if the material's density is increased artificially by a factor of f^2 , the speed of the wave will reduce by a factor of f , and the stable time increment increases by a factor of f . Therefore, mass scaling allows for analyzing the quasi-static problem in its natural time

period by reducing the computation time. Therefore, mass scaling was used in the FE model for validation purposes, and both the circular and the corrugated tubes were scaled by a factor of 10^8 to increase the computation efficiency.

Figure 3-12 and Figure 3-13 show the deformation modes obtained from the experimental test and FE model for both the circular and corrugated tubes. From here, it is evident that the FE model was able to capture the collapse modes of the experimental tests. Furthermore, Figure 3-14 and Figure 3-15 depict the force-displacement profiles obtained from the experimental test and the FE model for both tubes. The initial peak force, mean force and energy absorption were calculated for both experimental tests and the FE model, and the error was insignificant as shown in Table 3-5. Therefore, the FE model has an acceptable accuracy and can be used to predict the crushing response of the proposed corrugated tapered tubes design to reduce cost, time and material wastage.

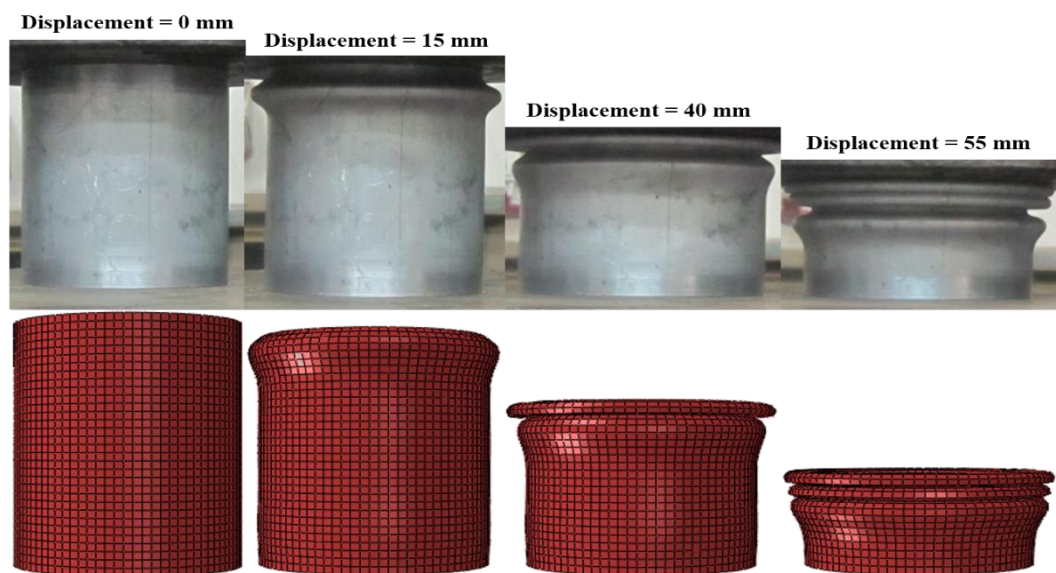


Figure 3-12: Deformation modes of a circular aluminum tube (experimental and FE)

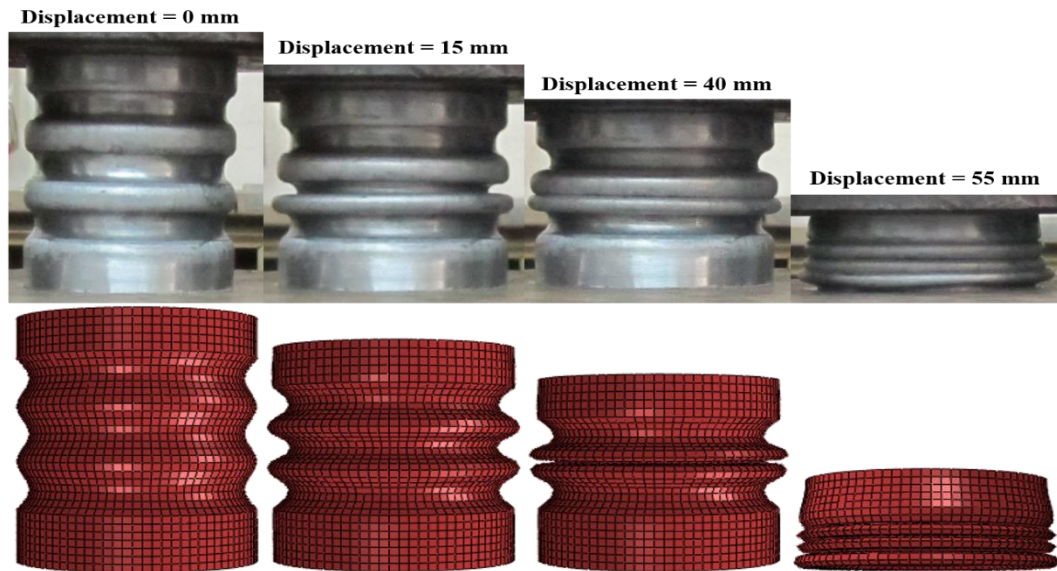


Figure 3-13: Deformation modes for the corrugated aluminum tube (experimental and FE)

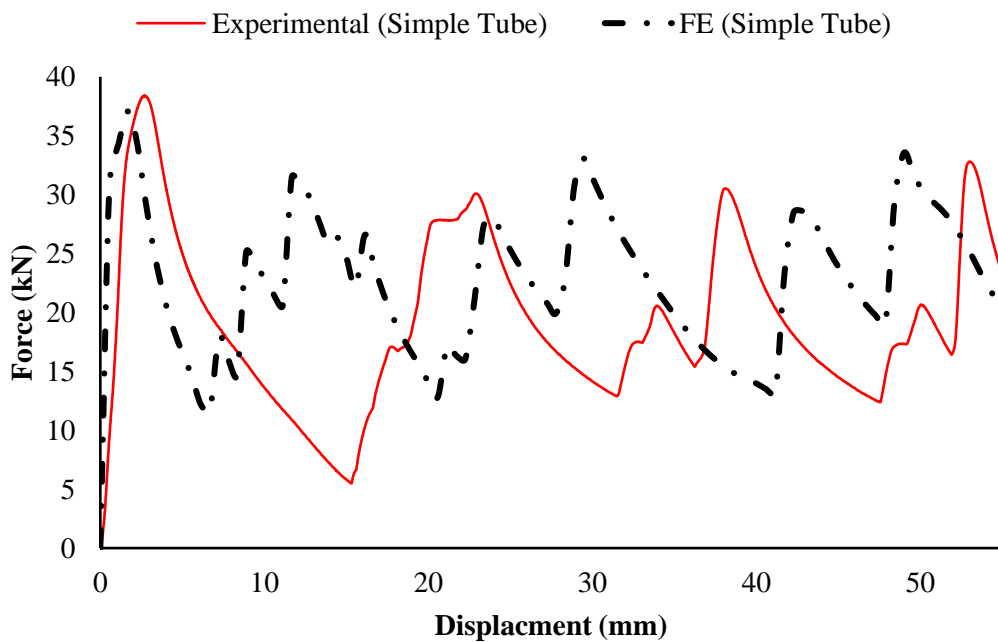


Figure 3-14: Force-displacement profiles for a circular aluminum tube (experimental and FE tests)

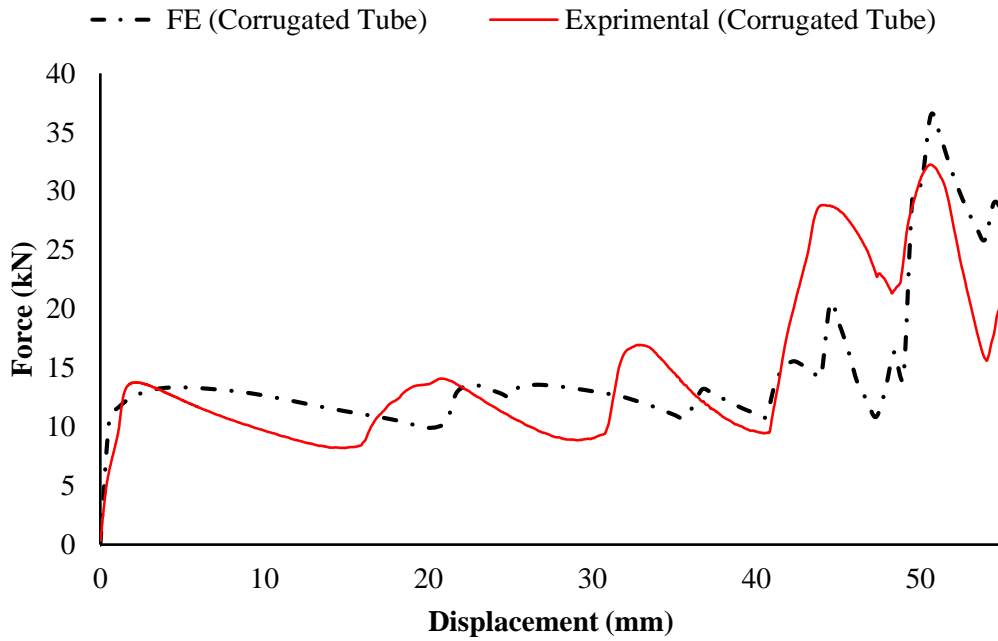


Figure 3-15: Force-displacement profiles for a corrugated aluminum tube (experimental and FE tests)

Table 3-5: Difference in IPF and EA between the original and present study models

	Initial Peak force (kN)	Mean Force (kN)	Energy Absorption (kJ)
Circular Tube			
Experimental	38.40	20.80	1.04
FE	37.06	22.13	0.91
Deviation	-3.5%	+6.4%	-3%
Corrugated Tube			
Experimental	13.61	12.20	0.61
FE	13.34	12.44	0.58
Deviation	-2%	+2%	-5%

3.4 Summary

The developed FE model has been validated using experimental tests on simple and corrugated tubes. The details of the FE model development and all of its aspects have been discussed in this chapter, as well as the model validation against experimental data. The FE model results displayed good agreement with the experimental tests. Therefore, the developed numerical FE model can be used to predict the collapse behavior and energy absorption performance of corrugated tapered tubes under axial and oblique impacts. The model can also be used to understand the effect of the geometric parameters and impact angles on the performance of corrugated tapered tubes.

CHAPTER 4: CORRUGATED TAPERED TUBES UNDER AXIAL LOADING

4.1 Introduction

This chapter discusses the performance of corrugated tapered tubes under axial loading conditions. First, the force-displacement characteristics of corrugated tapered tubes of different amplitudes and wavelengths, and different categories of diameters and lengths under axial impact are discussed. The development of deformation modes and the collapse behavior are then investigated for corrugated tapered tubes of different categories. Finally, the effect of geometrical parameters on the performance indicators is explained, and the most performance-influential geometrical parameters are identified.

4.2 Force-Displacement Characteristics

The performance indicators' values of the tested CTT profiles are summarized and presented in Table 1 to Table 4 in the appendix, for convenience. A detailed explanation on the effect of the design's factors on the performance indicators is presented in the following sections. Typical force-displacement diagrams for CTTs of different diameters and tapered angles combinations are shown in Figure 4-1, while diagrams for CTTs of different lengths and thicknesses combinations are shown in Figure 4-2. The displacement refers to the striker's displacement which is assumed to be in contact with the tube during the crushing process. The diagrams show the force responses for CTTs profiles under axial loading condition. It is evident from the figures that the force-displacement characteristics are rather similar for different combinations of tapered angles and diameters, and different combinations of thicknesses and lengths. Furthermore, it is evident from the figures that

the force-displacement characteristics change mainly with the amplitude. This indicates that the force responses in CTTs are primarily influenced by the tube's corrugation amplitude.

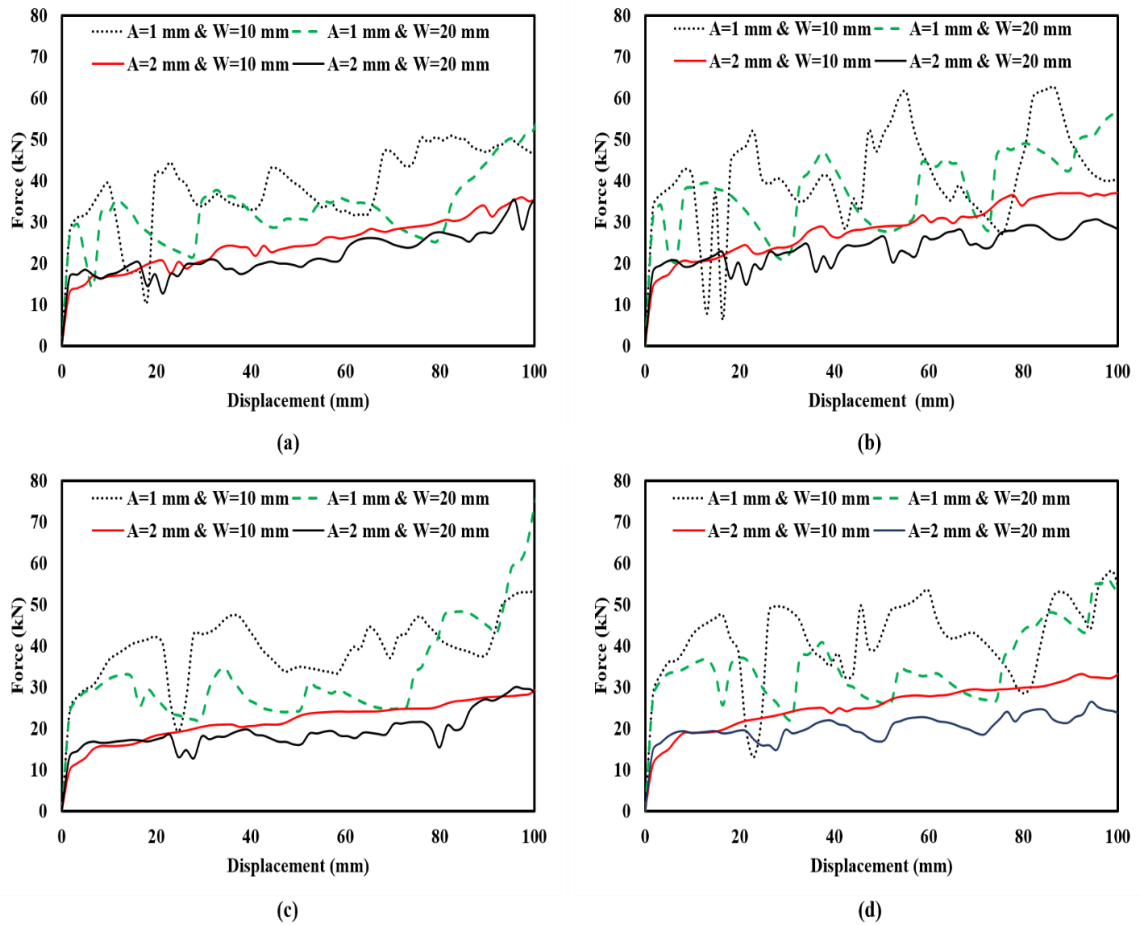


Figure 4-1: Force-displacement diagram of CTTs of $t = 2$ mm & $L = 150$ mm (a) Tapered Angle = 80° & $D = 40$ mm; (b) Tapered Angle = 80° & $D = 50$ mm; (c) Tapered Angle = 85° & $D = 40$ mm; (d) Tapered Angle = 85° & $D = 50$ mm

It is also clear from the diagrams that CTTs with an amplitude of 2 mm have smooth force-displacement curves and lower crushing forces regardless of the wavelength of the profile's corrugation. On the other hand, fluctuations in the force-displacement curves and higher crushing forces are observed for CTTs with an amplitude of 1 mm (regardless of the wavelength). This is because the tubes' corrugation works as collapse triggers that allow for easier fold formation of the tube and promote stable crushing, and a longer corrugation amplitude helps increase this triggering effect.

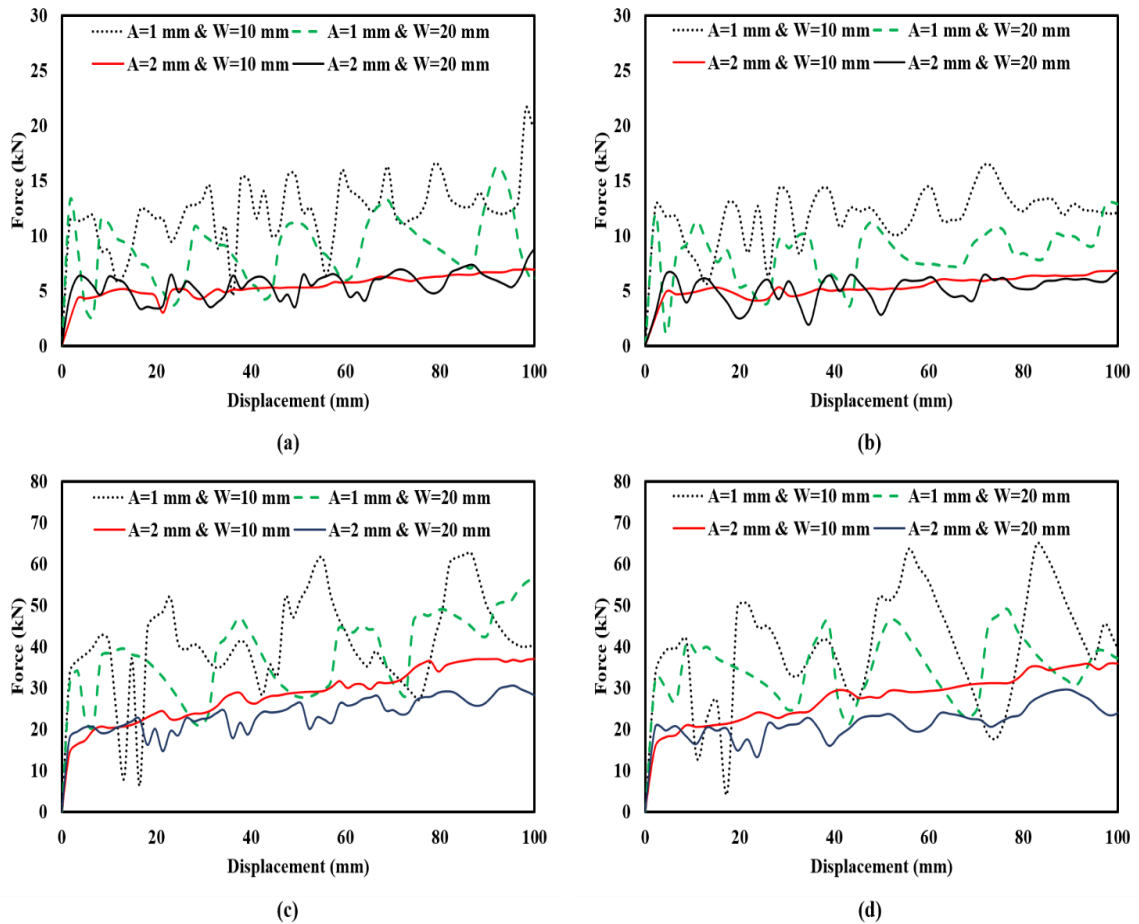


Figure 4-2: Force-displacement diagram of CTTs of Tapered Angle= 80° & $D = 50$ mm (a) $t = 1$ mm & $L = 150$ mm; (b) $t = 1$ mm & $L = 200$ mm; (c) $t = 2$ mm & $L = 150$ mm; (d) $t = 2$ mm & $L = 200$ mm

4.3 Deformation Modes Under Axial Impact

The tested CTTs profiles exhibited three different deformation modes under axial crushing (Figure 4-3). To clearly understand the deformation modes of the tested CTTs, Figure 4-4 to Figure 4-6 show the cross-section views of the crushing stages of CTTs profiles exhibiting the observed deformation modes. Figure 4-4 represents a clear example

of a CTT ($A=2$ mm and $W=10$ mm) exhibiting mode 1. Under crushing, the corrugation gaps start to coalesce from the top (Figure 4-4a to Figure 4-4c) allowing the tube to crush in a stable, progressive manner similar to the concertina instrument. This stable crushing is due to the long corrugation amplitude (2 mm) which enhances the triggering effect of the tube's corrugation allowing it to crush easily. The gaps then keep on coalescing until the tube is crushed completely (Figure 4-4d).

Mode 2 can be seen in the crushing stages of the CTT ($A=1$ mm and $W=20$ mm) presented in Figure 4-5. When the tube starts to deform, an outward fold forms at the amplitude of the first proximal wave as shown in Figure 4-5a. As the crushing progresses, other folds begin to form at similar locations along the tube as shown 4-5b to 4-5c, until the tube is crushed completely (4-5d).

Finally, the development of mode 3 is shown in the crushing stages of the CTT ($A=1$ mm and $W=20$ mm) shown in Figure 4-6. As depicted in the figure, outward folds start to form at the beginning of the crushing process (Figure 4-6a to Figure 4-6b). The folds are then proceeded by irregular ones as shown in Figure 4-6c resulting in an unstable crushing process until the tube is crushed completely (Figure 4-6d). This unstable crushing is due to the low corrugation's amplitude and longer wavelength. As shown in Figure 4-7a, for a fixed amplitude the CTT profile will tend to be less corrugated when the wavelength increases. Hence the triggering effect of the corrugation is lower, disallowing smooth and stable crushing. Similarly, the corrugation will be less evident when the amplitude decreases, which also reduces the triggering effect of corrugation (Figure 4-7b).

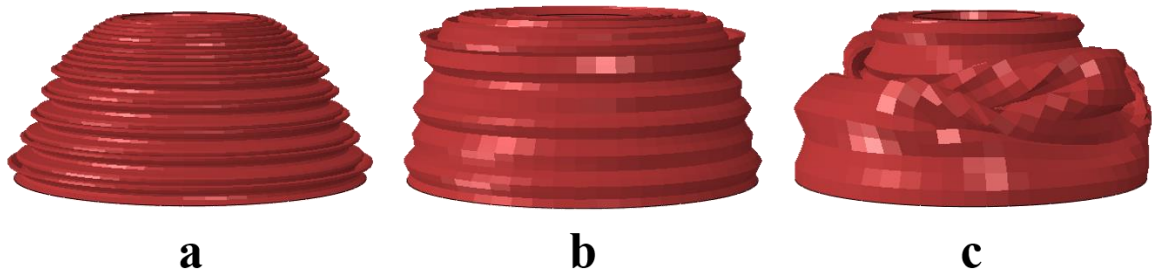


Figure 4-3: CTT exhibited deformation modes, a: mode 1 (Symmetric mode), b: mode 2 (Symmetric mode), c: mode 3 (Non-symmetric mode)

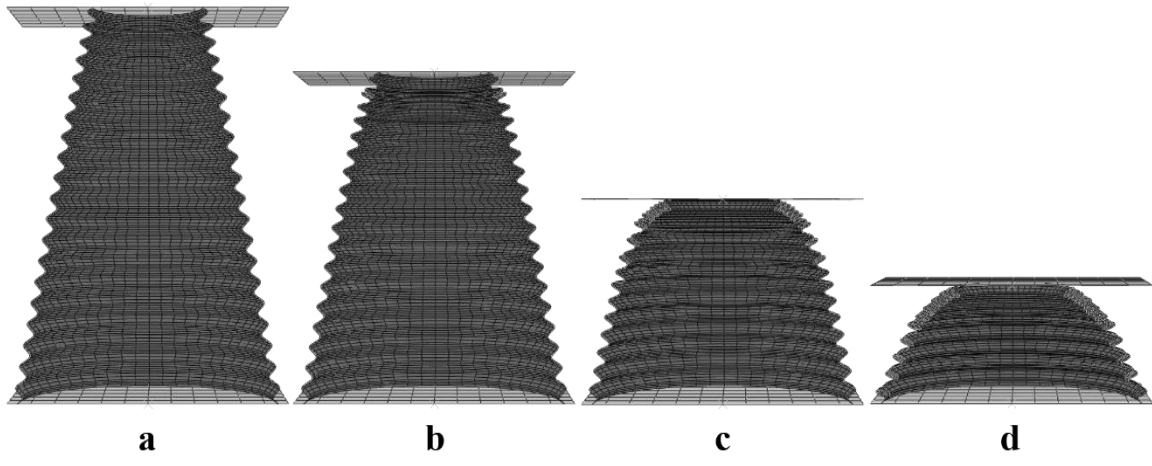


Figure 4-4: Cross-section view of the crushing stages of mode 1 of CTT of $A = 2 \text{ mm}$ and $W = 10 \text{ mm}$ ($L = 200 \text{ mm}$, $D = 50 \text{ mm}$, $t = 2 \text{ mm}$ and Tapered angle = 80°)

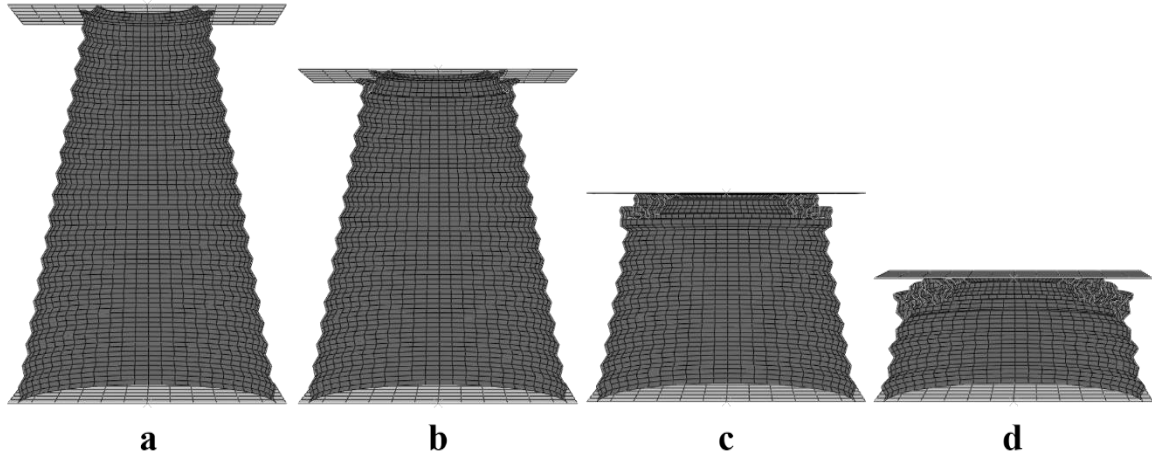


Figure 4-5: Cross-section view of the crushing stages of mode 2 of CTT of $A = 1 \text{ mm}$ and $W = 10 \text{ mm}$ ($L = 200 \text{ mm}$, $D = 50 \text{ mm}$, $t = 2 \text{ mm}$ and Tapered angle = 80°)

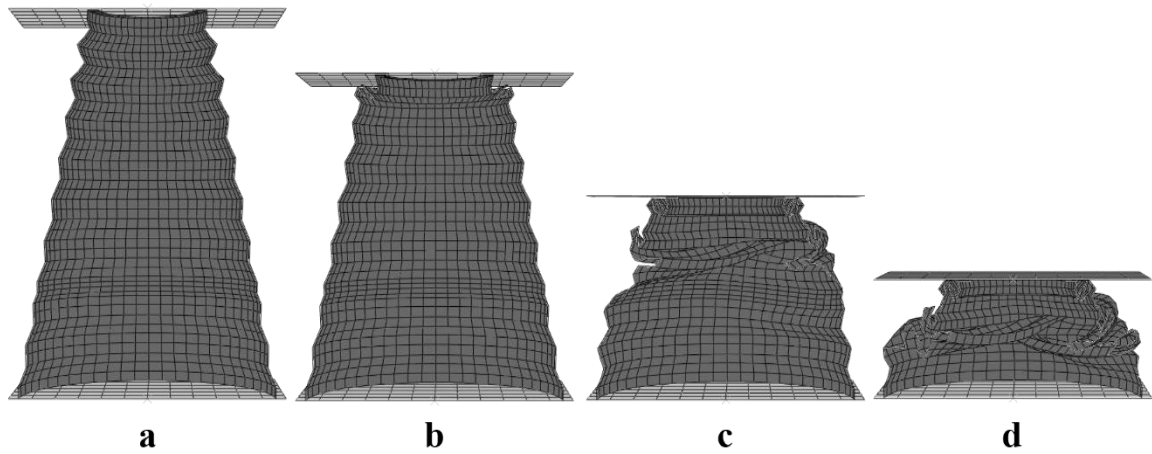


Figure 4-6: Cross-section view of the crushing stages of mode 3 of CTT of $A = 1 \text{ mm}$ and $W = 20 \text{ mm}$ ($L = 200 \text{ mm}$, $D = 50 \text{ mm}$, $t = 2 \text{ mm}$ and Tapered angle = 80°)

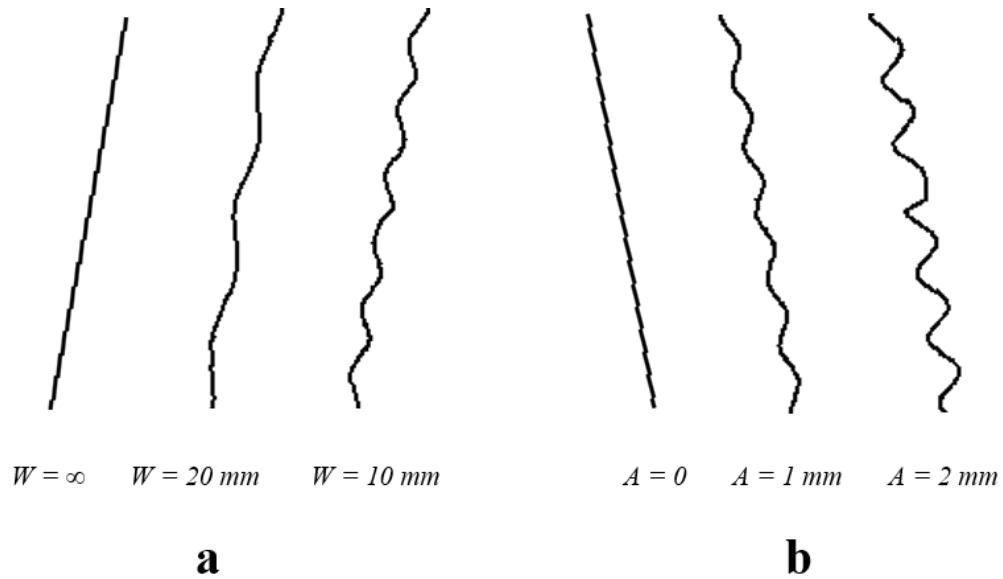


Figure 4-7: The profiles of CTTs for different wavelengths (W) or amplitudes (A) at $W = \infty$ and $A = 0$, (a) $A = 1\text{ mm}$ (b) $W = 10\text{ mm}$

Table 4-1 lists the distribution of the developed deformation modes in CTTs based on the corrugation's amplitudes and wavelengths. It is clear from the figure that mode 1 corresponds to a corrugation's amplitude of 2 mm regardless of the wavelength. However, when the amplitude is 1 mm, mode 2 is exhibited when the wavelength is 10 mm, and mode 3 is exhibited when the wavelength is 20 mm. In general, the deformation modes developed in circular aluminum tubes under axial crushing are influenced by the diameter to thickness, and diameter to length ratios [103]. This was not the case for the selected geometric CTT parameters (length, diameter, tapered angle and thickness), as the developed deformation modes in the tested profiles were mainly influenced by the corrugation's amplitude and wavelength. This is evident from Figure 4-1 and Figure 4-2

which show the force-displacement diagrams for CTTs of different combinations of tapered angles and top diameters (Figure 4-1), and different combinations of thicknesses and lengths (Figure 4-2). From here, the force-displacement characteristics are similar for different geometrical combinations. This is an indication that these geometrical factors do not play a major role in the deformation modes developed in CTTs. However, the force-displacement characteristics are different for different amplitudes and wavelengths, which indicates that the deformation modes are mainly influenced by the wall corrugation.

Table 4-1: Deformation modes distribution for the 64 runs based on the amplitude and the wavelength

Deformation Mode	Amplitude	Wavelength
Mode 1	2 mm	10 mm or 20 mm
Mode 2	1 mm	10 mm
Mode 3	1 mm	20 mm

4.4 Analysis of Performance Indicators under Axial Impact

4.4.1 Influence on Initial Peak Force (IPF)

- **Influence of Amplitude and Wavelength**

Figure 4-8 shows the initial peak force values for CTTs of different amplitudes and wavelengths compared to a conventional circular tapered tube. To study the effect of amplitude and wavelength on IPF, all the tubes depicted in the figure are of the same

thickness, diameter, length, and tapered angle. It is evident from the figure that IPF reduces significantly by adopting the corrugation relative to a conventional tapered tube. For example, IPF of the regular tapered tube is 45 kN, whereas IPF of CTT ($A=2$ mm and $W=20$ mm) reduces to 21 kN (53% reduction). Similar observations were reported for straight corrugated tubes [24, 25, 91] and tapered tubes with surface indentations [30]. This reduction is attributed to the triggering effect of corrugation that reduces the tube's stiffness and promotes crushing.

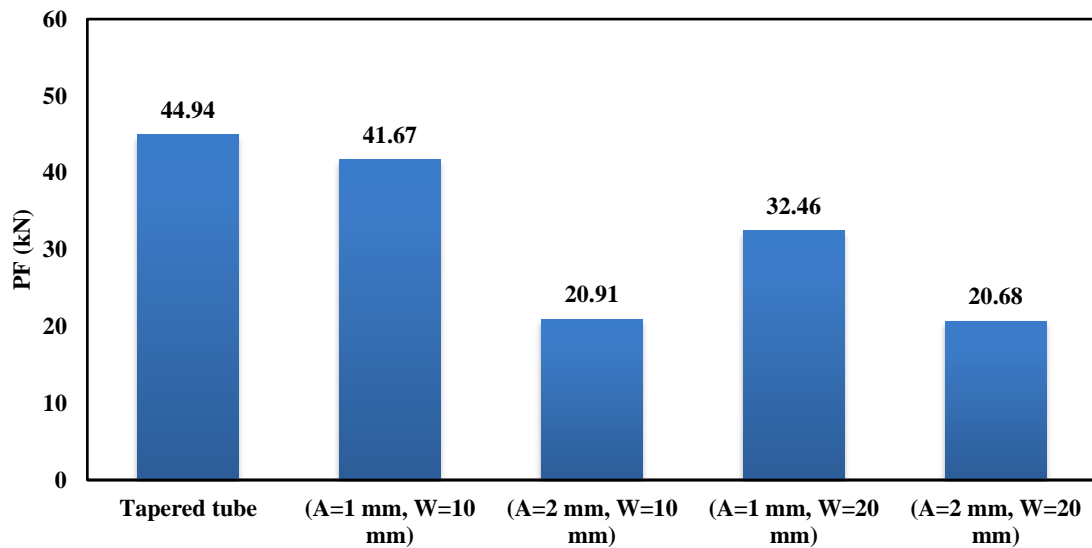


Figure 4-8: IPF values for CTT profiles relative to a conventional tapered tube ($L = 200$ mm, $D = 50$ mm, $t = 2$ mm and Tapered angle = 80°)

Figure 4-9 depicts the average effect of CTT geometrical parameters (from all the 64 simulations) on IPF. It is evident from the figure that the initial peak force in CTT can be considerably reduced by increasing the corrugation's amplitude from 1 mm to 2 mm. Similarly, a minor reduction in IPF can also be obtained by increasing the wavelength to 20 mm. It can be seen at this point that introducing corrugation reduces the initial peak force, specifically for longer amplitudes and longer wavelengths. The same reduction in IPF was also reported by Wu S. et al. [23] when longer corrugation's amplitudes and wavelengths are adopted for straight tubes. This reduction is because of the enhanced corrugation triggering effect due to longer amplitudes and wavelengths which makes the corrugation evident (Refer to Figure 4-7).

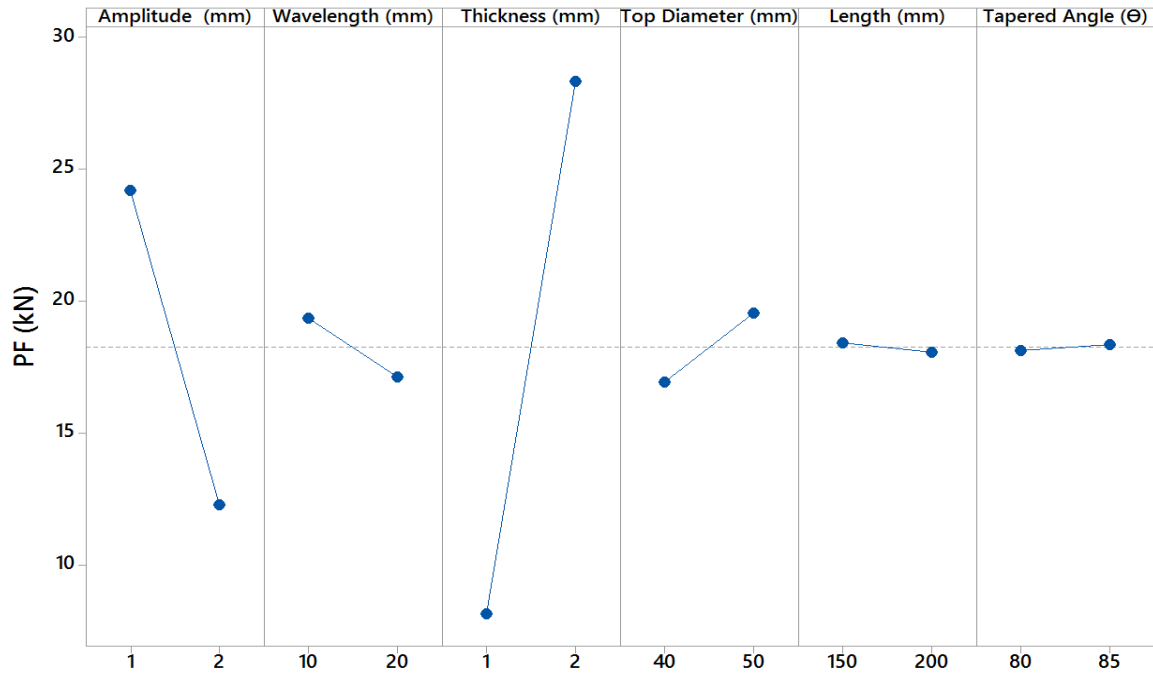


Figure 4-9: Influence of design parameters on IPF

- **Effect of Thickness, Top Diameter, Length, and Tapered Angle**

On the other hand, a significant increase in IPF is observed when the tube thickness changes from 1 mm to 2 mm. This is due to the stiffness increase that corresponds to the increased wall thickness, therefore increasing the initial load needed to start crushing, which is consistent with physical observations. Furthermore, a minor increase in IPF is observed when the tube's top diameter increases from 40 mm to 50 mm. This is due to the moment of inertia increase that corresponds to increasing the top diameter, which increases the tube resistance to progressive crushing and hence increases the initial load. Finally, neither the tube's length nor the tube's tapered angle has a notable influence on IPF.

- **The Most Influential Geometric Factors on PF**

The surface plot in Figure 4-10 depicts the interaction effect of the geometrical parameters of highest influence on IPF. It is evident from the figure that a CTT profile with low thickness value and longer corrugation's amplitude would have the lowest initial peak force.

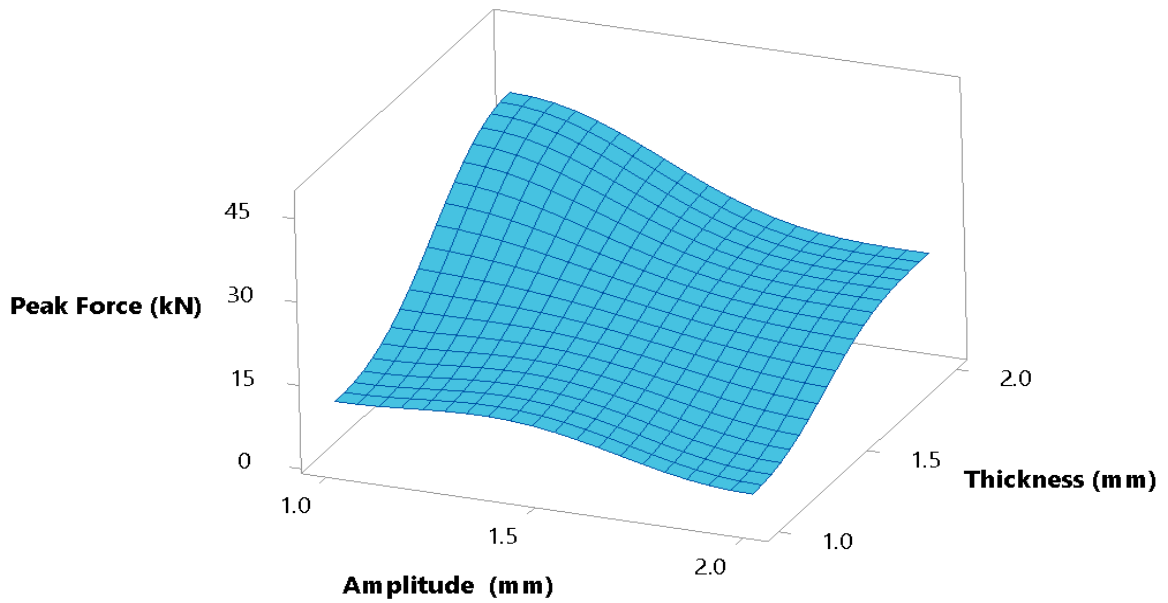


Figure 4-10: The effect of Amplitude-Thickness interaction on IPF

4.4.2 Influence on Mean Force (MF)

- **Effect of Amplitude and Wavelength**

The mean force (MF) represents the average crushing force maintained by the tube during the crushing process. A higher value of MF indicates higher energy absorption as well as higher initial peak load. Figure 4-11 shows the MF values of CTTs of different amplitudes and wavelengths relative to a conventional tapered tube. From here, it is evident that the average force of a regular tapered tube is generally higher than the CTTs depicted in the figure, except for CTT of $A=1\text{ mm}$ and $W=10\text{ mm}$.

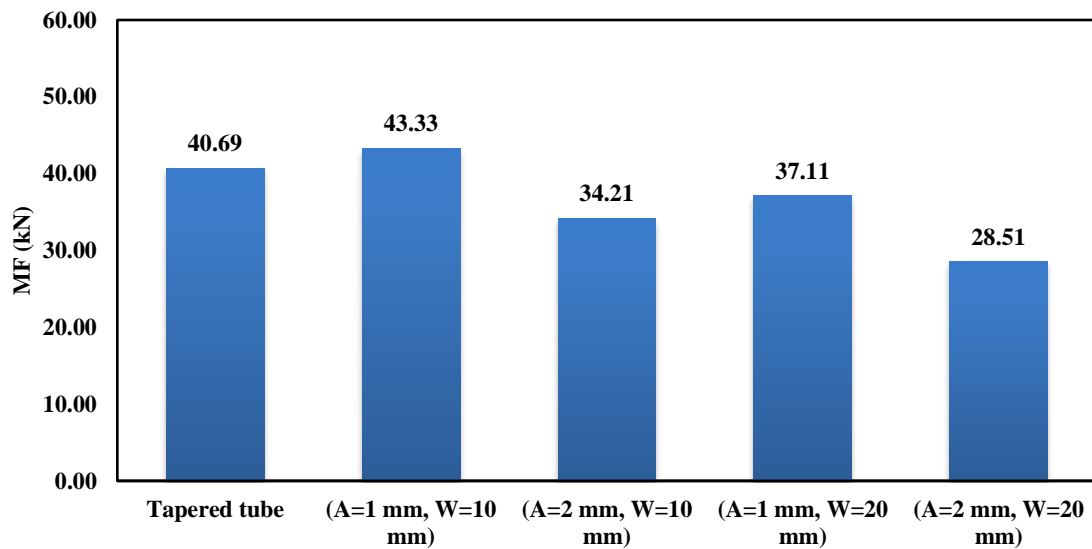


Figure 4-11: MF values for CTT profiles relative to a conventional tapered tube ($L = 200\text{ mm}$, $D = 50\text{ mm}$, $t = 2\text{ mm}$ and Tapered angle = 80°)

Figure 4-12 shows the average effect of CTT's geometrical parameters on MF. It is clear from the figure that increasing the amplitude and wavelength reduces MF, which is similar to their effect on IPF. This is logical, as adopting corrugation reduces the initial force needed to start deformation, and therefore the crushing forces along the tube's length are reduced.

- **Effect of Thickness, Top Diameter, Length, and Tapered Angle**

In addition, MF has the similar tendency as IPF for the thickness and the top diameter, as increasing both results in an increase in MF (Refer to the previous section). Finally, increasing the tapered angle results in a minor decrease in MF, while the length has no significant effect on MF.

- **The Most Influential Geometric Factors on MF**

Figure 4-13 shows the interaction effect of the geometrical parameters of highest influence on MF. The interaction effect of amplitude and thickness on MF has the same tendency as in the case of IPF (Refer to Figure 4-9). An amplitude of 1 mm and a thickness value of 2 mm will result in the highest MF and IPF values.

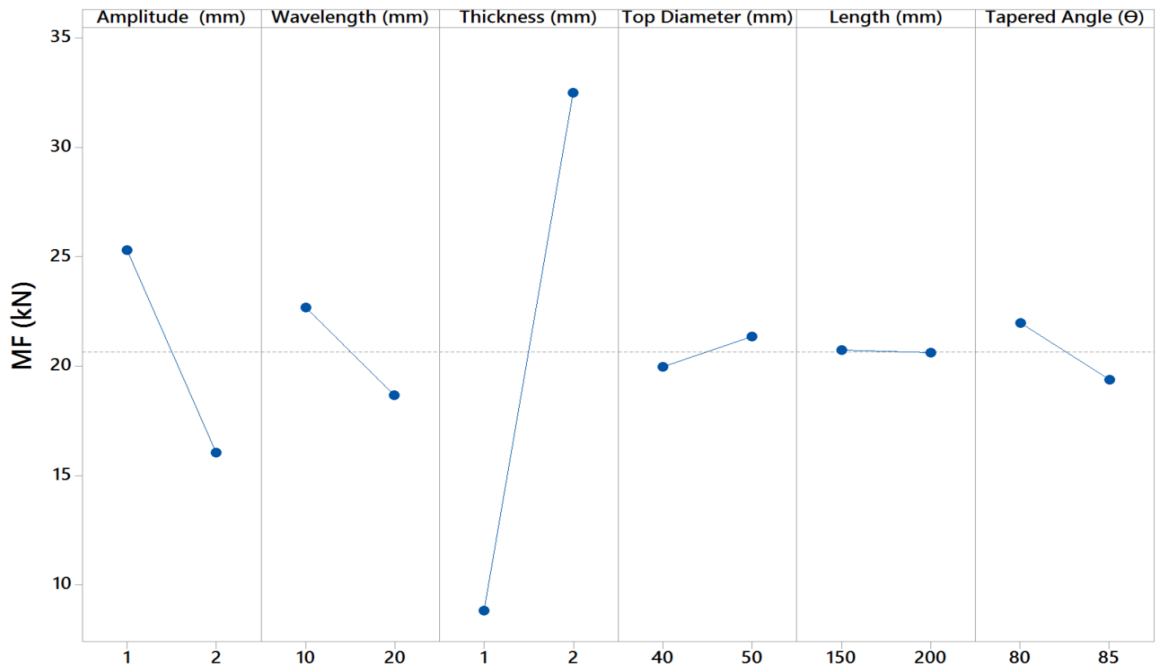


Figure 4-12: Influence of design parameters on MF

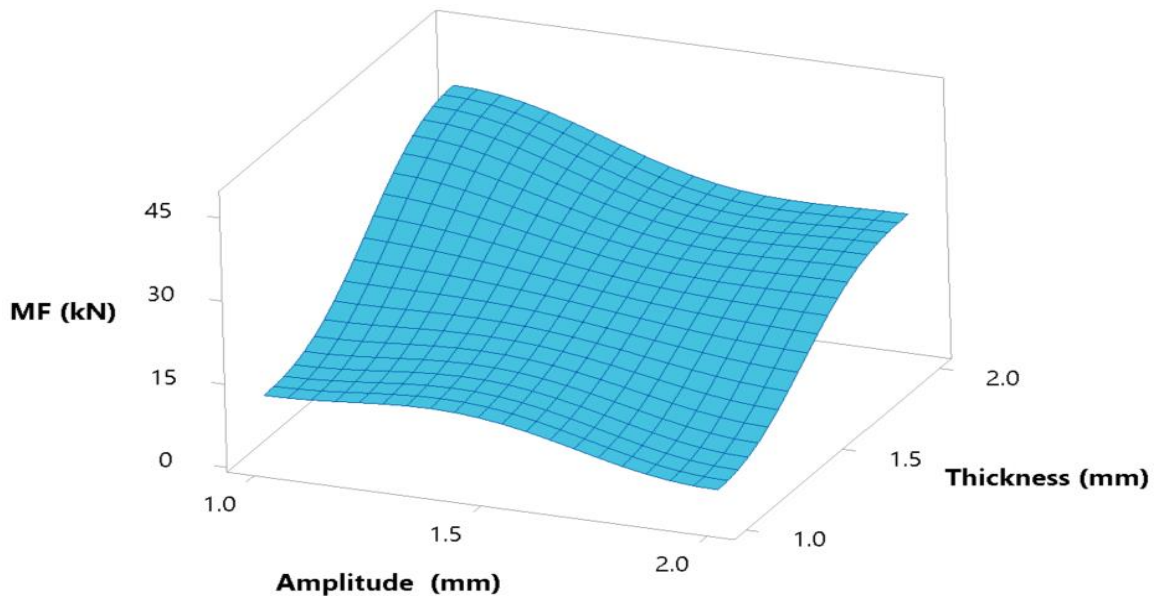


Figure 4-13: The effect of Amplitude-Thickness interaction on MF

4.4.3 Influence on Energy Absorption (EA)

- **Effect of Amplitude and Wavelength**

Figure 4-14 shows the energy absorption (EA) values for CTTs of different amplitudes and wavelengths relative to a conventional tapered tube. It is evident from here that EA of the conventional tapered tube is slightly higher than the depicted CTTs, except for CTT of $A=1\text{ mm}$ and $W=10\text{ mm}$. The lowest EA value for a CTT profile from the figure was 4.84 kJ ($A=2\text{ mm}$ and $W=20\text{ mm}$) which represents a reduction of 24.5% relative to the regular tapered tube (6.81 kJ). Figure 4-15 shows the average effect of the selected CTT's geometrical parameters on EA. It is evident from the figure that an increase in amplitude from 1 mm to 2 mm leads to a significant drop in energy absorption. Similarly, a decrease in EA is observed when the wavelength increases from 10 mm to 20 mm. This implies that although a reduction in IPF is achieved when corrugation is adopted, however, CTTs must sacrifice some energy absorption capacity for this reduction. This reduction has also been reported by [23-25, 91] for straight corrugated tubes.

- **Effect of Thickness, Top Diameter, Length, and Tapered Angle**

In addition, a reduction in EA is also observed when the tapered angle is increased from 80° to 85° . This is related to the bending moment decrease that corresponds to tapered angle increase (lower diameter reduces), resulting in less buckling which reduces the energy absorbed by the tube.

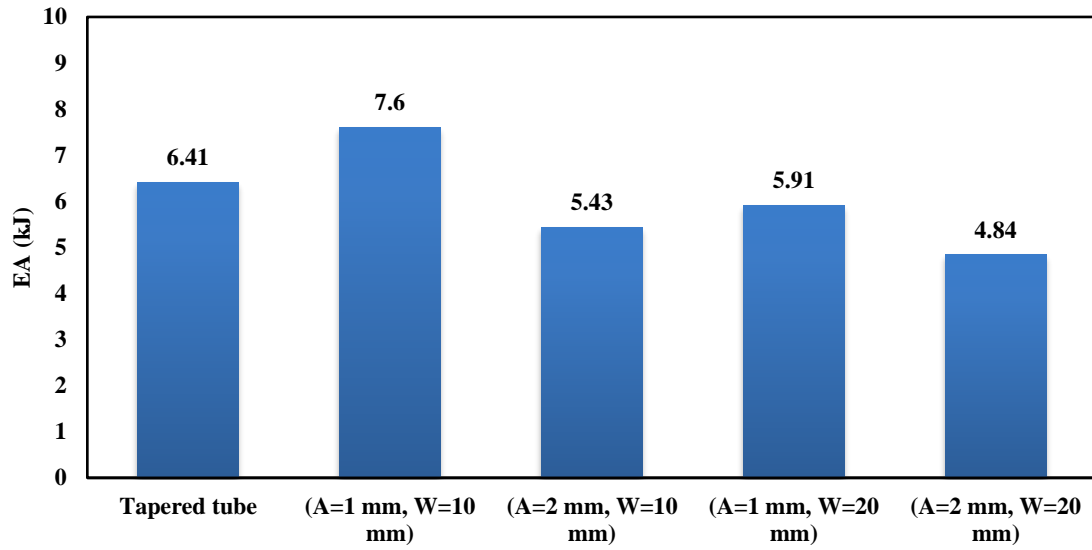


Figure 4-14: EA values for CTT profiles relative to a conventional tapered tube ($L = 200$ mm, $D = 50$ mm, $t = 2$ mm and Tapered angle = 80°)

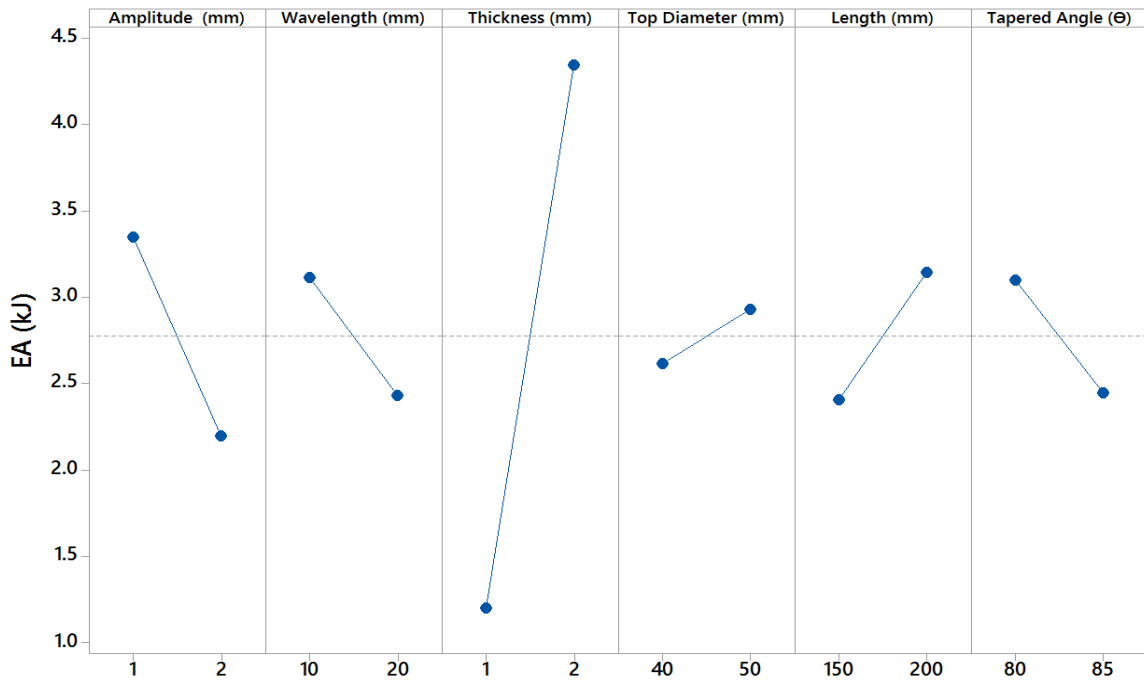


Figure 4-15: Influence of design parameters on EA

On the other hand, a significant increase in EA is obtained when the thickness increases from 1 mm to 2mm. This is due to the tube's mass increase resulting from increasing the wall thickness, which results in more tube's material that can absorb more energy. Likewise, the increase in EA when the tube's length increases from 150 mm to 200 mm, and the top diameter from 40 mm to 50 mm is attributed to the same reason.

- **The Most Influential Geometric Factors on EA**

Figure 4-16 shows the interaction effect of the geometrical parameters of highest influence on EA. It can be intuitively seen that a tube with an amplitude of 1 mm and a wall thickness of 2 mm will have the highest EA. However, this combination will lead to a higher IPF which is not a desirable performance indicator. Therefore, a tradeoff between IPF and EA needs to be done.

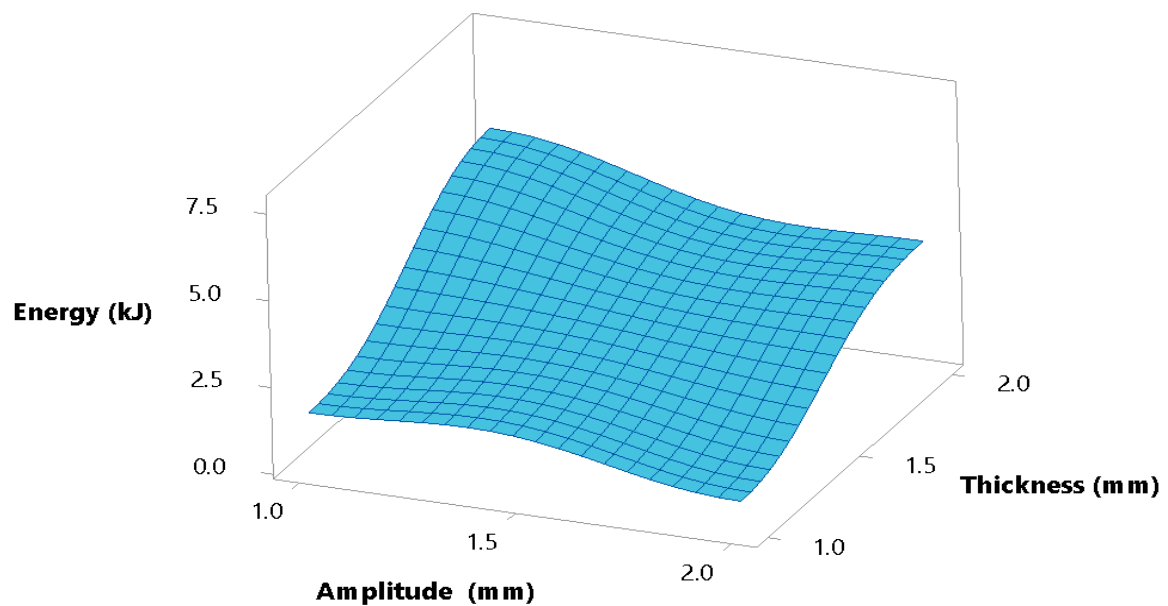


Figure 4-16: The effect of Amplitude-Thickness interaction on EA

4.4.4 Influence on Specific Energy Absorption (SEA)

- **Effect of Amplitude and Wavelength**

Figure 4-17 shows the specific energy absorption (SEA) values for CTTs relative to a conventional tapered tube. It is clear from the figure that SEA has the same tendency as EA, as all the CTT profiles exhibit lower SEA than the conventional tapered tube. As Figure 4-17 shows, the regular tapered tube has an SEA of 27.47 kJ/kg, while the highest SEA value for CTT depicted in the figure was 26.84 kJ/kg ($A=1$ mm and $W=10$ mm). The low performance of CTTs in terms of SEA can be explained by their low energy absorption capacity and high mass relative to conventional tapered tubes. Figure 4-18 shows the average effect of CTT geometrical parameters on SEA. From here it is clear that increasing the amplitude from 1 mm to 2 mm reduces SEA significantly. Moreover, increasing the corrugation's wavelength from 10 mm to 20 mm introduces a minor reduction in SEA. This is due to the reduction in EA and the mass increase that corresponds to increasing the amplitude and wavelength of corrugation.

- **Effect of Thickness, Top Diameter, Length, and Tapered Angle**

Furthermore, a reduction in SEA is observed when the top diameter increases from 40 mm to 50 mm, and when the tube's length increases from 150 mm to 200 mm. This is also due to the mass increase resulting from increasing the diameter and the length of the tube.

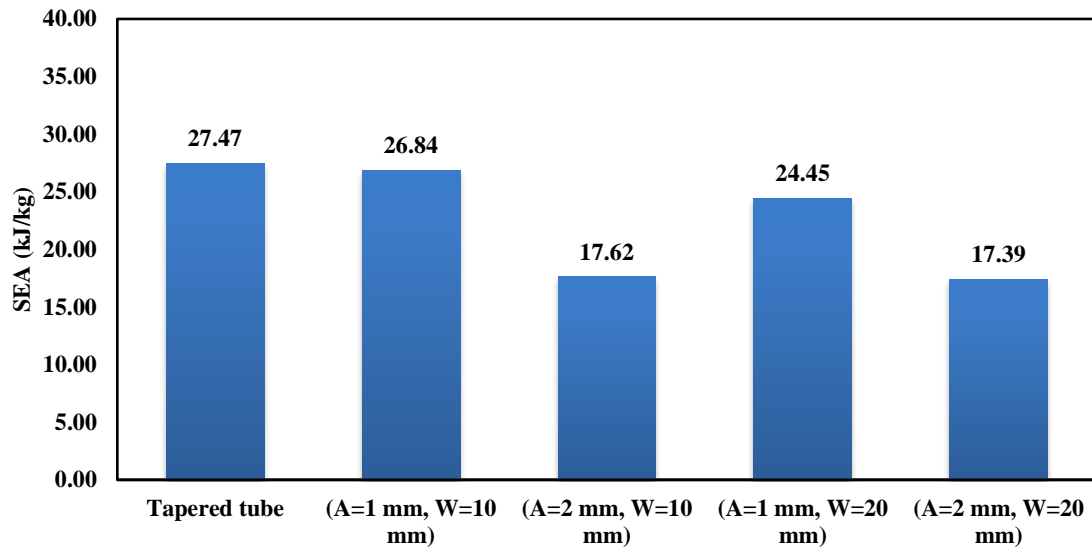


Figure 4-17: SEA values for CTT profiles relative to a conventional tapered tube ($L = 200$ mm, $D = 50$ mm, $t = 2$ mm and Tapered angle = 80°)

On the other hand, a significant increase in SEA is noted with the increase in thickness from 1 mm to 2 mm. This is because of the energy absorption increase that corresponds to the thickness increase. Although a mass increase occurs when the thickness is increased, however, the energy absorption resulting from this increase is more dominant than the mass increase and thus increases SEA. Similarly, increasing the tapered angle from 80° to 85° results in higher SEA. This is mainly due to the mass reduction that corresponds to the tapered angle increase.

- **The Most Influential Geometric Factors on SEA**

Figure 4-19 depicts the interaction effect of the geometrical parameters of highest influence on SEA. Similar to the effect on EA, lowering the amplitude to 1 mm and increasing the thickness to 2 mm will result in the highest SEA. However, this will lead to

a higher IPF. Hence, a tradeoff between SEA/EA and IPF needs to be done as mentioned earlier.

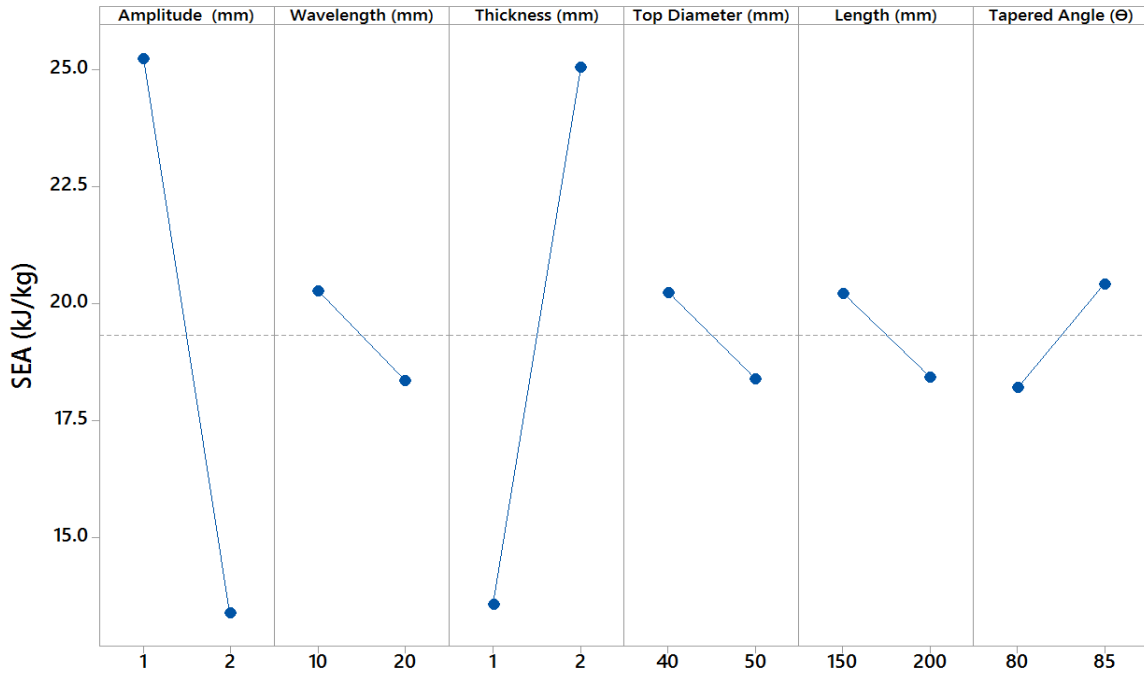


Figure 4-18: Influence of design parameters on SEA

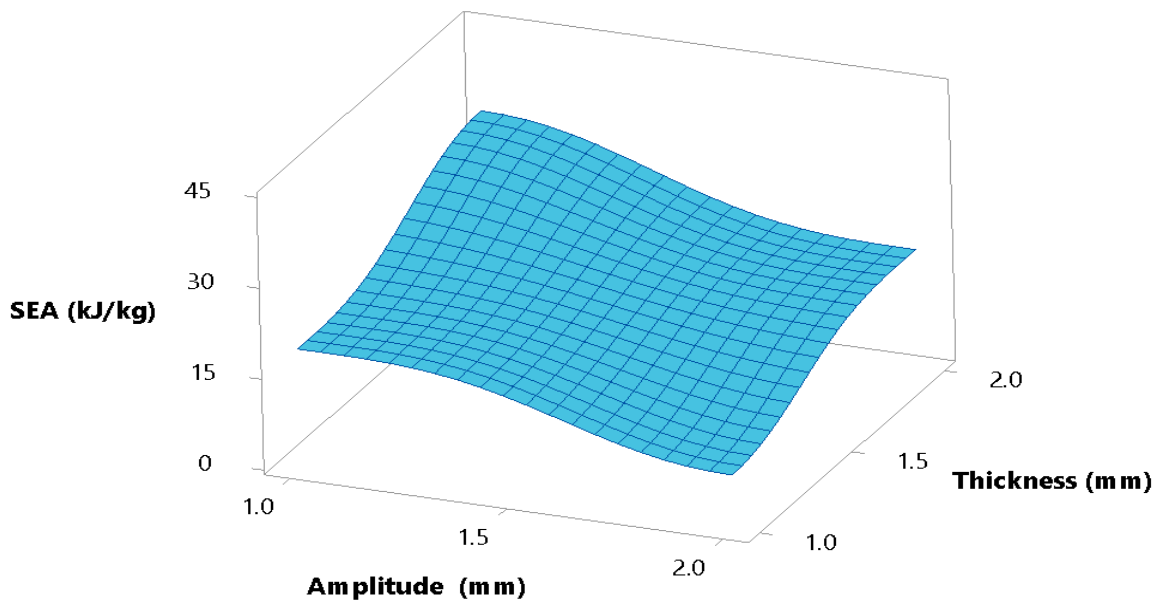


Figure 4-19: The effect of Amplitude-Thickness interaction on SEA

4.5 Summary

The results presented in the previous sections showed that some of the geometrical parameters have a significant effect on the performance indicators of CTTs while others have a slight or no effect. The geometrical parameters with the most significant influence on the performance indicator were the tube's amplitude of corrugation and the wall thickness. For the selected range of geometrical parameters values, it was found that longer amplitude (2 mm) will lead to lower initial peak force. However, the longer amplitude will result in a lower energy and specific energy absorption (EA & SEA) performance. On the other hand, increasing the wall thickness was found to enhance the energy and specific energy absorption. However, it will result in a higher initial peak force (IPF) which is not a desired performance indicator. The geometrical parameters' influence shows that it is

impossible to select an amplitude or thickness values that will simultaneously result in optimum performance. This is depicted by the amplitude-thickness performance influence paradox shown in Figure 4-20. The figure indicates that the effect of each parameter is opposite to the other. Hence, a tradeoff between the geometrical parameters' values should be made to obtain a balanced performance.

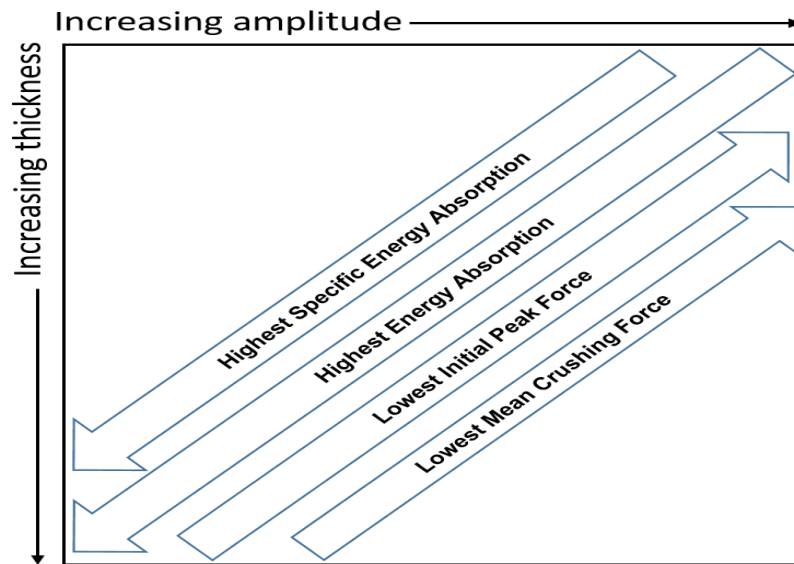


Figure 4-20: Amplitude-thickness performance influence paradox under the tested geometric factors' range: (Thickness: 1-2 mm, Amplitude= 1-2 mm)

Published work from this chapter:

S. E. Alkhatib, F. Tarlochan, and A. Eyvazian, "Collapse behavior of thin-walled corrugated tapered tubes," *Engineering Structures*, vol. 150, pp. 674-692, 11/1/ 2017. (Impact Factor: 2.258)

CHAPTER 5: CORRUGATED TAPERED TUBES UNDER OBLIQUE LOADING

5.1 Introduction

This chapter discusses the performance of corrugated tapered tubes under oblique loading conditions. First, the force-displacement behavior of corrugated tubes under different impact angles is discussed and compared to conventional tapered tubes. The deformation modes and collapse behavior are then explained for corrugated tapered tubes of different categories. Furthermore, the effect of loading angles and geometric parameters on the performance indicators is explained. Finally, a comparative analysis of the corrugated tapered tubes and conventional tapered tubes is presented in terms of specific energy absorption and mean crushing force.

5.2 Force-Displacement Characteristics

The results obtained from the crushing simulations of CTTs under different loading conditions are summarized in Table 5 to Table 8 in the appendix, for the reader's convenience. The performance indicators' values in these tables were calculated at a given displacement (=100 mm) to meaningfully and fairly facilitate the comparison of the performance of the tubes under different loading angles. This displacement point was selected as all the tubes have deformed sufficiently at it. Figure 5-1 and Figure 5-2 show the force-displacement characteristics of a representative CTT ($A=1$ mm, $W=20$ mm) and a conventional circular tapered tube under different loading angles, respectively. The first clear observation from the figures is that the crushing forces of CTTs are lower than the forces of the regular tapered tube. This is due to the corrugated surface of CTT that

works as deformation trigger that reduces the dynamic crushing forces. Furthermore, it is evident from the figures that both tubes experience the highest initial peak force under axial impact (loading angle = 0°). The axial crushing characteristics are also similar to both tubes as the crushing forces keep oscillating after the initial peak force, with less force fluctuation for CTT due to its corrugated surface as mentioned earlier. Furthermore, the initial peak force and magnitude of force oscillations tend to reduce as the impact angle increases to 10° and continue to decrease as the loading angle increases up to 40° as observed in previous studies [11, 20]. This is because tubular structures under oblique loading conditions experience two categories of mechanical loadings, mainly bending (particularly at the high impact angles) while undergoing some form of axial crushing.

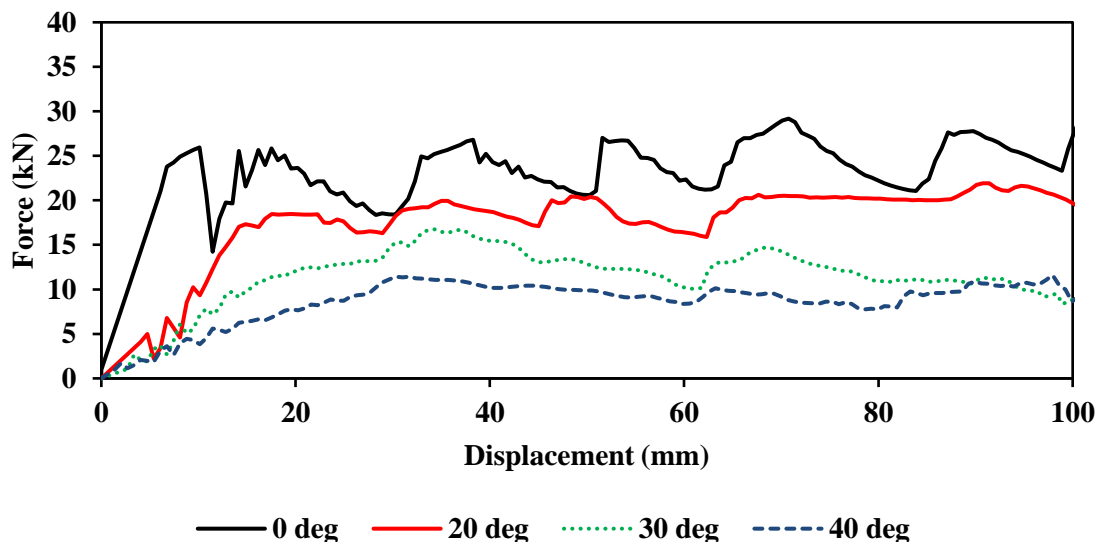


Figure 5-1: Force-Displacement Diagram for CTT ($A = 1$ mm, $W = 20$ mm, Tapered Angle = 85° and Thickness = 2 mm)

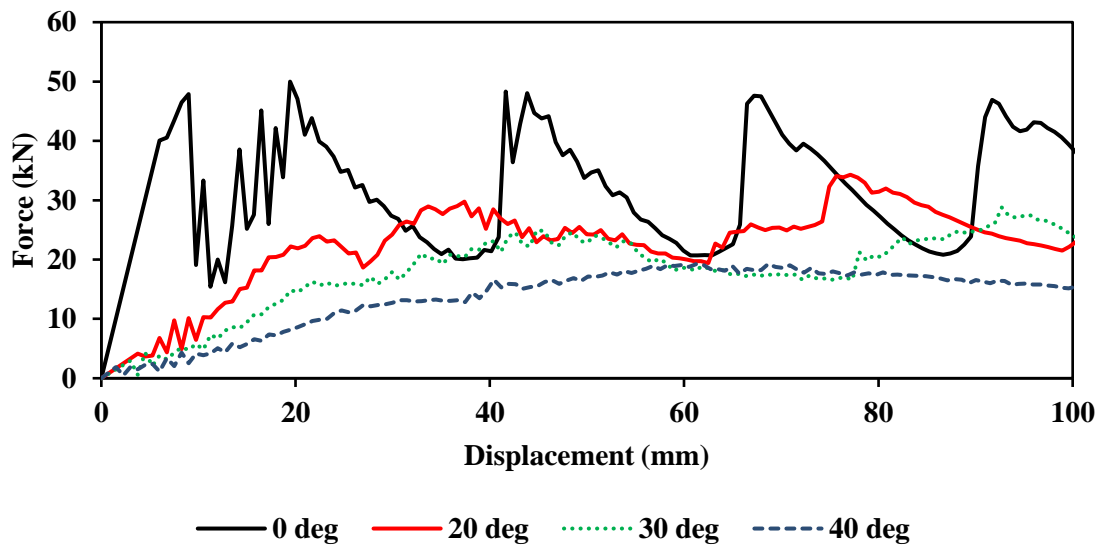


Figure 5-2: Force-Displacement Diagram for a Regular Circular Tapered Tube (Tapered Angle = 85° and Thickness = 2 mm)

5.3 Deformation Modes

It was found through the results of the entirety of the conducted simulations that all of the tested CTTs undergo progressive axial crushing under the impact angles of 0° and 10° , despite the differences in geometric parameters. However, beyond the impact angle of 10° (under higher impact angles), the axial crushing pattern tends to shift to the sides leading to global Euler buckling. Global Euler buckling tends to reduce the performance of the structure because it inhibits its capacity to absorb the maximum amount of the impact energy. This transition between progressive crushing and global Euler buckling is different for each structure and depends mainly on the geometric configuration of CTTs. To understand the effect of CTT's geometric parameters on the transition to global Euler buckling, the final deformation modes of CTTs of different wall thickness values and

tapered angles are shown in Figure 5-3 to Figure 5-6 for different loading angles. Each figure represents a group of CTTs of different corrugation's amplitudes and wavelengths.

Figure 5-3 shows the final deformation modes of CTTs of 1 mm amplitude and 10 mm wavelength. From here, it can be seen that the transition to global Euler buckling happens at higher impact angles for structures of tapered angle of 80° compared to a tapered angle 85° . This is evident from Figure 5-3a and Figure 5-3b, where global Euler buckling occurs at 25° and 40° load angles, respectively. This can be attributed to the larger lower diameter that corresponds to a tapered angle of 80° , which enhances the stability of the structure under oblique loading conditions. On the other hand, global Euler buckling develops at an impact angle of 15° for CTTs of 85° tapered angles in this category, for both 1 and 2 mm thickness (Figure 5-3c - Figure 5-3d).

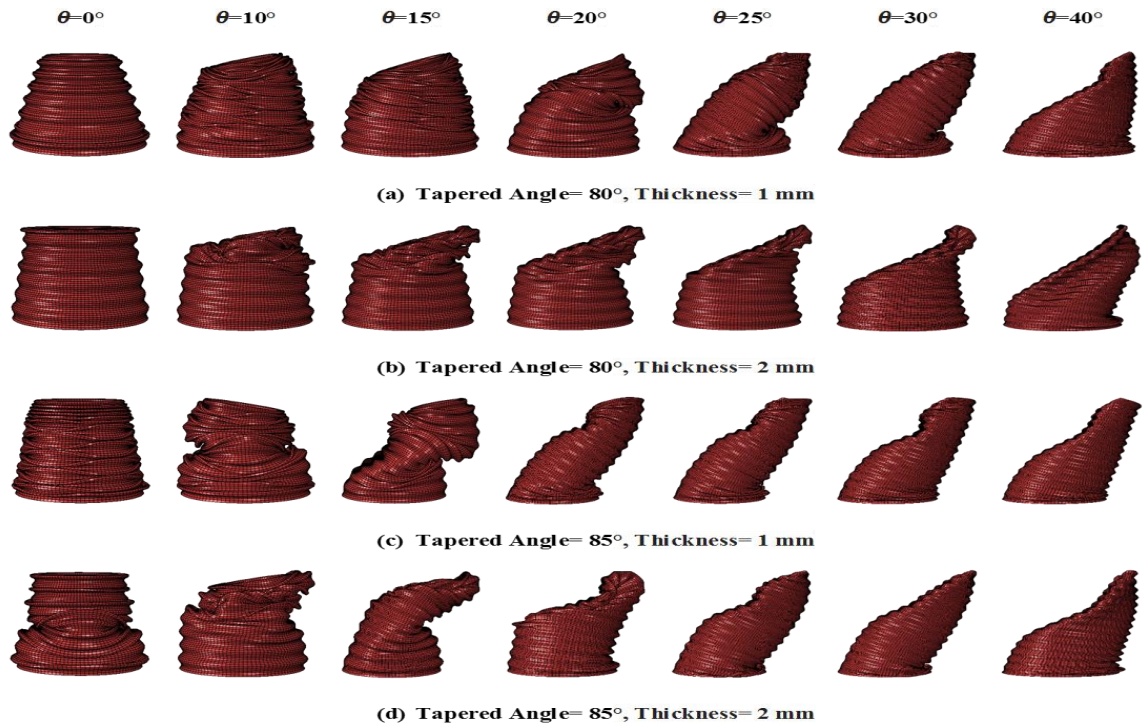


Figure 5-3: Final Deformation Modes for CTT (A=1 mm, W=10 mm)

Figure 5-4 illustrates the deformation modes of CTTs category of 1 mm amplitude and 20 mm wavelength. Similar to the previous category, global Euler buckling exists at higher impact angles for structures of 80° tapered angles relative to their opposites of 85° tapered angles. This is evident from Figure 5-4a where global Euler buckling occurs at 40° load angle, and from Figure 5-4b where it occurs at 30° load angle. On the contrary, global Euler buckling exists at an impact angle of 20° for structures of 85° tapered angle in this category (Figure 5-4c - Figure 5-4d).

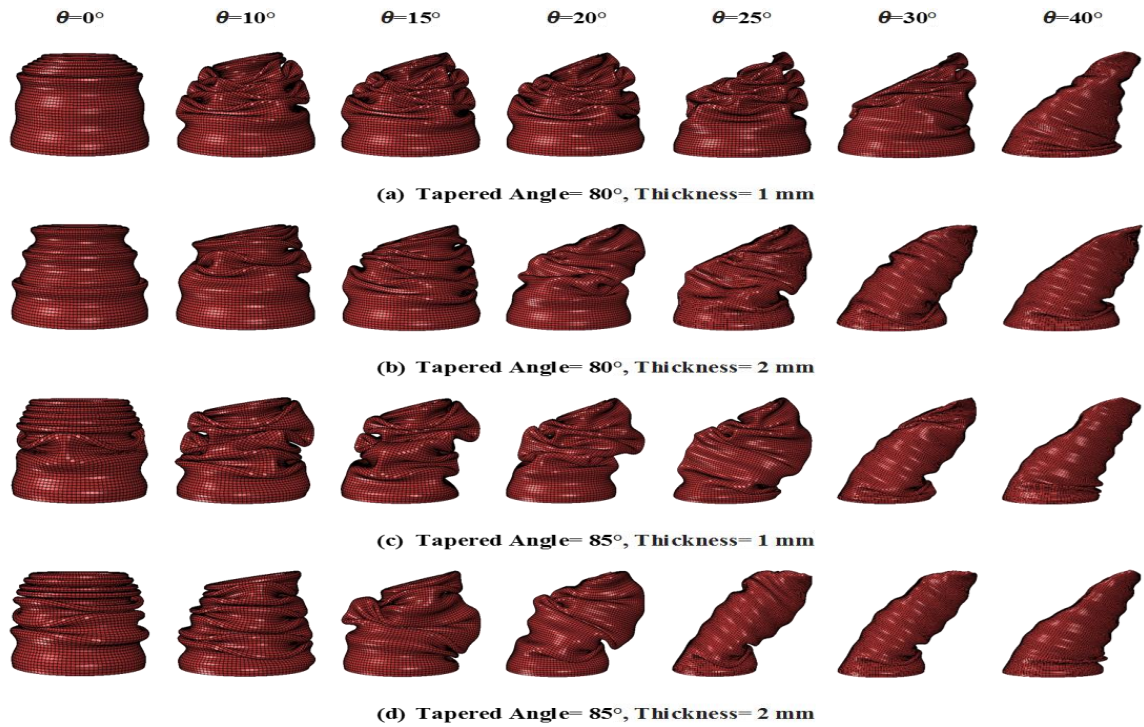


Figure 5-4: Final Deformation Modes for CTT (A=1 mm, W=20 mm)

Figure 5-5 shows the final deformation modes of CTTs of 2 mm amplitude and 10 mm wavelength. Unlike the previous two categories (Figure 5-3 and Figure 5-4), in which the corrugation's amplitude was 1 mm, the influence of the tapered angle on the transition to global Euler buckling is not significant. This can be observed from the figure, in which global Euler buckling develops at a lower impact angle of 15° for all the tested tubes in this category except the one depicted in Figure 5-5a, in which global Euler buckling occurs at an impact angle of 20° . This implies that a CTT of 2 mm amplitude and 10 mm wavelength is very unstable under oblique loading conditions.

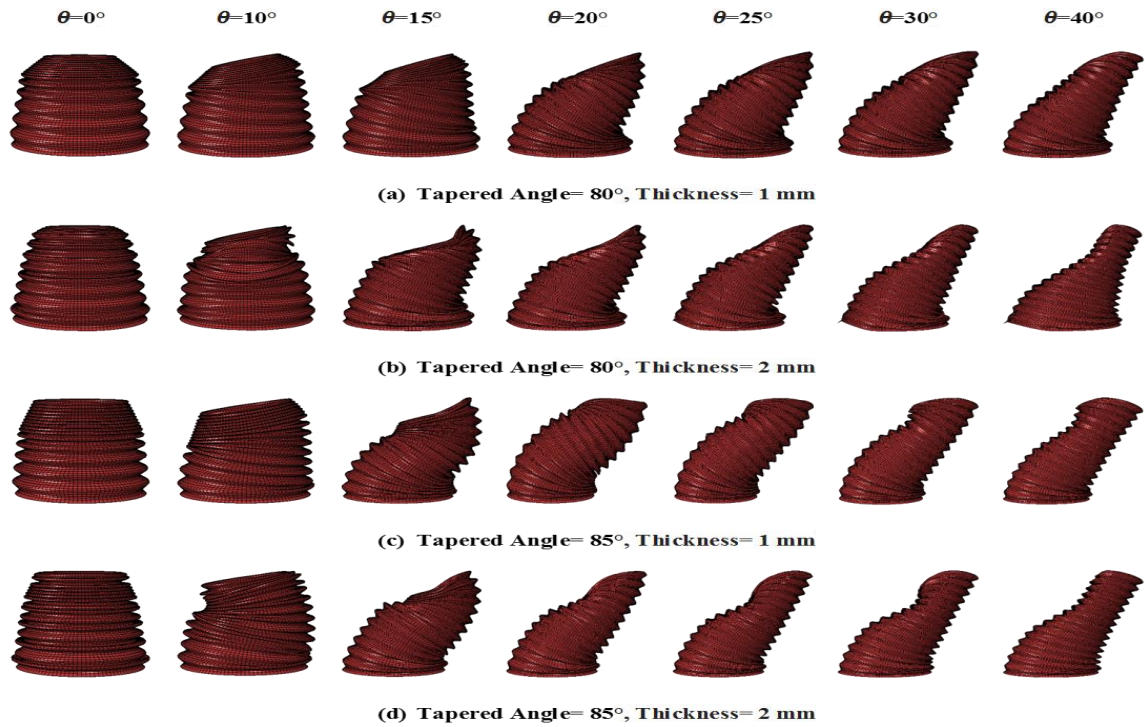


Figure 5-5: Final Deformation Modes for CTT (A=2 mm, W=10 mm)

On the other hand, CTTs of 2 mm amplitude and 20 mm wavelength are influenced by the tapered angle, as global Euler buckling is observed at higher impact angles for structures of 80° tapered angle in this category. This is evident from Figure 5-6a and Figure 5-6b in which global Euler buckling occurs at 30° and 25°, respectively. Conversely, for the structures depicted in Figure 5-6c and Figure 5-6d with a tapered angle of 85°, global Euler buckling develops at 20°.

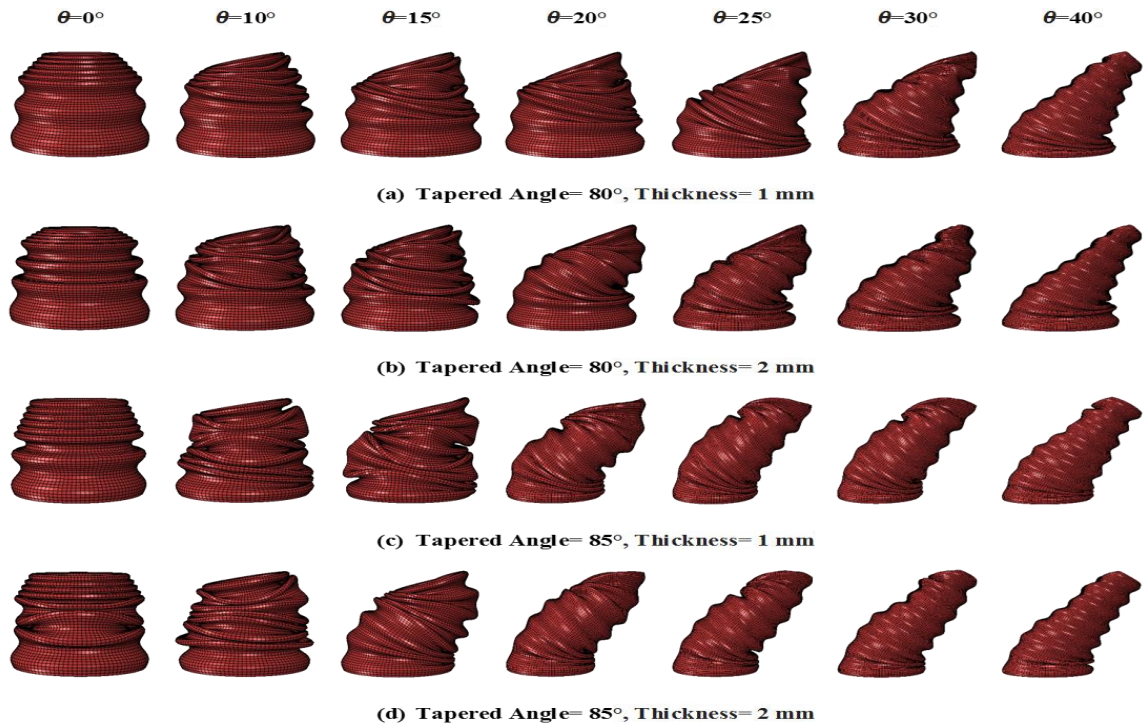


Figure 5-6: Final Deformation Modes for CTT (A=2 mm, W=20 mm)

5.4 Performance Analysis

5.4.1 Influence of Loading Angle

As previously mentioned, oblique loading conditions inhibit the performance of the structure in terms of energy absorption. That is due to the two loading types the structure undergoes under oblique impacts: bending and axial crushing. To precisely understand the effect of impact angles on CTTs' performance, the main effect plots shown in Figure 5-7 to Figure 5-10 depict the performance indicators (Energy Absorption, Specific Energy Absorption, Initial Peak Force and Mean Force) behavior under different loading angles. From here, it is evident that the highest initial peak force occurs under axial loading (Impact

Angle =0°), and then it drops significantly at an impact angle of 10° and continues to decrease as the impact angle reaches 40° as shown in Figure 5-7. This observed substantial decline in IPF with the increase of the impact angle was reported by other studies on thin-walled structures under oblique impact [11, 20].

Furthermore, the mean force (MF) follows the same pattern under the tested impact angles, however uniformly throughout the impacting angles range, as MF continues to decrease with the increase of the impact angle as shown in Figure 5-8. A similar observation was also reported by other studies on similar loading conditions [11, 20, 78]. This reduction in MF can be attributed to the decrease in initial peak force mentioned earlier. Another possible reason for this drop is that higher impact angles shift the lobes that form under progressive crushing away from the structure's central axis, leading to a low overall deformation of the structure under large impact angles.

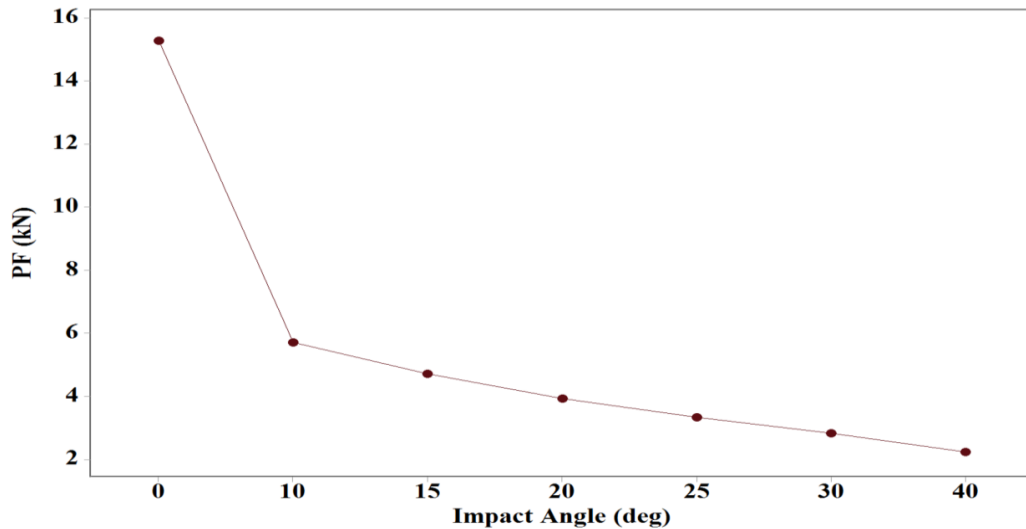


Figure 5-7: Effect of Load Angle on the Initial Peak Force IPF

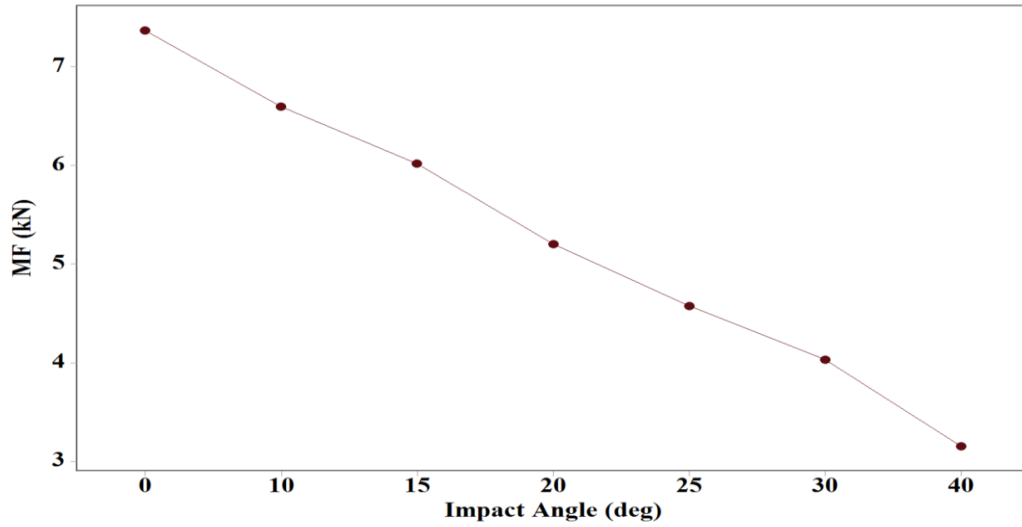


Figure 5-8: Effect of Load Angle on the Mean Force (MF)

In the same manner, the energy absorption (EA) and specific energy absorption (SEA) reduce as the loading angle increases as shown in Figure 5-9 and Figure 5-10. The reduction in EA and SEA was found to be approximately 54% as the impact angle increases from 0° (axial crushing) to 40°. This decrease is mainly due to the reduction in MF that is associated with the increasing the loading angle.

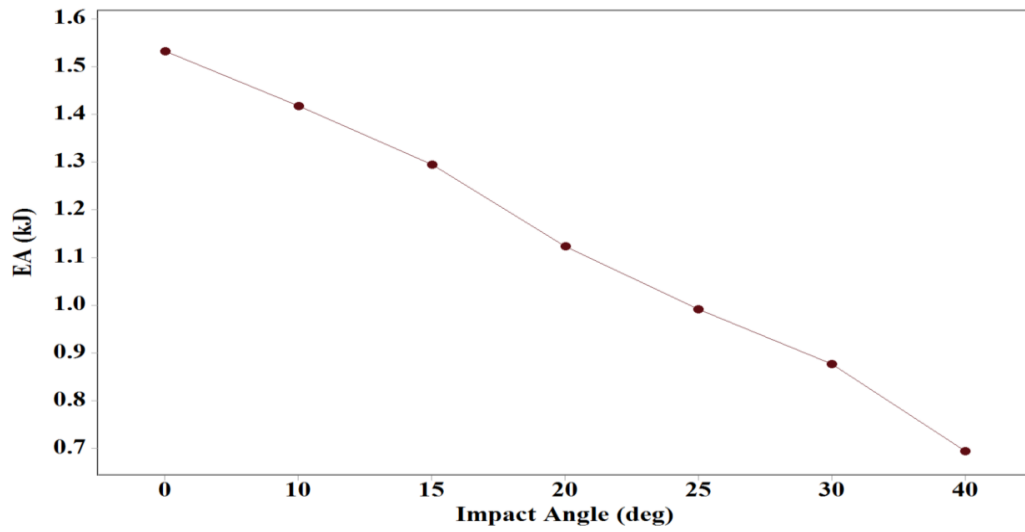


Figure 5-9: Effect of Load Angle on the Energy Absorption (EA)

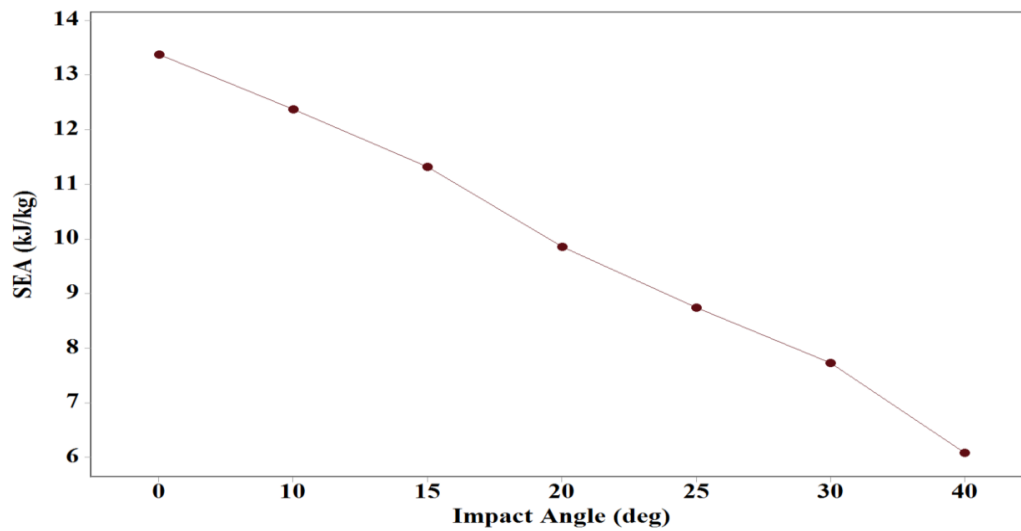


Figure 5-10: Effect of Load Angle on the Specific Energy Absorption (SEA)

5.4.2 Influence of Geometric Parameters

It is vital to understand the influence of CTTs' geometric parameters on their performance as energy absorbing structures. Therefore, to solely investigate the effect of each geometric parameter on the performance of CTTs, the average effect of corrugation's amplitude, corrugation's wavelength, wall thickness, and tapered angle on performance indicators under different loading angles is discussed in the following sections.

5.4.2.1 Influence on Initial Peak Force

Figure 5-11 shows the average effect of corrugation's amplitude on the initial peak force (IPF). From here, it is observed that an amplitude of 1 mm will result in higher IPF value, up to a load angle of 15°. However, at higher impacting angles, an amplitude of 2 mm will lead to a higher IPF.

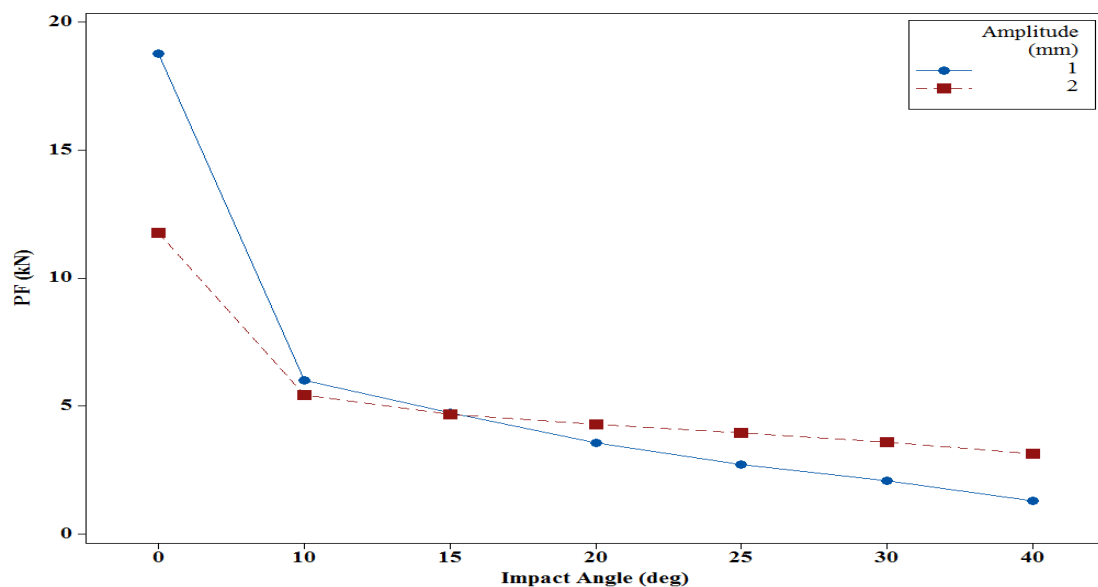


Figure 5-11: The Average Effect of Amplitude on IPF Under Different Loading Angles

As for the corrugation's wavelength, a wavelength of 10 mm was found to result in higher initial peak force values compared to a wavelength of 20 mm (See Figure 5-12). Furthermore, the wall thickness has a significant effect on IPF as shown in Figure 5-13. From the figure, it is observed that a thickness value of 2 mm will result in higher IPF along the range of the tested impact angles. This can be attributed to the structure's stiffness increase caused by the thick walls, which lead to an increase in the initial load required to deforming the structure. Finally, the tube's tapered angle was not found to have a significant influence on the initial peak force throughout the tested impacting angles (See Figure 5-14).

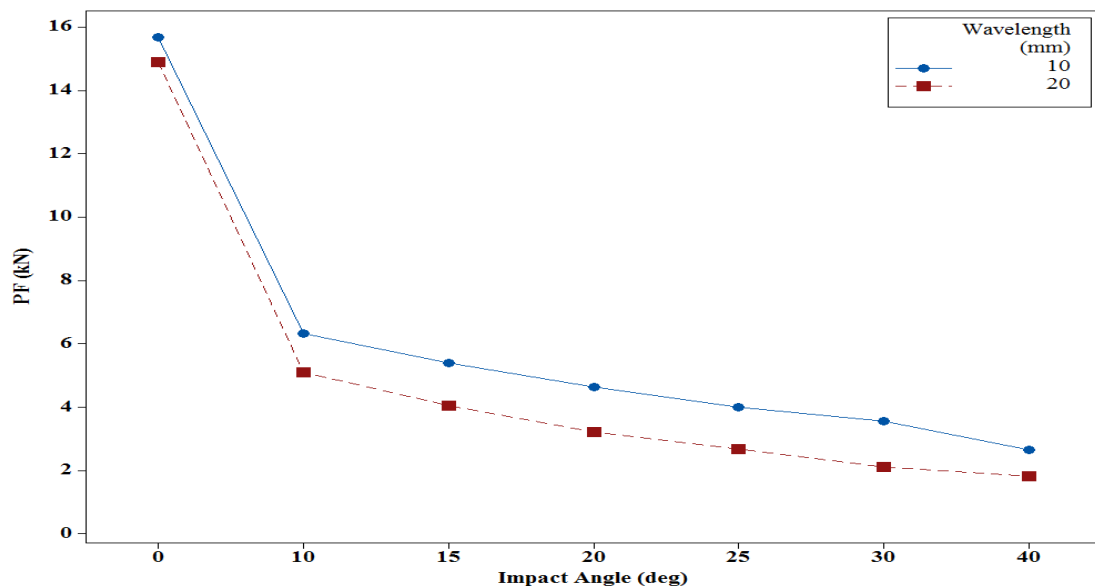


Figure 5-12: The Average Effect of Wavelength on IPF Under Different Loading Angles

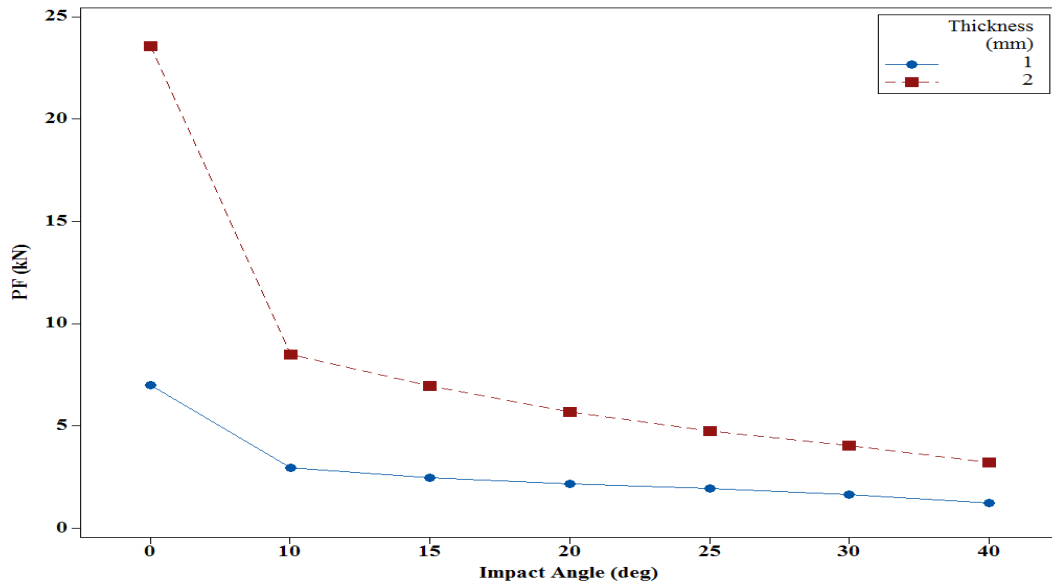


Figure 5-13: The Average Effect of Thickness on IPF Under Different Loading Angles

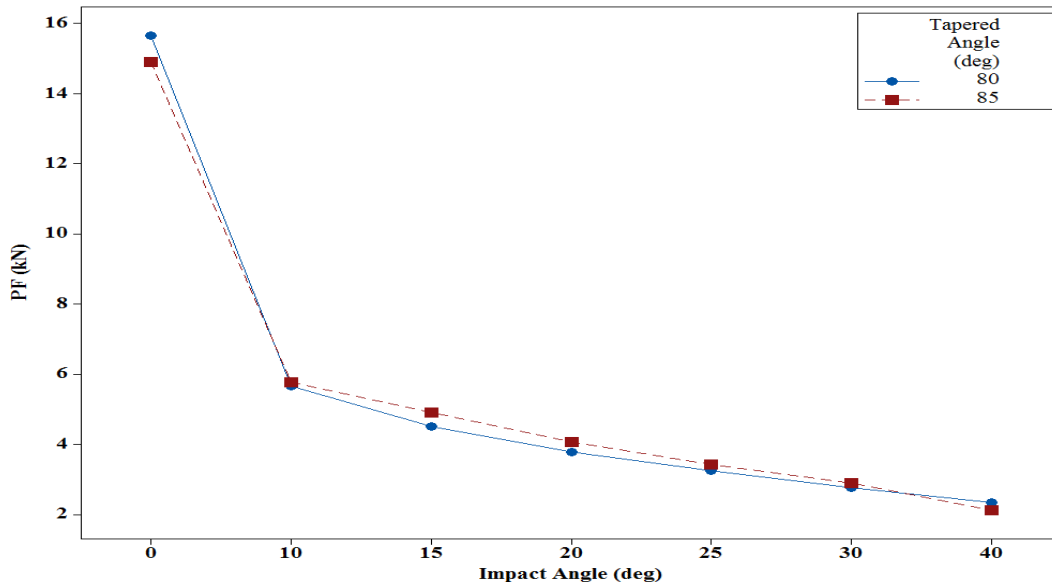


Figure 5-14: The Average Effect of Tapered Angle on IPF Under Different Loading Angles

5.4.2.2 Influence on Mean Force

The mean force is the crushing force maintained by the structure along its total length throughout the entire crushing process. The mean force value gives an indication of the energy absorption as high mean crushing force implies higher energy absorption. Figure 5-15 illustrates the average effect of corrugation's amplitude on MF under the tested range of impact angles. It is evident from the figure that an amplitude of 1 mm leads to a higher MF values relative to an amplitude of 2 mm. The same behavior is observed for a wavelength of 10 mm as shown in Figure 5-16. This can be explained by the fact that longer corrugation's amplitudes and wavelengths reduce the force needed to deform the structure and hence reduces the mean force.

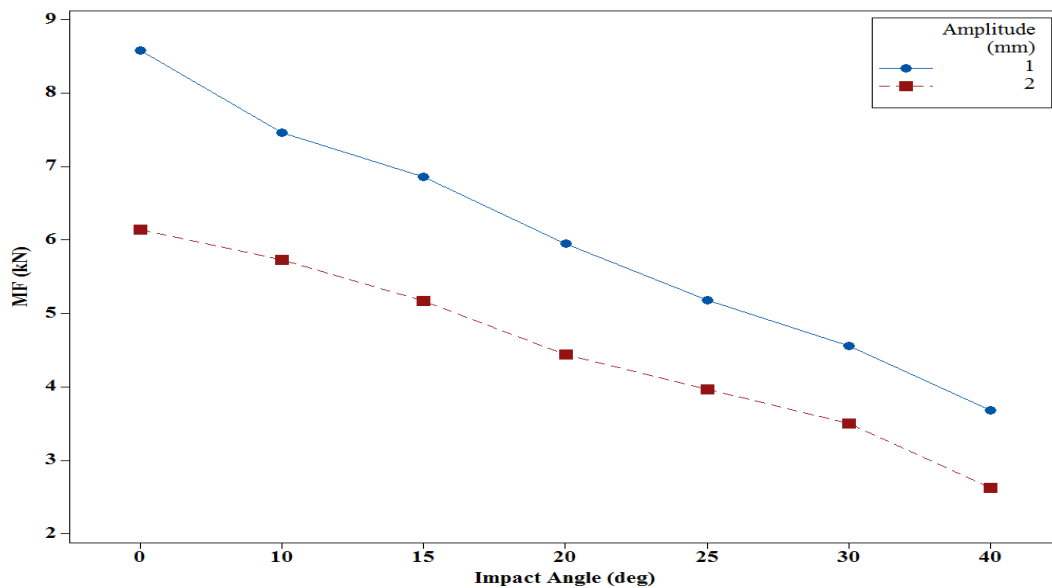


Figure 5-15: The Average Effect of Amplitude on MF Under Different Loading Angles

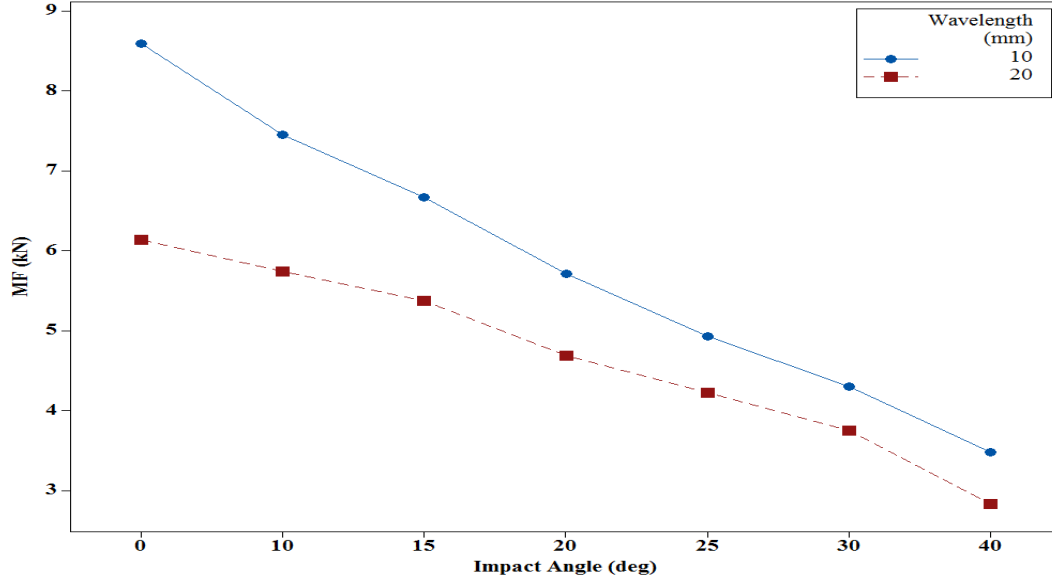


Figure 5-16: The Average Effect of Wavelength on MF Under Different Loading Angles

Furthermore, increasing the thickness from 1 mm to 2 mm will lead to increasing MF for all the tested impact angles (See Figure 5- 17). This is attributed to the structure’s stiffness increase that is associated with the increased wall thickness, which increases the amount of force needed to start deformation. Finally, a tapered angle of 80° will result in higher MF values along the tested range of impact angles as shown in Figure 5-18. This is due to the increase in the lower structure’s diameter when the tapered angle is 80° , promoting axial crushing under large angles and hence increasing MF. Similar results were reported for circular tapered tubes tested under oblique loading conditions [95].

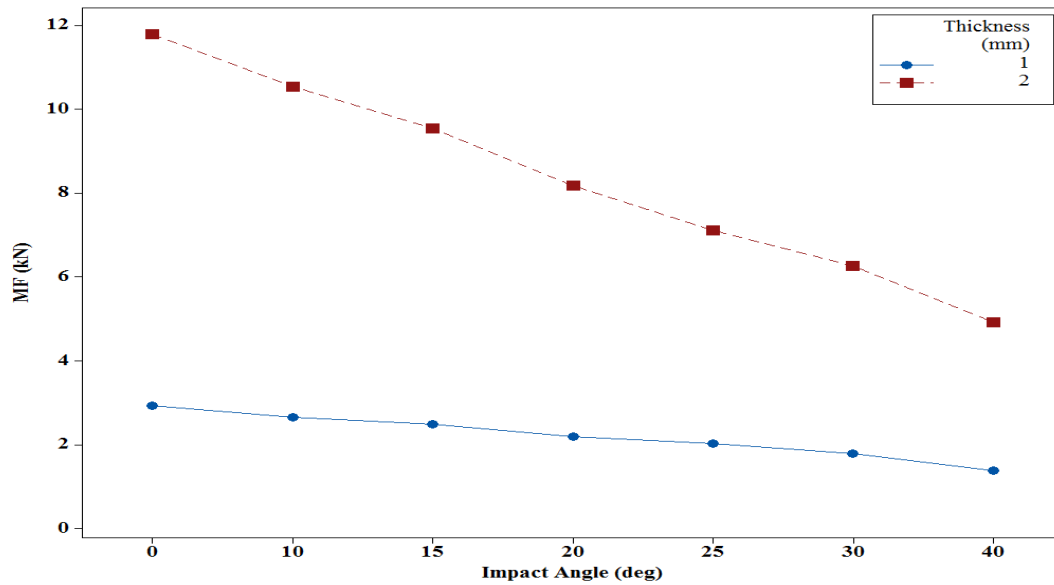


Figure 5- 17: The Average Effect of Thickness on MF Under Different Loading Angles

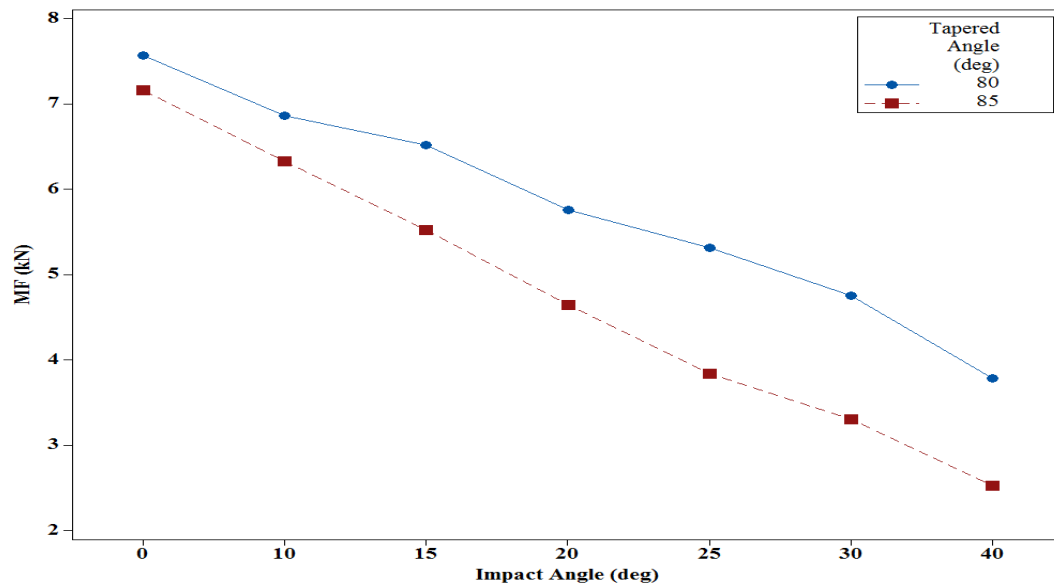


Figure 5-18: The Average Effect of Tapered Angle on MF Under Different Loading Angles

5.4.2.3 Influence on Energy Absorption

Figure 5-19 depicts the effect of corrugation's amplitude on the energy absorption along the tested impact angles. Similar to the effect of corrugation's amplitude on MF, an amplitude of 1 mm will have higher EA as opposed to 2 mm for all of the tested impact angles. Similarly, a wavelength of 10 mm will result in higher energy absorption compared to 20 mm as shown in Figure 5-20. This is logical, because lowering the amplitude and wavelength will result in higher mean forces, and therefore will increase EA.

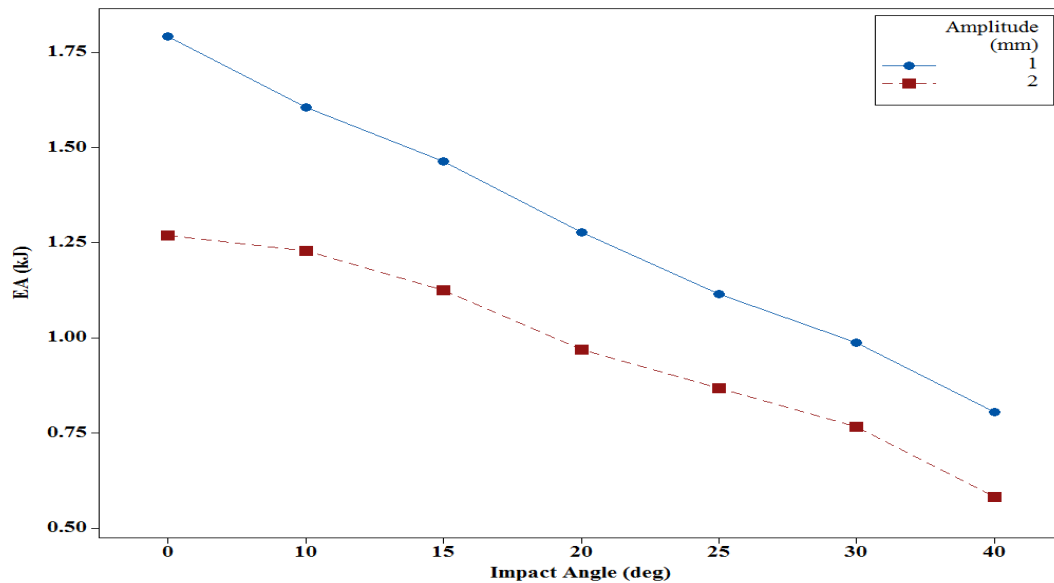


Figure 5-19: The Average Effect of Amplitude on EA Under Different Loading Angles

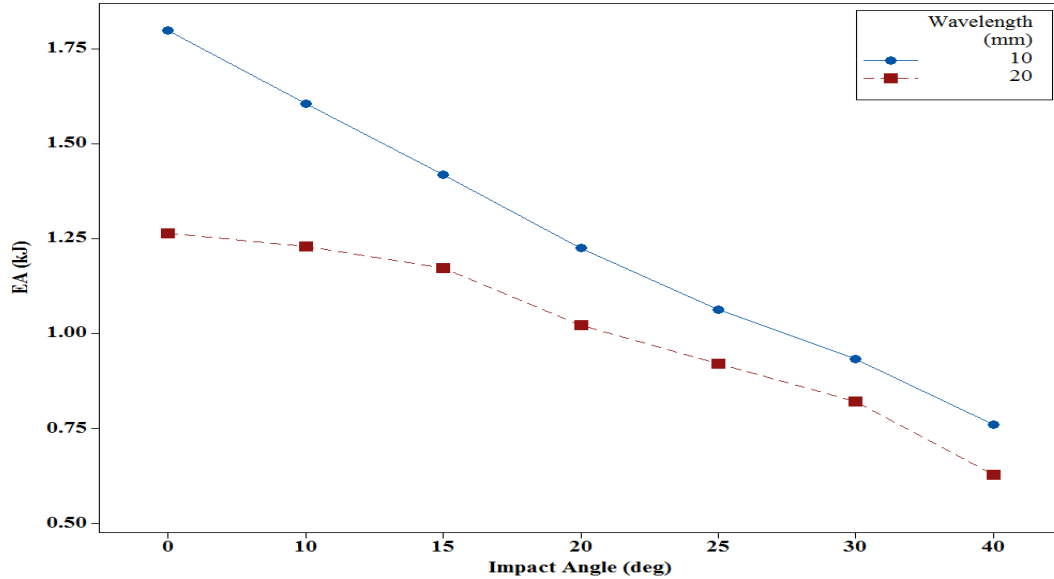


Figure 5-20: The Average Effect of Wavelength on EA Under Different Loading Angles

Moreover, increasing the thickness from 1 mm to 2 mm will result in higher EA under the tested range of impact angles as illustrated in Figure 5-21. This can be attributed to the structure's volume increase corresponding to the thickness increase, resulting in more material that can absorb the crushing energy. Finally, adopting a tapered angle of 80° will result in higher energy absorption under all loading angles when compared to a tapered angle of 85° as depicted in Figure 5-22. This is because of the larger lower diameter of the structure that corresponds to the tapered angle of 80° , which promotes axial crushing and hence increase the absorbed energy.

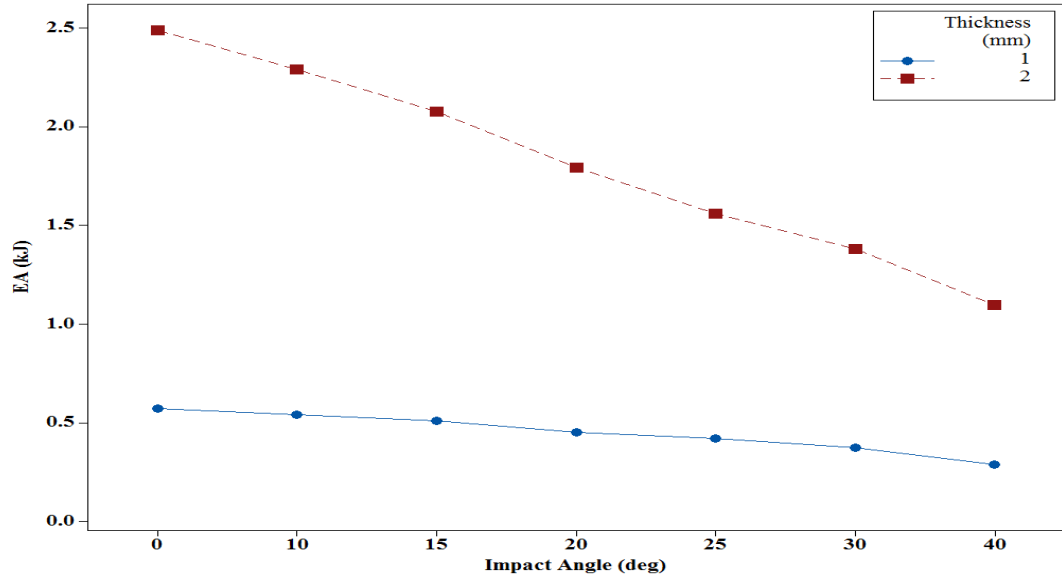


Figure 5-21: The Average Effect of Thickness on EA Under Different Loading Angles

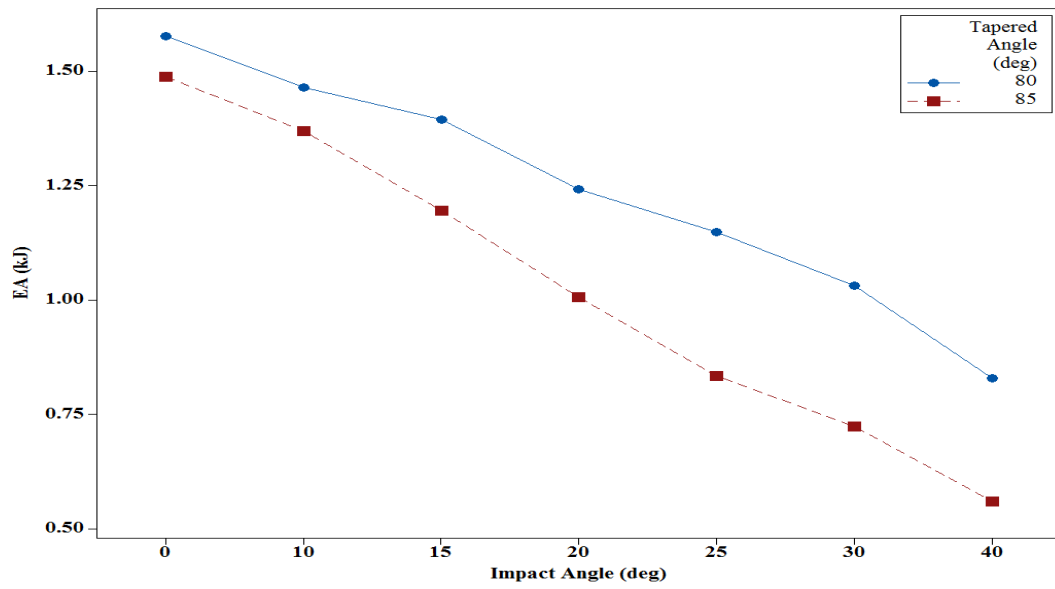


Figure 5-22: The Average Effect of Tapered Angle on EA Under Different Loading Angles

5.4.2.4 Influence on Specific Energy Absorption

The specific energy absorption relates the energy absorbed by the structure to its deformed mass. This indicator is vital for applications where lower mass is desired (i.e., automobile vehicles). As shown in Figure 5-23, an amplitude of 1 mm achieves higher SEA than an amplitude of 2 mm under the tested range of impact angles. This can be explained by two reasons: an amplitude of 1 mm results in higher MF and EA, and naturally higher SEA. The second reason is that a structure of 1 mm amplitude will have lower mass compared to its counterpart of 2 mm amplitude, and hence higher SEA. On the other hand, a wavelength of 10 mm will lead to a higher SEA up to an impact angle of 10° as shown in Figure 5-24. However, beyond the impact angle of 10°, no significant difference in SEA is observed between a wavelength of 10 and 20 mm.

Moreover, increasing the wall thickness to 2 mm results in a reduction in SEA (see Figure 5-25). This is mainly attributed to the structure's mass increase associated with the wall thickness increase. Finally, a CTT with an 85° tapered angle achieves higher SEA values than its counterpart CTT of 80° tapered angle, up to a 20° impact angle as shown in Figure 5-26. However, the opposite is true for impact angles larger than 20°.

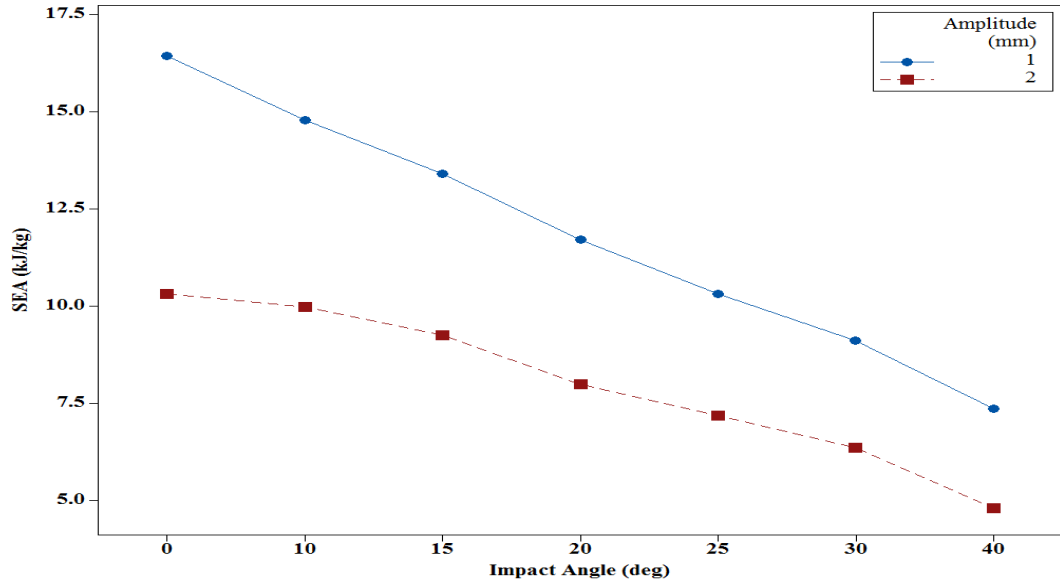


Figure 5-23: The Average Effect of Amplitude on SEA Under Different Loading Angles

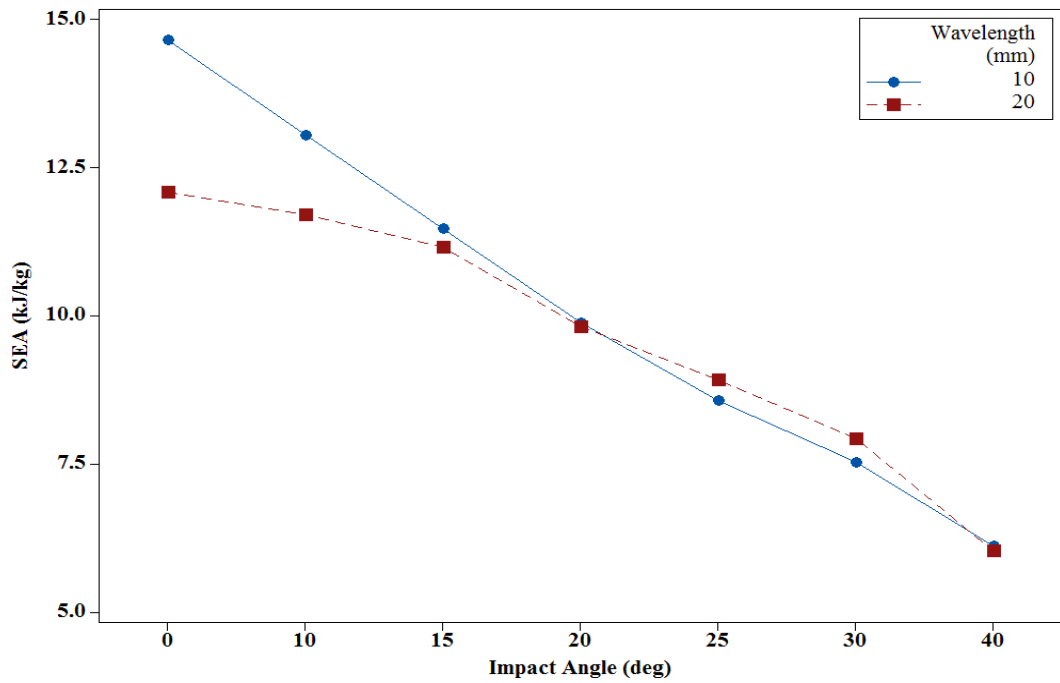


Figure 5-24: The Average Effect of Wavelength on SEA Under Different Loading Angles

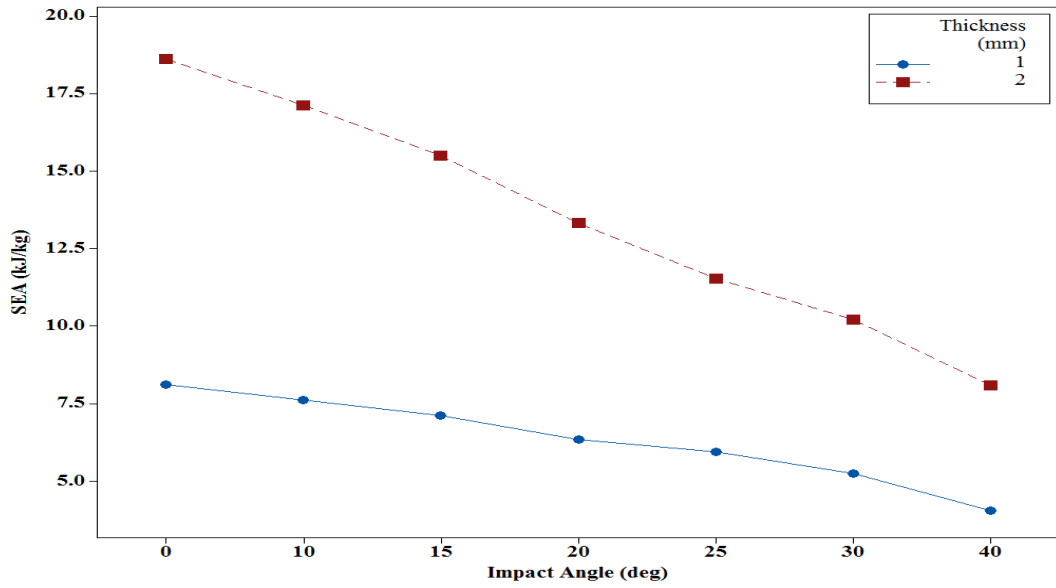


Figure 5-25: The Average Effect of Thickness on SEA Under Different Loading Angles

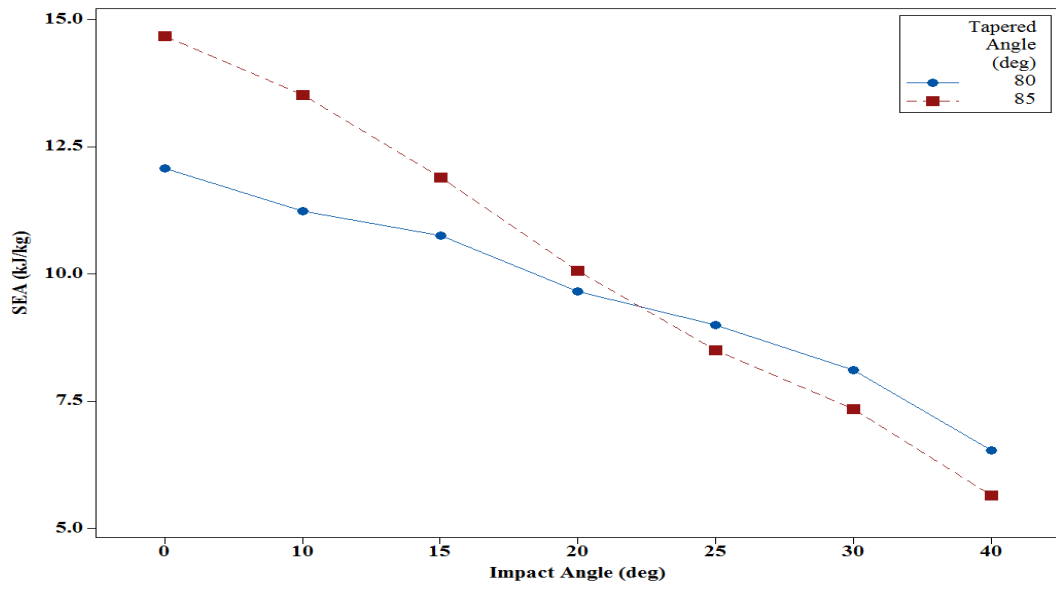


Figure 5-26: The Average Effect of Tapered Angle on SEA Under Different Loading Angles

5.5 Comparative Analysis

To visually compare the specific energy absorption (SEA) and mean force (MF) characteristics of all the tested CTTs to conventional tapered tubes, the values of SEA and MF under all loading angles are presented in Figure 5-27 to Figure 5-34. From Figure 5-27, it is clear that a conventional tapered tube of 80° tapered angle and 1 mm thickness have better SEA performance than CTTs of the same tapered angle and thickness under axial loading conditions (impact angle = 0°). However, a CTT of 1 mm amplitude and 20 mm wavelength have better SEA performance under oblique loading conditions. This can be explained by the lightweight this CTT has compared to its conventional counterpart. As for the MF values, the conventional tapered tube (tapered angle= 80° , Thickness= 1 mm) has higher MF values compared to the CTTs of the same geometric parameters as shown in Figure 5-28.

As for the conventional tapered tube of 2 mm thickness, the SEA and MF performances are better than CTTs of the same geometric parameters under all impact angles as shown in Figure 5-29 and Figure 5-30, respectively. It is worth mentioning that the best CTT profile of the same geometric parameters (Tapered Angle= 80° , Thickness= 2 mm) is of 1 mm amplitude and 10 mm wavelength.

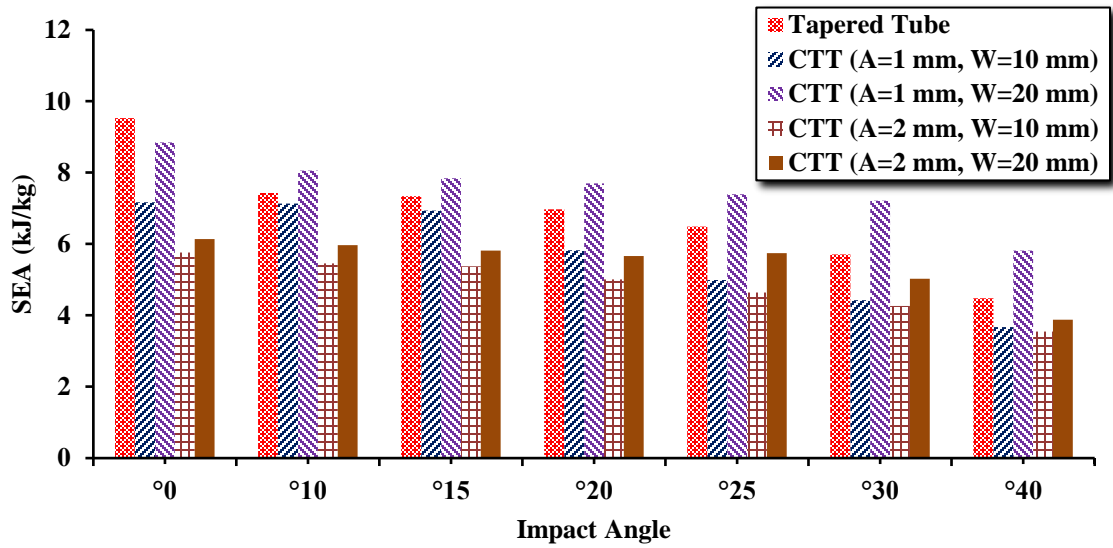


Figure 5-27: SEA Values for a Conventional Tapered Tube and CTT (Tapered Angle = 80°, Thickness = 1 mm)

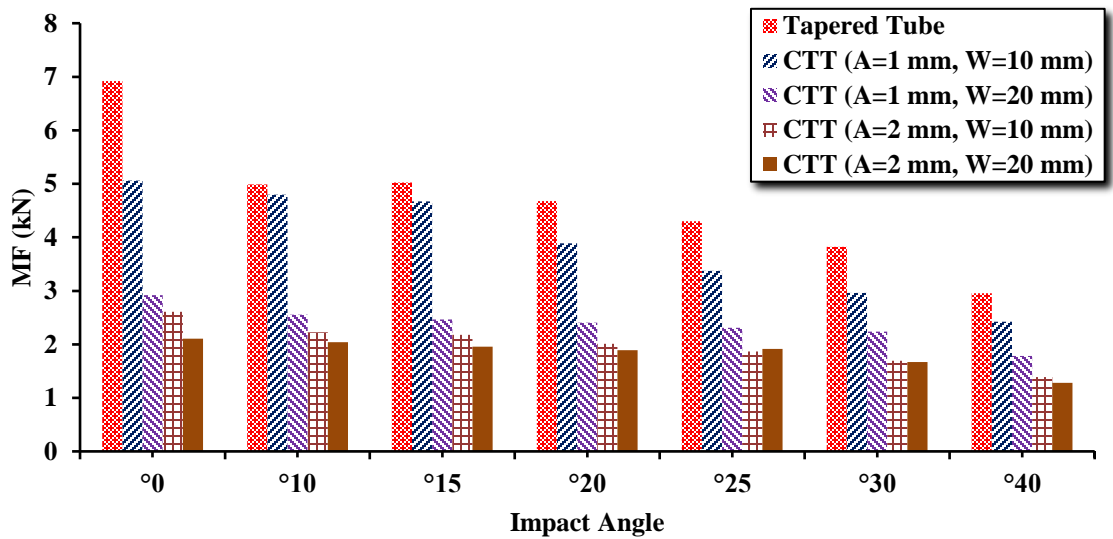


Figure 5-28: MF Values for a Conventional Tapered Tube and CTT (Tapered Angle = 80°, Thickness = 1 mm)

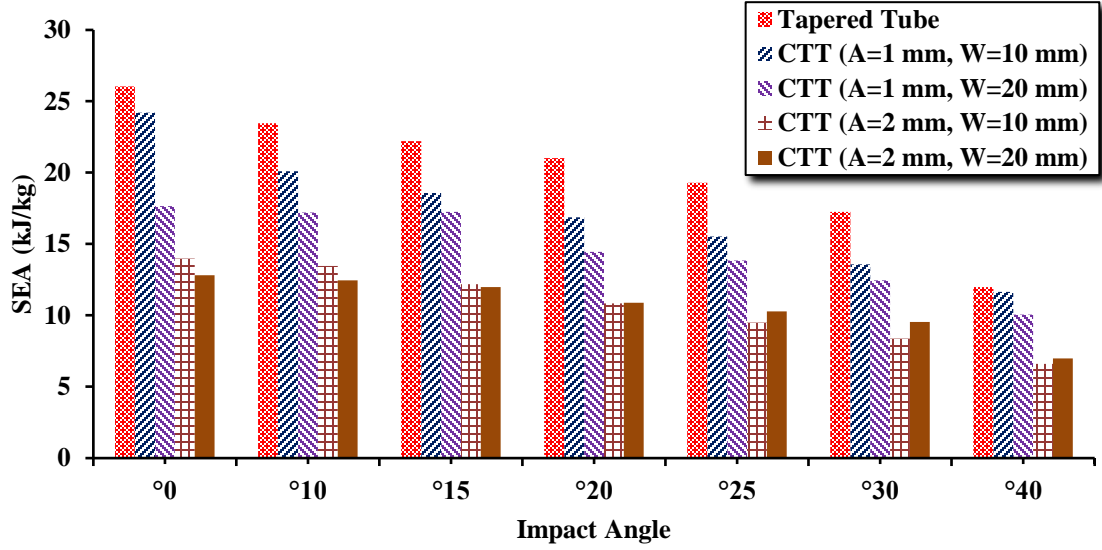


Figure 5-29: SEA Values for a Conventional Tapered Tube and CTT (Tapered Angle = 80°, Thickness = 2 mm)

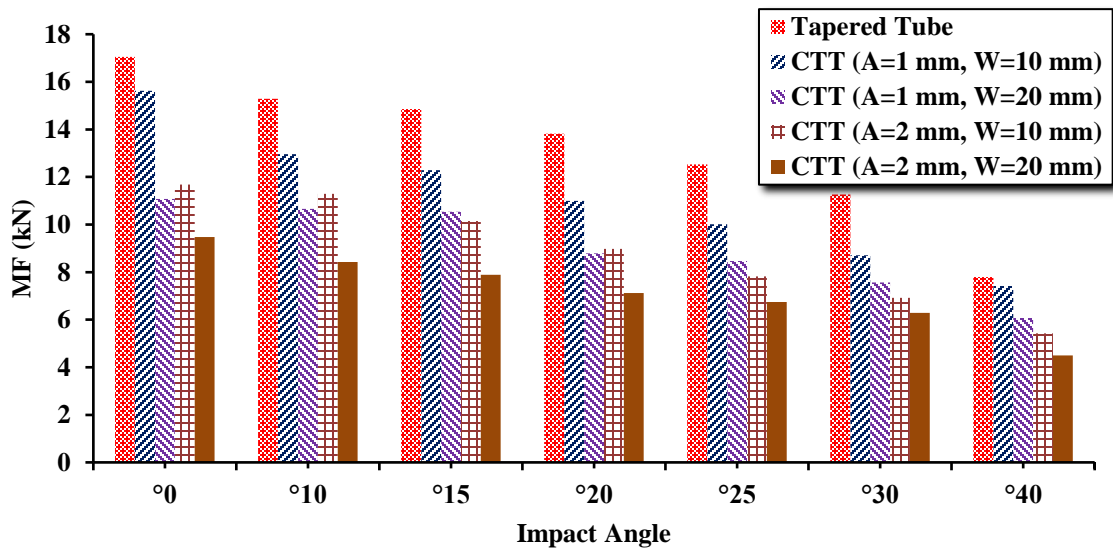


Figure 5-30: MF Values for a Conventional Tapered Tube and CTT (Tapered Angle = 80°, Thickness = 2 mm)

Figure 5-31 depicts the SEA values for a conventional tapered tube and CTTs of 85° tapered angle and 1 mm thickness. From here, it can be seen that a CTT of 1 mm amplitude and 10 mm wavelength has better SEA performance than its conventional counterpart under all impact angles. This can be mainly attributed to the light weight of this CTT relative to the conventional tapered tube. On the contrary, the conventional tapered tube has higher MF values than its counterparts of CTTs under all the tested impact angles (Figure 5-32).

Figure 5-33 depicts the SEA values of a conventional tapered tube and CTTs of 85° tapered angle and 2 mm thickness. From the figure, it is clear that a CTT of 1 mm amplitude and 10 mm wavelength has slightly higher SEA value than the conventional tapered tube under axial loading condition (impact angle = 0°). However, the conventional tapered tube has better SEA performance for the rest of the impact angles. Similarly, the conventional tapered tube has higher MF values than its counterparts of CTTs under all the tested impact angles as depicted in Figure 5-34.

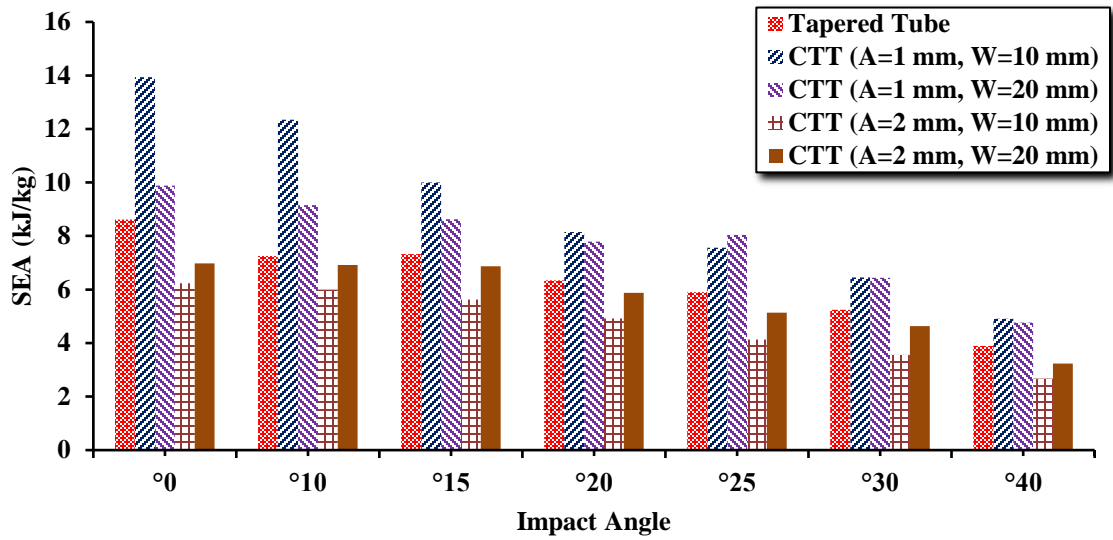


Figure 5-31: SEA Values for a Conventional Tapered Tube and CTT (Tapered Angle = 85°, Thickness = 1 mm)

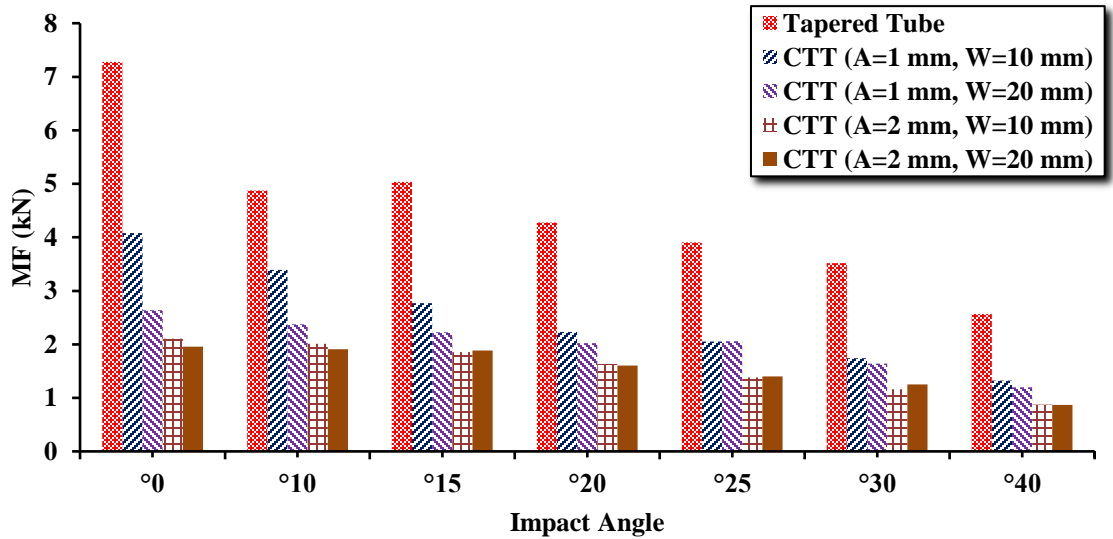


Figure 5-32: MF Values for a Conventional Tapered Tube and CTT (Tapered Angle = 85°, Thickness = 1 mm)

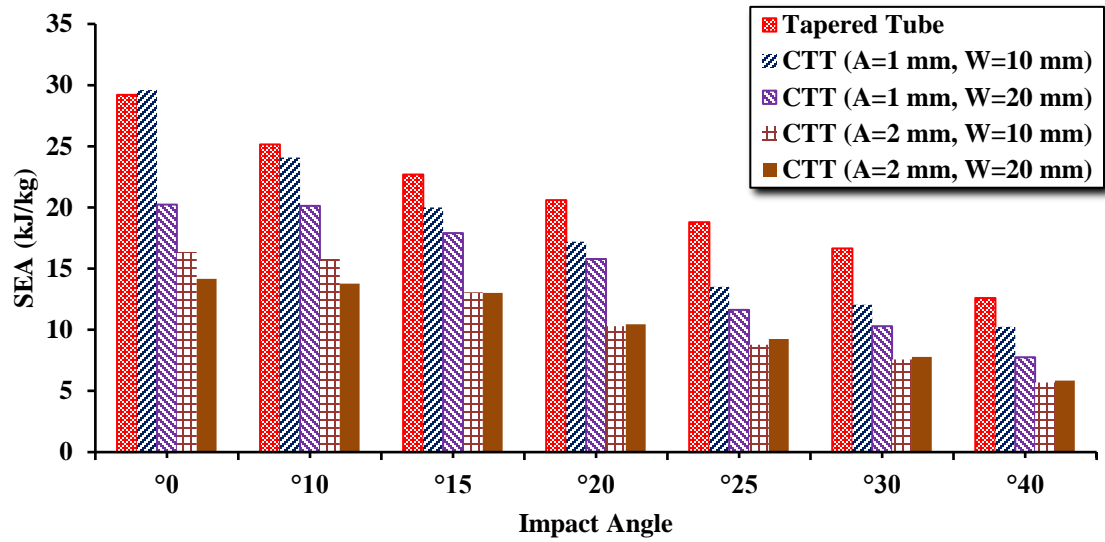


Figure 5-33: SEA Values for a Conventional Tapered Tube and CTT (Tapered Angle = 85°, Thickness = 2 mm)

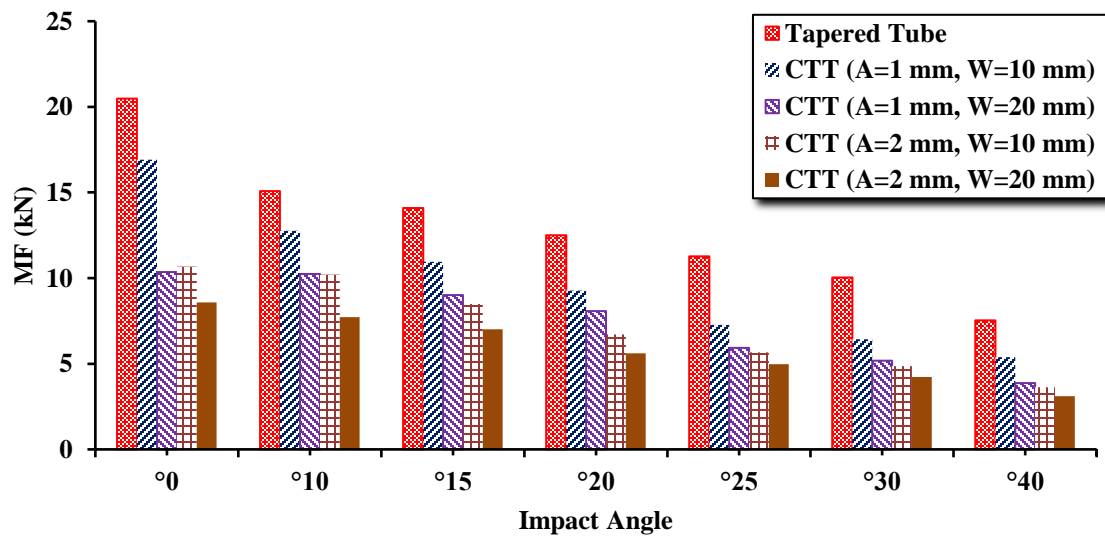


Figure 5-34: MF Values for a Conventional Tapered Tube and CTT (Tapered Angle = 85°, Thickness = 2 mm)

5.6 Summary

This chapter has investigated the performance of corrugated tapered tubes of different wavelengths and amplitudes under oblique loading conditions. In general, it was found that oblique loading angle inhibits and reduces the amount of energy absorbed by corrugated tapered tubes, as is the case for conventional tapered tubes. In addition, the geometric factors were found to influence the performance of corrugated tapered tubes under oblique loading similar to their effect on performance under axial impact. Furthermore, the transition to global Euler buckling was found to develop at higher impact angles for corrugated tapered tubes of 80° . Finally, it was found that corrugated tapered tubes can achieve better specific energy absorption performance than conventional tapered tubes.

Published work from this chapter:

S. E. Alkhatib, F. Tarlochan, Ahmad Hashem, Sadok Sassi, "Collapse behavior of thin-walled corrugated tapered tubes under oblique impact," *Thin-Walled Structures*, vol. 122, pp. 510-528, 2018. (Impact Factor: 2.829)

CHAPTER 6: CONCLUSIONS

Thin-walled energy absorbers have been widely used in safety applications, such as occupants carrying vehicles, due to their lightweight, energy absorption capabilities, and low manufacturing cost. The tremendous work on thin-walled structures in the open literature revealed that structures of corrugated surfaces reduce the crushing forces and offer a controllable manner of energy absorption, while tapered tubes are efficient energy absorbers under axial and oblique impact conditions. This thesis studied a tubular structure that combines the corrugated surface pattern and the tapered layout for its potential as an effective energy absorbing device under axial and oblique impacts. The study has been conducted numerically using a developed and experimentally validated finite element model using ABAQUS software. The influence of geometric parameters and loading angles on the proposed structure has been investigated, and the following conclusions are made:

- The force-displacement characteristics of CTTs are mainly influenced by the amplitude of the tube's corrugation, and a corrugation's amplitude of 2 mm will result in a smooth force-displacement curve and lower crushing forces along the crushing length regardless of the other geometrical parameters' values.
- There are three deformation modes exhibited for the tested CTT profiles, and they are mainly influenced by the corrugation's amplitude and wavelength.
- Adopting the corrugation reduces the initial peak force (IPF), specifically for longer amplitudes and wavelengths. Also, it reduces the energy absorption (EA) and specific energy absorption (SEA).

- Adopting the corrugation reduces the initial peak force (IPF) relative to a conventional tapered tube, and a maximum reduction of 93.38% is obtained. On the other hand, the energy absorption (EA) and specific energy absorption (SEA) of CTTs are lower compared to a conventional tapered tube in general.
- All the calculated performance indicators are significantly influenced by the corrugation's amplitude and wall thickness. The other geometrical parameters have minor influence or no effect the performance indicators.
- CTTs experience lower dynamic crushing forces (IPF and MF) and fewer fluctuations in forces than conventional tapered tubes under all the tested impact angles.
- Transition to global Euler buckling occurs at larger impact angles (25° - 40°) when the tapered angle is 80° , and at lower impact angles (15° - 20°) when the tapered angle is 85° .
- For CTTs of ($A=2$ mm, $W= 10$), global Euler buckling is not influenced by the tapered angle and develops at lower impact angles (15° - 20°).
- The initial peak force (IPF), mean force (MF), energy absorption (EA), and specific energy absorption (SEA) reduce with the increase of the impact angle.
- A reduction of approximately 54% in EA and SEA is observed when the impact angle increases from 0° (axial impact) to 40° .
- CTTs with shorter amplitudes and wavelengths have higher EA and SEA under all the tested impact angles.

- CTTs of higher thickness and smaller tapered angles offer higher EA compared to CTTs of lower thickness and larger tapered angles.
- Adopting corrugation can enhance the specific energy absorption under oblique loading conditions, as a CTT (Tapered Angle = 80° , Thickness = 1 mm) of 1 mm amplitude and 20 mm wavelength have higher SEA compared to a conventional tapered tube.

CHAPTER 7: RECOMMENDATIONS FOR FUTURE WORK

To support the conclusions drawn from this study, and to expand the knowledge area on the collapse behavior and energy absorption of corrugated tapered tubes, the following recommendations are proposed:

- Due to the time and cost constraints, the number of investigated geometric parameters and their levels was limited. Hence, studying more geometric parameters and geometric levels would give a broader picture of the performance of corrugated tapered tubes under axial and oblique impacts.
- Integrating the corrugated tapered tube in an energy absorbing system and testing it experimentally and numerically under axial and oblique loadings would reflect the realistic image of real-life crash situations. Moreover, it will provide more accurate insights on the performance of corrugated tapered tube as a part of an energy absorbing system rather than individually.
- Employing materials other than aluminum to the generated design profiles to investigate the effect of the material on the performance.
- Conducting a multi-objective optimization would leap a great benefit, as the optimization will provide the geometric parameters that will result in the optimum performance within the specified design and geometrical range

REFERENCES

- [1] D. Sperling, D. Gordon, and A. Schwarzenegger, *Two Billion Cars: Driving Toward Sustainability*: Oxford University Press, 2009.
- [2] "The Global Status Report on Road Safety 2015," World Health Organization (WHO).
- [3] T. Staff, T. Eken, T. B. Hansen, P. A. Steen, and S. Sjøvik, "A field evaluation of real-life motor vehicle accidents: Presence of unrestrained objects and their association with distribution and severity of patient injuries," *Accident Analysis & Prevention*, vol. 45, pp. 529-538, 2012/03/01/ 2012.
- [4] N. Jones, *Structural impact*: Cambridge university press, 2011.
- [5] J. Marsolek and H. G. Reimerdes, "Energy absorption of metallic cylindrical shells with induced non-axisymmetric folding patterns," *International Journal of Impact Engineering*, vol. 30, pp. 1209-1223, 2004/09/01/ 2004.
- [6] C. Bisagni, "Crashworthiness of helicopter subfloor structures," *International Journal of Impact Engineering*, vol. 27, pp. 1067-1082, 2002/11/01/ 2002.
- [7] A. G. Mamalis, M. Robinson, D. E. Manolakos, G. A. Demosthenous, M. B. Ioannidis, and J. Carruthers, "Crashworthy capability of composite material structures," *Composite Structures*, vol. 37, pp. 109-134, 1997/02/01/ 1997.
- [8] G. Lu and T. Yu, "11 - Composite materials and structures," in *Energy Absorption of Structures and Materials*, ed: Woodhead Publishing, 2003, pp. 317-350.
- [9] Z. Fan, G. Lu, and K. Liu, "Quasi-static axial compression of thin-walled tubes with different cross-sectional shapes," *Engineering Structures*, vol. 55, pp. 80-89, 10//

2013.

- [10] M. Liu, L. Zhang, P. Wang, and Y. Chang, "Buckling behaviors of section aluminum alloy columns under axial compression," *Engineering Structures*, vol. 95, pp. 127-137, 7/15/ 2015.
- [11] F. Tarlochan, F. Samer, A. M. S. Hamouda, S. Ramesh, and K. Khalid, "Design of thin wall structures for energy absorption applications: Enhancement of crashworthiness due to axial and oblique impact forces," *Thin-Walled Structures*, vol. 71, pp. 7-17, 10// 2013.
- [12] W. Liu, Z. Lin, N. Wang, and X. Deng, "Dynamic performances of thin-walled tubes with star-shaped cross section under axial impact," *Thin-Walled Structures*, vol. 100, pp. 25-37, 3// 2016.
- [13] O. Mohammadiha and H. Ghariblu, "Crush behavior optimization of multi-tubes filled by functionally graded foam," *Thin-Walled Structures*, vol. 98, Part B, pp. 627-639, 1// 2016.
- [14] G. Li, Z. Zhang, G. Sun, F. Xu, and X. Huang, "Crushing analysis and multiobjective optimization for functionally graded foam-filled tubes under multiple load cases," *International Journal of Mechanical Sciences*, vol. 89, pp. 439-452, 12// 2014.
- [15] G. Sun, G. Li, S. Hou, S. Zhou, W. Li, and Q. Li, "Crashworthiness design for functionally graded foam-filled thin-walled structures," *Materials Science and Engineering: A*, vol. 527, pp. 1911-1919, 3/25/ 2010.
- [16] F. Djamaluddin, S. Abdullah, A. K. Ariffin, and Z. M. Nopiah, "Optimization of

- foam-filled double circular tubes under axial and oblique impact loading conditions," *Thin-Walled Structures*, vol. 87, pp. 1-11, 2// 2015.
- [17] M. D. Goel, "Deformation, energy absorption and crushing behavior of single-, double- and multi-wall foam filled square and circular tubes," *Thin-Walled Structures*, vol. 90, pp. 1-11, 5// 2015.
- [18] Q. Gao, L. Wang, Y. Wang, and C. Wang, "Crushing analysis and multiobjective crashworthiness optimization of foam-filled ellipse tubes under oblique impact loading," *Thin-Walled Structures*, vol. 100, pp. 105-112, 3// 2016.
- [19] F. Li, G. Sun, X. Huang, J. Rong, and Q. Li, "Multiobjective robust optimization for crashworthiness design of foam filled thin-walled structures with random and interval uncertainties," *Engineering Structures*, vol. 88, pp. 111-124, 4/1/ 2015.
- [20] J. Song and F. Guo, "A comparative study on the windowed and multi-cell square tubes under axial and oblique loading," *Thin-Walled Structures*, vol. 66, pp. 9-14, 5// 2013.
- [21] H. Nikkhah, F. Guo, Y. Chew, J. Bai, J. Song, and P. Wang, "The effect of different shapes of holes on the crushing characteristics of aluminum square windowed tubes under dynamic axial loading," *Thin-Walled Structures*, vol. 119, pp. 412-420, 10// 2017.
- [22] C. W. Isaac and O. Oluwole, "Energy absorption improvement of circular tubes with externally press-fitted ring around tube surface subjected under axial and oblique impact loading," *Thin-Walled Structures*, vol. 109, pp. 352-366, 2016/12/01/ 2016.

- [23] S. Wu, G. Li, G. Sun, X. Wu, and Q. Li, "Crashworthiness analysis and optimization of sinusoidal corrugation tube," *Thin-Walled Structures*, vol. 105, pp. 121-134, 8// 2016.
- [24] Z. Liu, W. Hao, J. Xie, J. Lu, R. Huang, and Z. Wang, "Axial-impact buckling modes and energy absorption properties of thin-walled corrugated tubes with sinusoidal patterns," *Thin-Walled Structures*, vol. 94, pp. 410-423, 9// 2015.
- [25] C. Kılıçaslan, "Numerical crushing analysis of aluminum foam-filled corrugated single- and double-circular tubes subjected to axial impact loading," *Thin-Walled Structures*, vol. 96, pp. 82-94, 11// 2015.
- [26] S. Kokkula, M. Langseth, O. S. Hopperstad, and O. G. Lademo, "Offset impact behaviour of bumper beam—longitudinal systems: experimental investigations," *International Journal of Crashworthiness*, vol. 11, pp. 299-316, 2006/04/01 2006.
- [27] G. M. Nagel and D. P. Thambiratnam, "Dynamic simulation and energy absorption of tapered thin-walled tubes under oblique impact loading," *International Journal of Impact Engineering*, vol. 32, pp. 1595-1620, 10// 2006.
- [28] Y. Zhang, G. Sun, X. Xu, G. Li, and Q. Li, "Multiobjective crashworthiness optimization of hollow and conical tubes for multiple load cases," *Thin-Walled Structures*, vol. 82, pp. 331-342, 2014/09/01/ 2014.
- [29] A. Asanjarani, S. H. Dibajian, and A. Mahdian, "Multi-objective crashworthiness optimization of tapered thin-walled square tubes with indentations," *Thin-Walled Structures*, vol. 116, pp. 26-36, 2017/07/01/ 2017.
- [30] E. Acar, M. A. Guler, B. Gerçeker, M. E. Cerit, and B. Bayram, "Multi-objective

- crashworthiness optimization of tapered thin-walled tubes with axisymmetric indentations," *Thin-Walled Structures*, vol. 49, pp. 94-105, 1// 2011.
- [31] A. Taştan, E. Acar, M. A. Güler, and Ü. Kılınçkaya, "Optimum crashworthiness design of tapered thin-walled tubes with lateral circular cutouts," *Thin-Walled Structures*, vol. 107, pp. 543-553, 10// 2016.
- [32] X. Zhang, H. Zhang, and Z. Wen, "Axial crushing of tapered circular tubes with graded thickness," *International Journal of Mechanical Sciences*, vol. 92, pp. 12-23, 3// 2015.
- [33] C. Qi, S. Yang, and F. Dong, "Crushing analysis and multiobjective crashworthiness optimization of tapered square tubes under oblique impact loading," *Thin-Walled Structures*, vol. 59, pp. 103-119, 10// 2012.
- [34] R. A. Galganski, "Crashworthiness design of HSGGT vehicles," in *Proceedings of the 1993 IEEE/ASME Joint Railroad Conference*, 1993, pp. 121-130.
- [35] N. Jones and T. Wierzbicki, *Structural crashworthiness*: Butterworths, 1983.
- [36] A. Deb, M. S. Mahendrakumar, C. Chavan, J. Karve, D. Blankenburg, and S. Storen, "Design of an aluminium-based vehicle platform for front impact safety," *International Journal of Impact Engineering*, vol. 30, pp. 1055-1079, 2004/09/01/ 2004.
- [37] P. D. Bois, C. C. Chou, B. B. Fileta, T. B. Khalil, A. I. King, H. F. Mahmood, *et al.*, *Vehicle Crashworthiness and Occupant Protection*, 2000.
- [38] D. Karagiozova and N. Jones, "Dynamic elastic-plastic buckling of circular cylindrical shells under axial impact," *International Journal of Solids and*

Structures, vol. 37, pp. 2005-2034, 2000/04/01/ 2000.

- [39] Y. Chen, A. H. Clausen, O. S. Hopperstad, and M. Langseth, "Stress–strain behaviour of aluminium alloys at a wide range of strain rates," *International Journal of Solids and Structures*, vol. 46, pp. 3825-3835, 10/15/ 2009.
- [40] M. Itabashi and K. Kawata, "Carbon content effect on high-strain-rate tensile properties for carbon steels," *International Journal of Impact Engineering*, vol. 24, pp. 117-131, 2000/02/01/ 2000.
- [41] E. El-Magd and M. Abouridouane, "Characterization, modelling and simulation of deformation and fracture behaviour of the light-weight wrought alloys under high strain rate loading," *International Journal of Impact Engineering*, vol. 32, pp. 741-758, 2006/05/01/ 2006.
- [42] S. R. Reid and T. Y. Reddy, "Axial crushing of foam-filled tapered sheet metal tubes," *International Journal of Mechanical Sciences*, vol. 28, pp. 643-656, 1986/01/01/ 1986.
- [43] W. Abramowicz and N. Jones, "Dynamic axial crushing of circular tubes," *International Journal of Impact Engineering*, vol. 2, pp. 263-281, 1984/01/01/ 1984.
- [44] A. Shrot and M. Bäker, "Determination of Johnson–Cook parameters from machining simulations," *Computational Materials Science*, vol. 52, pp. 298-304, 2// 2012.
- [45] G. R. Johnson and W. H. Cook, "A constitutive model and data for metals subjected to large strains, high strain rates and high temperatures," in *7th International*

Symposium on Ballistics, The Hague, The Netherlands, 1983.

- [46] R. Liang and A. S. Khan, "A critical review of experimental results and constitutive models for BCC and FCC metals over a wide range of strain rates and temperatures," *International Journal of Plasticity*, vol. 15, pp. 963-980, 1999/01/01/ 1999.
- [47] C. R. Calladine and R. W. English, "Strain-rate and inertia effects in the collapse of two types of energy-absorbing structure," *International Journal of Mechanical Sciences*, vol. 26, pp. 689-701, 1984/01/01/ 1984.
- [48] D. Karagiozova, M. Alves, and N. Jones, "Inertia effects in axisymmetrically deformed cylindrical shells under axial impact," *International Journal of Impact Engineering*, vol. 24, pp. 1083-1115, 2000/11/01/ 2000.
- [49] B. Wang and G. Lu, "Mushrooming of circular tubes under dynamic axial loading," *Thin-Walled Structures*, vol. 40, pp. 167-182, 2002/02/01/ 2002.
- [50] G. Lu and T. Yu, "1 - Introduction," in *Energy Absorption of Structures and Materials*, ed: Woodhead Publishing, 2003, pp. 1-24.
- [51] S. R. Reid and J. J. Harrigan, "Transient effects in the quasi-static and dynamic internal inversion and nosing of metal tubes," *International Journal of Mechanical Sciences*, vol. 40, pp. 263-280, 1998/02/01/ 1998.
- [52] W. Abramowicz and N. Jones, "Dynamic progressive buckling of circular and square tubes," *International Journal of Impact Engineering*, vol. 4, pp. 243-270, 1986/01/01/ 1986.
- [53] T. Wierzbicki, S. U. Bhat, W. Abramowicz, and D. Brodtkin, "Alexander

- revisited—A two folding elements model of progressive crushing of tubes," *International Journal of Solids and Structures*, vol. 29, pp. 3269-3288, 1992/01/01/ 1992.
- [54] C. P. Gameiro and J. Cirne, "Dynamic axial crushing of short to long circular aluminium tubes with agglomerate cork filler," *International Journal of Mechanical Sciences*, vol. 49, pp. 1029-1037, 2007/09/01/ 2007.
- [55] G. Lu and T. Yu, "6 - Axial crushing of thin-walled members," in *Energy Absorption of Structures and Materials*, ed: Woodhead Publishing, 2003, pp. 144-173.
- [56] A. G. Hanssen, M. Langseth, and O. S. Hopperstad, "Static and dynamic crushing of circular aluminium extrusions with aluminium foam filler," *International Journal of Impact Engineering*, vol. 24, pp. 475-507, 5// 2000.
- [57] A. A. Singace, "Axial crushing analysis of tubes deforming in the multi-lobe mode," *International Journal of Mechanical Sciences*, vol. 41, pp. 865-890, 1999/07/01/ 1999.
- [58] S. R. Guillow, G. Lu, and R. H. Grzebieta, "Quasi-static axial compression of thin-walled circular aluminium tubes," *International Journal of Mechanical Sciences*, vol. 43, pp. 2103-2123, 2001/09/01/ 2001.
- [59] Z. Tang, S. Liu, and Z. Zhang, "Analysis of energy absorption characteristics of cylindrical multi-cell columns," *Thin-Walled Structures*, vol. 62, pp. 75-84, 1// 2013.
- [60] S. R. Reid, "Plastic deformation mechanisms in axially compressed metal tubes

- used as impact energy absorbers," *International Journal of Mechanical Sciences*, vol. 35, pp. 1035-1052, 1993/12/01/ 1993.
- [61] T. Wierzbicki and W. Abramowicz, "On the Crushing Mechanics of Thin-Walled Structures," *Journal of Applied Mechanics*, vol. 50, pp. 727-734, 1983.
- [62] W. Abramowicz and T. Wierzbicki, "Axial Crushing of Multicorner Sheet Metal Columns," *Journal of Applied Mechanics*, vol. 56, pp. 113-120, 1989.
- [63] A. G. Mamalis, D. E. Manolakos, A. K. Baldoukas, and G. L. Viegelaahn, "Energy dissipation and associated failure modes when axially loading polygonal thin-walled cylinders," *Thin-Walled Structures*, vol. 12, pp. 17-34, 1991/01/01/ 1991.
- [64] X. Zhang and H. Huh, "Crushing analysis of polygonal columns and angle elements," *International Journal of Impact Engineering*, vol. 37, pp. 441-451, 2010/04/01/ 2010.
- [65] Z. Tang, S. Liu, and Z. Zhang, "Energy absorption properties of non-convex multi-corner thin-walled columns," *Thin-Walled Structures*, vol. 51, pp. 112-120, 2012/02/01/ 2012.
- [66] M. Yamashita, M. Gotoh, and Y. Sawairi, "Axial crush of hollow cylindrical structures with various polygonal cross-sections," *Journal of Materials Processing Technology*, vol. 140, pp. 59-64, 2003/09/22/ 2003.
- [67] M. Abbasi, S. Reddy, A. Ghafari-Nazari, and M. Fard, "Multiobjective crashworthiness optimization of multi-cornered thin-walled sheet metal members," *Thin-Walled Structures*, vol. 89, pp. 31-41, 4// 2015.
- [68] X. Zhang, G. Cheng, and H. Zhang, "Theoretical prediction and numerical

- simulation of multi-cell square thin-walled structures," *Thin-Walled Structures*, vol. 44, pp. 1185-1191, 2006/11/01/ 2006.
- [69] X. Zhang and H. Zhang, "Energy absorption of multi-cell stub columns under axial compression," *Thin-Walled Structures*, vol. 68, pp. 156-163, 2013/07/01/ 2013.
- [70] X. Zhang and G. Cheng, "A comparative study of energy absorption characteristics of foam-filled and multi-cell square columns," *International Journal of Impact Engineering*, vol. 34, pp. 1739-1752, 2007/11/01/ 2007.
- [71] J. Fang, Y. Gao, G. Sun, N. Qiu, and Q. Li, "On design of multi-cell tubes under axial and oblique impact loads," *Thin-Walled Structures*, vol. 95, pp. 115-126, 2015/10/01/ 2015.
- [72] S. Tabacu, "Axial crushing of circular structures with rectangular multi-cell insert," *Thin-Walled Structures*, vol. 95, pp. 297-309, 2015/10/01/ 2015.
- [73] A. Alavi Nia and M. Parsapour, "Comparative analysis of energy absorption capacity of simple and multi-cell thin-walled tubes with triangular, square, hexagonal and octagonal sections," *Thin-Walled Structures*, vol. 74, pp. 155-165, 1// 2014.
- [74] N. Qiu, Y. Gao, J. Fang, Z. Feng, G. Sun, and Q. Li, "Crashworthiness analysis and design of multi-cell hexagonal columns under multiple loading cases," *Finite Elements in Analysis and Design*, vol. 104, pp. 89-101, 2015/10/15/ 2015.
- [75] A. Baroutaji, M. Sajjia, and A.-G. Olabi, "On the crashworthiness performance of thin-walled energy absorbers: Recent advances and future developments," *Thin-Walled Structures*, vol. 118, pp. 137-163, 2017/09/01/ 2017.

- [76] X. An, Y. Gao, J. Fang, G. Sun, and Q. Li, "Crashworthiness design for foam-filled thin-walled structures with functionally lateral graded thickness sheets," *Thin-Walled Structures*, vol. 91, pp. 63-71, 2015/06/01/ 2015.
- [77] X. Zhang, Z. Wen, and H. Zhang, "Axial crushing and optimal design of square tubes with graded thickness," *Thin-Walled Structures*, vol. 84, pp. 263-274, 11// 2014.
- [78] G. Li, F. Xu, G. Sun, and Q. Li, "A comparative study on thin-walled structures with functionally graded thickness (FGT) and tapered tubes withstanding oblique impact loading," *International Journal of Impact Engineering*, vol. 77, pp. 68-83, 2015/03/01/ 2015.
- [79] G. Li, Z. Zhang, G. Sun, X. Huang, and Q. Li, "Comparison of functionally-graded structures under multiple loading angles," *Thin-Walled Structures*, vol. 94, pp. 334-347, 2015/09/01/ 2015.
- [80] A. E. Markaki and T. W. Clyne, "The effect of cell wall microstructure on the deformation and fracture of aluminium-based foams," *Acta Materialia*, vol. 49, pp. 1677-1686, 2001/05/25/ 2001.
- [81] H. R. Zarei and M. Kröger, "Optimization of the foam-filled aluminum tubes for crush box application," *Thin-Walled Structures*, vol. 46, pp. 214-221, 2008/02/01/ 2008.
- [82] T. Børvik, O. S. Hopperstad, A. Reyes, M. Langseth, G. Solomos, and T. Dyngeland, "Empty and foam-filled circular aluminium tubes subjected to axial and oblique quasistatic loading," *International Journal of Crashworthiness*, vol. 8, pp.

481-494, 2003/01/01 2003.

- [83] M. Seitzberger, F. G. Rammerstorfer, R. Gradinger, H. P. Degischer, M. Blaimschein, and C. Walch, "Experimental studies on the quasi-static axial crushing of steel columns filled with aluminium foam," *International Journal of Solids and Structures*, vol. 37, pp. 4125-4147, 2000/07/01/ 2000.
- [84] A. K. Toksoy and M. Güden, "The strengthening effect of polystyrene foam filling in aluminum thin-walled cylindrical tubes," *Thin-Walled Structures*, vol. 43, pp. 333-350, 2005/02/01/ 2005.
- [85] S. Santosa and T. Wierzbicki, "Crash behavior of box columns filled with aluminum honeycomb or foam," *Computers & Structures*, vol. 68, pp. 343-367, 1998/08/01/ 1998.
- [86] S. R. Reid, T. Y. Reddy, and M. D. Gray, "Static and dynamic axial crushing of foam-filled sheet metal tubes," *International Journal of Mechanical Sciences*, vol. 28, pp. 295-322, 1986/01/01/ 1986.
- [87] W. Abramowicz and N. Jones, "Transition from initial global bending to progressive buckling of tubes loaded statically and dynamically," *International Journal of Impact Engineering*, vol. 19, pp. 415-437, 1997/05/01/ 1997.
- [88] M. A. Guler, M. E. Cerit, B. Bayram, B. Gerçeker, and E. Karakaya, "The effect of geometrical parameters on the energy absorption characteristics of thin-walled structures under axial impact loading," *International Journal of Crashworthiness*, vol. 15, pp. 377-390, 2010/10/14 2010.
- [89] A. Reyes, O. S. Hopperstad, and M. Langseth, "Aluminum foam-filled extrusions

- subjected to oblique loading: experimental and numerical study," *International Journal of Solids and Structures*, vol. 41, pp. 1645-1675, 2004/03/01/ 2004.
- [90] A. G. Mamalis and W. Johnson, "The quasi-static crumpling of thin-walled circular cylinders and frusta under axial compression," *International Journal of Mechanical Sciences*, vol. 25, pp. 713-732, 1983/01/01/ 1983.
- [91] A. Eyvazian, M. K. Habibi, A. M. Hamouda, and R. Hedayati, "Axial crushing behavior and energy absorption efficiency of corrugated tubes," *Materials & Design (1980-2015)*, vol. 54, pp. 1028-1038, 2// 2014.
- [92] A. Alavi Nia, K. Fallah Nejad, H. Badnava, and H. R. Farhoudi, "Effects of buckling initiators on mechanical behavior of thin-walled square tubes subjected to oblique loading," *Thin-Walled Structures*, vol. 59, pp. 87-96, 2012/10/01/ 2012.
- [93] K. Yang, S. Xu, J. Shen, S. Zhou, and Y. M. Xie, "Energy absorption of thin-walled tubes with pre-folded origami patterns: Numerical simulation and experimental verification," *Thin-Walled Structures*, vol. 103, pp. 33-44, 6// 2016.
- [94] N. Abedrabbo, R. Mayer, A. Thompson, C. Salisbury, M. Worswick, and I. van Riemsdijk, "Crash response of advanced high-strength steel tubes: Experiment and model," *International Journal of Impact Engineering*, vol. 36, pp. 1044-1057, 2009/08/01/ 2009.
- [95] Z. Ahmad and D. P. Thambiratnam, "Crushing response of foam-filled conical tubes under quasi-static axial loading," *Materials & Design*, vol. 30, pp. 2393-2403, 2009/08/01/ 2009.
- [96] X. Zhang and H. Zhang, "Crush resistance of square tubes with various thickness

- configurations," *International Journal of Mechanical Sciences*, vol. 107, pp. 58-68, 2016/03/01/ 2016.
- [97] O. C. Zienkiewicz and R. L. Taylor, *The Finite Element Method for Solid and Structural Mechanics*: Elsevier Science, 2013.
- [98] M. Smith, *ABAQUS/Standard User's Manual, Version 6.14*: Simulia, 2014.
- [99] E. Q. Sun, "Shear Locking and Hourglassing in MSC Nastran, ABAQUS, and ANSYS," in *MSC Software Corporation's 2006 Americas Virtual Product Development Conference: Evolution to Enterprise Simulation*, 2006, pp. 17-19.
- [100] W. J. Witteman, "Improved vehicle crashworthiness design by control of the energy absorption for different collision situations," Doctoral degree, Department of Mechanical Engineering, Technische Universiteit Eindhoven, Eindhoven, 1999.
- [101] NHTSA, "Consumer Information; New Car Assessment Program," ed. USA, 2008.
- [102] A. G. Olabi, E. Morris, M. S. J. Hashmi, and M. D. Gilchrist, "Optimised design of nested circular tube energy absorbers under lateral impact loading," *International Journal of Mechanical Sciences*, vol. 50, pp. 104-116, 1// 2008.
- [103] F. Pled, W. Yan, and W. Cui'e, "Crushing Modes of Aluminium Tubes under Axial Compression," presented at the 5th Australasian Congress on Applied Mechanics, Brisbane, Australia, 2007.

APPENDIX: PERFORMANCE INDICATORS SUMMARY

Table 1: Summary of the performance indicators (Amplitude=1 mm and Wavelength=10 mm)

Thickness (mm)	Top diameter (mm)	Tapered angle	Length (mm)	IPF (kN)	EA (kJ)	SEA (kJ/kg)
1	50	85°	150	11.36	1.22	20.89
2	40	80°	200	38.35	5.94	28.21
1	40	80°	200	11.63	2.26	19.41
2	50	80°	150	42.79	5.40	28.89
2	50	80°	200	41.67	7.60	26.84
2	50	85°	200	46.57	6.70	34.47
1	40	85°	150	9.65	1.31	24.61
2	40	85°	150	42.18	4.99	43.00
1	50	80°	200	12.80	2.51	18.14
2	50	85°	150	47.35	5.83	39.39
1	50	85°	200	11.74	2.34	23.91
2	40	80°	150	39.17	5.76	35.81
1	40	85°	200	9.58	2.00	24.86
2	40	85°	200	39.74	5.26	36.95
1	50	80°	150	11.36	1.97	21.19
1	40	80°	150	10.02	1.71	22.48

Table 2: Summary of the performance indicators (Amplitude=1 mm and Wavelength=20 mm)

Thickness (mm)	Top diameter (mm)	Tapered angle	Length (mm)	IPF (kN)	EA (kJ)	SEA (kJ/kg)
1	50	85°	200	11.15	1.04	14.33
2	50	85°	150	35.50	3.77	32.20
1	40	80°	200	11.40	2.37	20.50
2	40	85°	150	33.09	3.09	33.88
1	40	85°	200	9.85	1.07	15.57
2	40	80°	200	27.09	5.24	26.34
2	40	80°	150	29.46	4.23	31.30
2	40	85°	200	32.35	3.39	27.67
1	50	80°	200	12.00	1.98	15.96
1	40	85°	150	9.31	0.86	19.35
1	50	85°	150	10.34	1.06	16.28
2	50	80°	150	34.08	4.15	28.78
2	50	80°	200	32.46	5.91	24.45
1	40	80°	150	11.20	0.76	13.88
2	50	85°	200	36.42	4.34	26.28
1	50	80°	150	13.10	1.17	12.36

Table 3: Summary of the performance indicators (Amplitude=2 mm and Wavelength=10 mm)

Thickness (mm)	Top diameter (mm)	Tapered angle	Length (mm)	IPF (kN)	EA (kJ)	SEA (kJ/kg)
2	50	80°	150	24.44	3.78	16.90
2	40	85°	200	15.71	3.74	18.85
1	40	85°	200	4.40	0.74	7.50
1	50	80°	150	5.18	0.69	6.58
1	40	80°	200	4.40	0.93	6.68
1	50	85°	200	5.00	0.79	6.97
1	50	85°	150	4.88	0.60	7.22
2	50	80°	200	20.91	5.43	17.62
2	50	85°	150	24.96	3.06	18.93
2	40	80°	200	17.53	5.02	18.15
2	50	85°	200	19.63	4.36	18.80
1	40	85°	150	4.19	0.50	7.37
1	40	80°	150	3.87	0.63	6.84
2	40	85°	150	16.78	2.53	19.11
1	50	80°	200	4.86	1.03	4.93
2	40	80°	150	17.03	3.19	17.89

Table 4: Summary of the performance indicators for (Amplitude=2 mm and Wavelength=20 mm)

Thickness (mm)	Top diameter (mm)	Tapered angle	Length (mm)	IPF (kN)	EA (kJ)	SEA (kJ/kg)
1	50	80°	150	6.22	0.80	8.84
2	40	80°	150	18.48	3.23	21.15
1	40	85°	200	5.46	0.80	9.90
2	50	80°	150	20.65	3.45	19.19
2	50	80°	200	20.68	4.84	17.39
1	40	85°	150	5.46	0.70	12.06
2	50	85°	150	19.43	2.49	18.46
1	50	85°	150	6.09	0.58	8.64
2	40	80°	200	19.08	3.97	17.28
1	50	85°	200	5.95	0.79	8.55
1	50	80°	200	6.49	1.26	8.59
2	50	85°	200	19.79	2.92	17.11
1	40	80°	150	5.76	1.02	11.92
2	40	85°	200	17.32	3.07	19.13
1	40	80°	200	5.96	0.99	8.55
2	40	85°	150	16.91	2.47	21.72

Table 5: Summary of performance indicators (Amplitude=1 mm and Wavelength=10 mm)

Thickness (mm)	Tapered Angle	Impact Angle	IPF (kN)	MF (kN)	EA (kJ)	SEA (kJ)
1	80°	0°	8.18	5.06	0.84	7.17
2	80°	0°	31.51	15.62	3.45	24.20
2	85°	0°	29.50	16.91	3.47	29.59
1	85°	0°	8.22	4.08	0.82	13.94
1	80°	10°	3.33	4.80	0.84	7.14
2	80°	10°	9.66	12.95	2.87	20.10
2	85°	10°	10.54	12.76	2.82	24.07
1	85°	10°	3.44	3.39	0.72	12.35
1	80°	15°	2.96	4.67	0.81	6.94
2	80°	15°	7.08	12.29	2.65	18.58
2	85°	15°	8.62	10.95	2.35	20.00
1	85°	15°	2.92	2.77	0.59	10.00
1	80°	20°	2.37	3.89	0.68	5.82
2	80°	20°	5.24	10.99	2.41	16.86
2	85°	20°	6.24	9.27	2.02	17.19
1	85°	20°	2.54	2.23	0.48	8.15
1	80°	25°	1.80	3.37	0.59	4.99
2	80°	25°	3.92	10.02	2.21	15.52
2	85°	25°	4.46	7.28	1.59	13.52
1	85°	25°	2.04	2.05	0.44	7.56
1	80°	30°	1.37	2.96	0.52	4.42
2	80°	30°	3.07	8.70	1.94	13.58
2	85°	30°	3.66	6.43	1.41	12.05
1	85°	30°	1.64	1.74	0.38	6.45
1	80°	40°	0.94	2.42	0.43	3.67
2	80°	40°	2.09	7.42	1.66	11.64
2	85°	40°	2.22	5.39	1.20	10.24
1	85°	40°	1.04	1.32	0.29	4.91

Table 6: Summary of performance indicators (Amplitude=1 mm and Wavelength=20 mm)

Thickness (mm)	Tapered Angle	Impact Angle	IPF (kN)	MF (kN)	EA (kJ)	SEA (kJ)
1	85°	0°	5.13	1.96	0.41	6.97
2	85°	0°	17.43	8.58	1.66	14.17
1	80°	0°	5.74	2.11	0.44	6.14
2	80°	0°	18.01	9.47	1.84	12.82
1	85°	10°	2.67	1.91	0.41	6.91
2	85°	10°	7.27	7.73	1.62	13.77
1	80°	10°	2.69	2.04	0.43	5.97
2	80°	10°	7.16	8.42	1.79	12.46
1	85°	15°	2.32	1.89	0.40	6.87
2	85°	15°	5.87	7.02	1.53	13.02
1	80°	15°	2.30	1.96	0.42	5.81
2	80°	15°	5.52	7.88	1.72	11.98
1	85°	20°	2.04	1.60	0.34	5.87
2	85°	20°	5.05	5.62	1.23	10.46
1	80°	20°	2.26	1.89	0.41	5.66
2	80°	20°	4.29	7.12	1.56	10.88
1	85°	25°	2.27	1.40	0.30	5.13
2	85°	25°	4.06	4.98	1.09	9.25
1	80°	25°	2.10	1.92	0.41	5.74
2	80°	25°	3.50	6.74	1.47	10.29
1	85°	30°	1.81	1.25	0.27	4.63
2	85°	30°	3.23	4.23	0.91	7.79
1	80°	30°	2.00	1.67	0.36	5.03
2	80°	30°	2.93	6.29	1.37	9.54
1	85°	40°	1.39	0.87	0.19	3.24
2	85°	40°	2.46	3.11	0.69	5.85
1	80°	40°	1.74	1.28	0.28	3.88
2	80°	40°	4.65	4.50	1.00	6.99

Table 7: Summary of performance indicators (Amplitude=2 mm and Wavelength=10 mm)

Thickness (mm)	Tapered Angle	Impact Angle	IPF (kN)	MF (kN)	EA (kJ)	SEA (kJ)
2	85°	0°	18.70	10.66	2.31	16.36
1	80°	0°	4.22	2.61	0.50	5.76
1	85°	0°	4.66	2.11	0.44	6.24
2	80°	0°	20.46	11.68	2.56	13.97
2	85°	10°	8.69	10.20	2.23	15.80
1	80°	10°	2.94	2.22	0.47	5.45
1	85°	10°	2.70	2.01	0.42	5.99
2	80°	10°	9.37	11.29	2.47	13.46
2	85°	15°	8.08	8.48	1.85	13.08
1	80°	15°	2.76	2.18	0.46	5.38
1	85°	15°	2.49	1.86	0.40	5.62
2	80°	15°	8.22	10.15	2.24	12.19
2	85°	20°	7.60	6.71	1.46	10.30
1	80°	20°	2.57	2.01	0.43	5.01
1	85°	20°	2.36	1.63	0.35	4.92
2	80°	20°	8.16	8.98	1.99	10.84
2	85°	25°	7.24	5.68	1.24	8.78
1	80°	25°	2.48	1.86	0.40	4.64
1	85°	25°	2.28	1.38	0.29	4.13
2	80°	25°	7.76	7.82	1.74	9.49
2	85°	30°	7.05	4.87	1.07	7.57
1	80°	30°	2.36	1.69	0.37	4.26
1	85°	30°	2.21	1.16	0.25	3.56
2	80°	30°	7.17	6.91	1.54	8.38
2	85°	40°	5.62	3.62	0.80	5.69
1	80°	40°	1.88	1.39	0.30	3.54
1	85°	40°	1.99	0.87	0.19	2.67
2	80°	40°	5.55	5.43	1.21	6.60

Table 8: Summary of performance indicators (Amplitude=2 mm and Wavelength=20 mm)

Thickness (mm)	Tapered Angle	Impact Angle	IPF (kN)	MF (kN)	EA (kJ)	SEA (kJ)
1	85°	0°	5.13	1.96	0.41	6.97
2	85°	0°	17.43	8.58	1.66	14.17
1	80°	0°	5.74	2.11	0.44	6.14
2	80°	0°	18.01	9.47	1.84	12.82
1	85°	10°	2.67	1.91	0.41	6.91
2	85°	10°	7.27	7.73	1.62	13.77
1	80°	10°	2.69	2.04	0.43	5.97
2	80°	10°	7.16	8.42	1.79	12.46
1	85°	15°	2.32	1.89	0.40	6.87
2	85°	15°	5.87	7.02	1.53	13.02
1	80°	15°	2.30	1.96	0.42	5.81
2	80°	15°	5.52	7.88	1.72	11.98
1	85°	20°	2.04	1.60	0.34	5.87
2	85°	20°	5.05	5.62	1.23	10.46
1	80°	20°	2.26	1.89	0.41	5.66
2	80°	20°	4.29	7.12	1.56	10.88
1	85°	25°	2.27	1.40	0.30	5.13
2	85°	25°	4.06	4.98	1.09	9.25
1	80°	25°	2.10	1.92	0.41	5.74
2	80°	25°	3.50	6.74	1.47	10.29
1	85°	30°	1.81	1.25	0.27	4.63
2	85°	30°	3.23	4.23	0.91	7.79
1	80°	30°	2.00	1.67	0.36	5.03
2	80	30°	2.93	6.29	1.37	9.54
1	85	40°	1.39	0.87	0.19	3.24
2	85	40°	2.46	3.11	0.69	5.85
1	80	40°	1.74	1.28	0.28	3.88
2	80	40°	4.65	4.50	1.00	6.99